NOx Measurement and Characterization in a Gaseous Fueled High-Pressure Direct-Injection Engine

by

Troy Hurren

B. S., Mississippi State University, 2018

A THESIS SUBMITTED IN PARTIAL FULFILLMENT
OF THE REQUIREMENTS FOR THE DEGREE OF

Master of Applied Science

in

THE FACULTY OF GRADUATE AND POSTDOCTORAL
STUDIES
(Mechanical Engineering)

The University of British Columbia
(Vancouver)

December 2022

The following individuals certify that they have read, and recommend to the Faculty of Graduate and Postdoctoral Studies for acceptance, the thesis entitled:

NOx Measurement and Characterization in a Gaseous Fueled High-Pressure Direct-Injection Engine

submitted by **Troy Hurren** in partial fulfillment of the requirements for the degree of **Master of Applied Science** in **Mechanical Engineering**.

Examining Committee:

Patrick Kirchen, Professor, Mechanical Engineering, UBC
Supervisor

Kendal Bushe, Professor, Mechanical Engineering, UBC
Supervisory Committee Member

Jon Mikkelsen, Professor, Mechanical Engineering, UBC
Supervisory Committee Member

Abstract

Internal combustion engines (ICE) produce emissions that are harmful to the environment and human health. Strict governmental regulations put in place to reduce these harmful emissions have driven engine advancements such as high-pressure direct-injection (HPDI) of natural gas (NG) technology developed by Westport Fuel Systems (WFS). Because NG has a lower flame temperature than diesel, nitrogen oxides NO and NO_2 (NO_x), can be slightly reduced; nevertheless, they are still a problematic harmful emission in HPDI engines. The effects of exhaust gas recirculation (EGR), known to reduce in-cylinder temperatures and thus NO_x emissions in diesel compression ignition (CI) engines, is not as well understood in HPDI engines. The intent of this research is to develop a better understanding of the sensitivity of NO_x to the specific effects of EGR (in-cylinder temperature, oxygen concentration, and combustion duration) in HPDI engines. This was accomplished by identifying the limits of EGR as a NO_x reduction strategy in HPDI engines using a dry EGR system on a single cylinder research engine (SCRE).

A baseline engine operating condition was developed to maintain a constant engine load of 12 bar gross indicated mean effective pressure (GIMEP), constant combustion phasing, and constant engine speed throughout an EGR sweep. To better understand the role oxygen concentration plays in NO_x reduction, two equivalence ratios (ϕ) were tested and held constant throughout the EGR sweep: 0.6 and 0.7. The maximum EGR rate tested was ~50% for each ϕ. Combustion instability (measured by the coefficient of variability (COV) of peak cylinder pressure (PCP) and GIMEP) increased by 2 and 3% at maximum EGR for ϕ = 0.6 and 0.7, respectively.

NO_x emissions were reduced ~80% up to 25% EGR. However, NO_x sensitivity

to the effects of EGR diminish significantly at rates above 35%. The inverse is also true for particulate matter (PM) and methane in that these emissions significantly increase at EGR rates above 35%. Lastly, a kinetics analysis of the effects of EGR in a simplified HPDI model was developed to identify that NO_x is twice as sensitive to temperature changes as to changes in oxygen concentration changes.

Lay Summary

Heavy-duty diesel engines are emitters of pollutants NO and NO_2 (NO_x) which are known precursors to smog. Westport Fuel Systems (WFS) has developed high-pressure direct-injection (HPDI) of natural gas (NG) technology for heavy-duty engines which allows for diesel-like efficiencies and cleaner emissions. However, NO_x emissions are still relevant and little understanding exists on NO_x reduction strategies for HPDI engines including the effects of exhaust gas recirculation (EGR). The focus of this research is to develop a better understanding of the sensitivities of NO_x to the specific effects of EGR such as temperature, O_2 concentration and combustion duration. First, the limits of EGR on NOx reduction were identified by performing an EGR sweep experimentally. Secondly, the measured emissions were compared to kinetically simulated emissions to identify sensitivities. It was found that NO_x emissions are most sensitive at lower EGR rates and more sensitive to temperature changes.

Preface

This thesis includes experimental results from an incremental EGR sweep on a single cylinder research engine (SCRE) using Westport Fuel Systems' (WFS) high-pressure direct-injection (HPDI) technology. The SCRE and corresponding data acquisition system (DAQ) were already developed prior to my research beginning and training from Mike Karpinksi was received to learn operation of them. I designed and installed an exhasut gas recirculation (EGR) condensate trap to prohibit water from being trapped in the intake system and causing inconsistent intake composition resulting in poor repeatability of tests.

The gaseous emissions were analyzed using a Fourier transform infrared (FTIR) analyzer manufactured by Bruker. Training and assistance on the FTIR were given by Bruker (Dimitri Probst and Tobias Glaser specifically) to ensure proper setup and configuration prior to use.

All experimental tests, numerical models, data analysis, and conclusions presented in this work are my original work under the direct supervision of Dr. Patrick Kirchen. The experimental operating conditions were reviewed by Dr. Kirchen and WFS (Sandeep Munshi).

Table of Contents

List of Tables

List of Figures

List of Abbreviations

ASC	Ammonia slip catalyst
BDC	Bottom dead center
BMEP	Brake mean effective pressure
CAA	Clean Air Act
CAD	Crank angle degrees
CARB	California Air Resources Board
CERC	Clean Energy Research Center
CH_4	Methane
CI	Compression ignition
CLD	Chemiluminescence detector
CO	Carbon monoxide
CO_2	Carbon dioxide
COV	Coefficient of variance
DAQ	Data acquisition
DOC	Diesel oxidation catalyst
DPF	Diesel particulate filter
EGR	Exhaust gas recirculation
EMI	DElectromagnetic interference
EPA	Environmental Protection Agency

EVO	Exhaust valve open
FID	Flame ionization detector
FTIR	Fourier transform infrared
GHG	Greenhouse gas
GIMEP	Gross indicated mean effective pressure
GVWR	Gross vehicle weight rating
HDV	Heavy-duty vehicle
HPDI	High-pressure direct-injection
HRR	Heat release rate
ICE	Internal combustion engine
$IFSCH_4$	Indicated fuel specific CH_4
IFSCO	Indicated fuel specific CO
$IFSCO_2$	Indicated fuel specific CO_2
$IFSNO_x$	Indicated fuel specific NOx
IHR50	50% Integrated heat release
IMEP	Indicated mean effective pressure
IR	Infrared
$ISCH_4$	Indicated specific CH_4
ISCO	Indicated specific CO
$ISCO_2$	Indicated specific CO_2
ISNO	Indicated specific NO
$ISNO_2$	Indicated specific NO_2
ISNOx	Indicated specific NOx
IVC	Intake valve close
LDV	Light-duty vehicle
LPM	Litre per minute

N_2O	Nitrous oxide
NG	Natural gas
NI	National Instruments
NIMEP	Net indicated mean effective pressure
NO_x	Nitrogen oxides NO and NO_2
P & ID	Pipe and instrumentation diagram
PCP	Peak cylinder pressure
PM	Particulate matter
PSEP	Pulse separation
SCR	Selective catalytic reduction
SCRE	Single cylinder research engine
SI	Spark ignition
TDC	Top dead center
UHC	Unburnt hydrocarbons
V_d	Displacement volume
WFS	Westport Fuel Systems
ϕ	Equivalence ratio

Acknowledgments

Throughout my study and research for this thesis, many individuals have offered help, support, and guidance. I would like to thank some of them here.

First I would like to thank Dr. Pat Kirchen for the mentorship and guidance he offered along the whole time of this research. He had belief in me even as a young, naive researcher and has helped guide me to asking the correct, focused research questions and how to best answer those questions. His helpful suggestions on my presentations and writing helped me become a better presenter of my work. I could not have accomplished this without his mentorship and help.

I would also like to thank Sandeep Munshi of WFS for his helpful suggestions as my research objectives were discussed in collaboration with WFS.

Many individuals who had experience in the Clean Energy Research Center (CERC) helped me learn not only the specifics about the lab, but general tips about research as well. I would like to thank Mike Karpinsky for having helped train me on the operation of the single cylinder research engine (SCRE). I would like to thank Jeremy Rochussen for his helpful insights on being a graduate researcher and for our occasional car talk. Isaac Becker, Matt Knight, Mark Guan and Nicolas Jaeger all helped lift the spirits in the lab and gave their own insights to different perspectives on research.

I would like to thank my parents for always believing in me. My father was always providing positive support and encouragement and stories of when he completed his PhD many years ago.

Lastly, I would like to thank my wife, Kaylie Hurren, who I met during my research for this study. She helped me focus on the research when I most needed to and always showed support.

Chapter 1

Introduction

The internal combustion engine (ICE) is the primary power source for transportation and plays an important role in power generation [47]. It can be found in small light-duty passenger vehicles, large heavy-duty transport trucks and ships, and stationary power generators among others. Two of the most common ICE configurations are spark ignition (SI) and compression ignition (CI) engines. As the names suggest, SI engines traditionally compress a premixed fuel and air mixture in the cylinder before igniting the mixture with a spark, while CI engines compress air in the cylinder and inject high pressure fuel into the cylinder which spontaneously combusts upon atomizing and mixing with the air. CI engines are typically fuelled by diesel and found in heavy duty applications due to their higher efficiency and torque. This is made possible by the higher compression ratios as compared to the preignition, or knock, limited compression ratios of SI engines typically fuelled by gasoline [20]. Unfortunately, CI diesel engines have a reputation of polluting the environment with nitrogen oxides (NO_x) and particulate matter (PM), or soot [48].

While the light-duty vehicle (LDV) market is adapting battery electric drivetrains to overcome tailpipe emissions [58], the greater size and weight along with the long haul demands of heavy duty transportation vehicles (HDV) (trucks, ships, locomotives) significantly increases the obstacles of batteries being able to replace CI engines [38]. However, there are measures that can be taken now to help reduce emissions that have health and environmental effects from CI engines. One such method is to use alternative fuels such as natural gas (NG) or other less carbon

intensive gaseous fuels. The focus of this work is on heavy-duty high-pressure direct-injection (HPDI) engines using low carbon intensive NG.

The motivation of this research comes from the understanding that CI engines will continue to play a role in transportation and power generation and thus focuses on reducing the environmentally harmful emissions of CI engines. The following sections describe first what health and environmental impacts CI engines have and specifics about the formation of the emissions, then what regulations and subsequent methods have been put in place to manage these emissions. Finally, details of HPDI NG engines and how they can help reduce carbon based emissions are discussed along with a literature review of NO_x reduction strategies in such engines.

1.1 Health and Environmental Effects of CI Engines

Emissions from CI engines that have an environmental and health impact can be divided into two categories: greenhouse gas (GHG) emissions and pollutants [58]. A GHG is defined as any gas that traps heat in the atmosphere such as carbon dioxide (CO_2), methane (CH_4), and nitrous oxide (N_2O) [21]. Pollutants represent any emissions that are harmful to human health such as nitrogen oxides (NO_x), carbon monoxide (CO), and particulate matter (PM), or soot.

First, the GHG emissions of CI engines, especially those prominent in NG fueled engines include CO_2 and CH_4. Because NG is a fossil fuel composed primarily of methane (about 95% by volume in British Columbia [23]) and other various gas species [45] as outlined in Table 1.1 (specifically for the British Gas Plc. [37]), the GHG emissions that are most prominent in NG fuelled engines are CO_2 and CH_4. While the use of NG in an ICE has been shown to reduce CO_2 emissions by 20-30% due to the lower carbon-hydrogen ratio [40], methane has a global warming potential of approximately 72 and 28 times that of CO_2 on a 20 and 100 year period respectively [5, 39].

Table 1.1: NG Composition [37]

Species	Concentration
Methane	92%
Ethane	3%
Propane	0.7%
Butane	0.02%
Pentane	0.1%
Carbon Dioxide	0.6%
Nitrogen	3%%

Nitrogen oxides (NO_x), made up of NO and NO_2, are pollutants because they are known to precede acid rain and photochemical smog [25]. They have also been linked to eye and respiratory irritation to humans [62]. Another pollutant is carbon monoxide (CO); a toxic, odorless, invisible gas with a short term exposure limit of 100 parts per million (ppm) for 15 minutes making it extremely toxic [72].

Lastly, Particulate matter (PM) is another emission common to CI engines sometimes referred to as soot. A typical composition of PM from a diesel engine exhaust may look similar to what is referenced in Table 1.2 [24] consisting of solid and semivolatile particles. PM can be measured by total mass or particle size [52]

Table 1.2: Particulate Matter Composition [24]

Species	Concentration
Carbon	31%
Unknown	8%
Sulphate & water	14%
Unburned fuel	7%
Unburned oil	40%

and sizes for PM are divided into four categories as seen in Table 1.3 [70]. PM has been identified as an irritant and carcinogen and a correlation exists between mortality and concentrations of $PM_{2.5}$ or smaller [24].

Table 1.3: Pariculate Matter Size Characterization [70]

Particulate	Particle Size ($\leq\mu$ m)	Influences on Human Health
PM_{100}	100	Persist in the air, no evidence of adverse effects on human health
PM_{10}	10	Enter the respiratory system and cause respiratory diseases
$PM_{2.5}$ PM_1	2.5 1	Get into the alveoli through the respiratory tract then enter into the blood circulation, causing various diseases.

1.2 Formation of Emissions and Pollutants in CI Engines

The following sections will go into more detail how the different emissions from CI engines are formed including NO_x, PM, CO, and unburnt hydrocarbons (UHC).

1.2.1 NOx

NO_x formation is dependent on temperature, O_2 concentration, and combustion duration (sometimes referred to as residence time) [24]. NO_x can be formed at high temperatures from the oxidation of nitrogen fixated in the air or bound in the fuel [25]. NO_x formed through fuel bound nitrogen refers to atomic nitrogen (N), and is usually found in solid fuels such as coal [71]. Although nitrogen does make up approximately 3% of NG as referenced in table 1.1, this is molecular nitrogen (N_2) and it will act similar to the air-bound nitrogen in the formation of NO_x. For this purpose, this study will not focus on the formation of fuel bound NO_x.

There are three different routes for the formation of NO_x from nitrogen fixated in air: the thermal route (also known as Zeldovich route), the prompt route (also known as Fenimore route) and the N_2O route [71]. First, Zeldovich NO, named after Y. B. Zeldovich who postulated the mechanism, requires a very high activation energy for the rate limiting step of the thermal NO formation [71]. The term thermal NO is also used due to the high temperatures over 1700K necessary for

the rate coefficient of the rate limiting step to become significant. For this purpose, the temperature of 1700K will be referred to as the Zeldovich threshold temperature throughout this study to represent the global temperature where significant thermal NO_x is formed. This route also requires time much longer than typical combustion duration times seen in internal combustion engines to reach equilibrium. When characterizing thermal NO production from a flame, it is measured behind the flame front to provide the time necessary to form NO.

The Fenimore route, named after C. P. Fenimore, is also called the prompt route because, unlike the thermal route, NO is formed promptly at the flame front instead of downstream [71]. This route requires the radical CH which exists in appreciable quantities at the flame front and is more common in fuel rich zones. It is possible to have prompt NO formation at temperatures around 1000K. Lastly, lean combustion can extinguish prompt NO and low temperatures can extinguish thermal NO, but NO can still be generated by the N_2O route. This route requires a third body reaction and has a low activation energy so lower temperatures do not penalize NO in this route as significantly as thermal NO.

1.2.2 Particulate Matter

Particulate matter (PM) forms in the fuel rich zones of the fuel-air mixture of combustion where there is not enough oxygen available for full oxidation of the fuel [42]. The process involved in the formation of PM includes several steps as outlined in Fig. 1.1. First, in the oxygen deficient environment, the fuel undergoes pyrolysis to form the precursors of PM before nuclei are formed through nucleation [32] which provide a surface for growth. Finally, while accumulating growth, the particles coalesce to form complex hydrocarbon laden aggregate structures that chain together to form agglomerates.

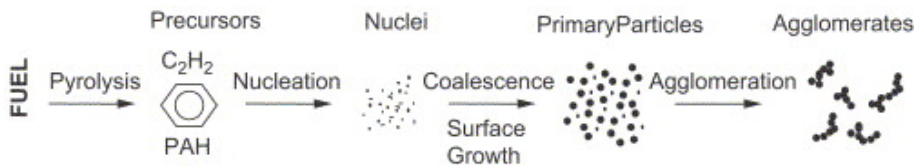

Figure 1.1: Schematic of particulate matter formation from pyrolysis of fuel to agglomerate of particles. Used with permission. Copyright © 2006 Elsevier Ltd. All rights reserved. [64]

It is also important to note that the entire process of particulate formation takes time, and oxidation and dehyrdogenation is occurring throughout the entire process as shown in Fig. 1.2 [2]. This leads to a loss in mass throughout the process. However, adsorption from chemical or physical forces [6] can also occur even after combustion and can affect the total mass measured from the tailpipe emissions. The formation of PM is a nonequilibrium process and in turn results in nonuniform particle sizes which can be categorized to show the distribution [32].

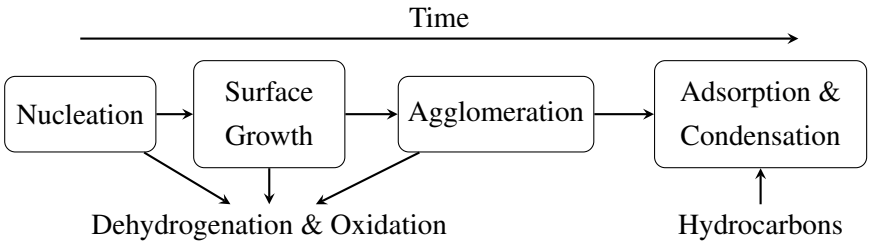

Figure 1.2: Process of formation of particulate matter including the dehydrogenation and oxidation before adsorption is affected by hydrocarbons[2]

1.2.3 Carbon Monoxide

CO emissions are predominantly controlled by the air-fuel ratio in an ICE [34]. When under a fuel rich operating condition, there is insufficient air in the system to fully oxidize all of the hydrocarbon fuel to CO_2, thus leading to CO. Fuel lean conditions lead to less CO formation in an ICE [30], and because CI engines tend to operate in lean conditions, CO emissions are not as much of a concern as they are for SI engines [34].

1.2.4 Unburnt Hydrocarbons

Hydrocarbons in the emissions of an ICE originate from hydrocarbon fuels that escape the combustion chamber partially burned, recombined, or completely unburnt [42]. When using NG as the primary fuel, the most common case for UHCs is through what the literature refers to as methane slip [69]. This is due to bulk quenching in the coldest regions of the combustion chamber which most frequently occurs under very fuel lean and low load operating conditions [61].

1.3 Emissions Regulations

The control of the quantity and composition of emissions for ICEs has historically been regulated by governmental bodies to ensure the local ambient air quality is maintained or even improved [42]. Traditionally, these regulations monitored pollutants known to be harmful to humans, but recent regulations also focus on GHG emissions[65]. The regulations are regionally regulated and differ by vehicle type (LDV and HDV). For instance, in The United States, the regulating department is the Environmental Protection Agency (EPA), while in Europe, the European Union develops the standards (currently the Euro VI standards). Because this work is focusing primarily on heavy-duty engines and because Canada uses emission standards that are harmonized with the US standards [15], this chapter will focus on the current EPA emissions standards for HDVs defined as any vehicle with a gross vehicle weight rating (GVWR) of more than 8500 lb [28].

The EPA standards have changed over the years to continue to improve ambient air conditions. The first standards were established in 1974 and have gone through several renditions since. Table 1.4 shows the current EPA emission standards established in 2007 for pollutant emissions [14]. The NO_x standards before this were 4.0 $\frac{g}{kW*hr}$ so the 2007 standards were phased in between years 2007 to 2010 [14]. Table 1.5 shows the GHG emission standards for HDVs set by the EPA

Table 1.4: EPA 2007 Pollutant Emission Standards

Units	CO	HC	NOx	PM
$\frac{g}{hp*hr}$	15.5	0.14	0.2	0.01
$\frac{g}{kW*hr}$	20.8	0.19	0.27	0.013

for the model year 2021. These standards were phased in with increased stringency each year and will continue to do so until 2027 [13].

Table 1.5: EPA 2021 GHG Emission Standards

Units	CO_2	CH_4
$\frac{g}{hp*hr}$	513	0.10
$\frac{g}{kW*hr}$	689	0.13

The state of California enacted its own standards before the federal Clean Air Act (CAA) was put in place so they still have the liberty to set their own standards under the California Air Resources Board (CARB) and have plans to set even more stringent standards for upcoming years [42]. In 2020 CARB approved the Heavy-Duty Low NOx Omnibus Regulation that requires a further 90% decrease in NO_x emissions and supercedes the optional low NO_x standards set in 2014. This emphasizes even more the need for understanding NO_x emissions for more developments in low NO_x ICEs in the heavy-duty sector to meet and continue to meet these ever changing stringent standards.

1.4 Methods to Reduce ICE Emissions

Engine emissions are controlled from two primary sytems: the in-cylinder combustion system and post combustion emission aftertreatment system [16]. This work focuses on the in-cylinder combustion system, but a brief summary of the aftertreatment methods of emission control will precede the in-cylinder combustion methods in this section.

1.4.1 Emission Aftertreatment System

The purpose of aftertreatment systems is not to erase all emissions from ICEs, but rather to convert the toxic pollutants, such as NO_x, CO and PM, to less harmful emissions such as CO_2, water, and molecular nitrogen [42]. The system is typically made up of a combination of filters and catalysts and a combination of four of these can be found for heavy-duty engines specifically. These include a diesel particulate filter (DPF) to filter the PM, a diesel oxidation catalyst (DOC) to oxidize the CO, a selective catalytic reduction catalyst (SCR) that uses onboard urea injection to

reduce NO_x, and finally an ammonia slip catalyst (ASC) to convert the ammonia from the SCR to inert nitrogen and water [42].

The aftertreatment system will not be 100% efficient. For example, the DPF filters and oxidizes the PM reducing the tailpipe PM emissions by over 90% [10]. The SCR is capable of reductions in NO_x emissions at efficiencies from 70-90% within a cost-effective manner [68]. The SCR also functions on the principal of three chemical reduction reactions termed ”standard”, ”slow”, and ”fast” SCR reactions and the ’fast” reaction is the preferred reaction due to its efficient reduction, but requires a 1:1 ratio of NO to NO_2 [42]. This means there still needs to be careful attention to how the emissions are controlled in-cylinder to ensure the aftertreatment system will be capable of converting the harmful emissions to acceptable rates.

1.4.2 In-Cylinder Combustion System

Because all of the emissions discussed thus far, including GHG and pollutant emissions, are produced through combustion of fuel in a cylinder of an engine, it is imperative to understand what in-cylinder combustion mechanisms can be adjusted or improved to mitigate these emissions as much as possible. The following subsections will cover how fuel interacting with air in the combustion chamber and how the composition of the mixture in-cylinder affect emissions.

1.4.3 Interaction of Fuel with Air In-cylinder

Emissions are affected by the design of the combustion chamber and how the fuel interacts with the air within the chamber [3]. Better mixing, whether brought on by swirl or turbulence induced by chamber design or injection techniques, stimulates better entrainment of the fuel with air which leads to more complete combustion. This results in fewer unoxidized or partially oxidized emissions such as CO and PM, but can lead to higher in-cylinder temperatures which lead to higher NO_x emissions. These must be managed by altering the composition and or initial parameters of the in-cylinder mixture.

1.4.4 In-cylinder Conditions and Mixture Composition

Adjusting the initial conditions of the in-cylinder contents will affect the emissions. For example, higher combustion temperatures are accompanied with higher intake air pressure temperatures (induced by increased manifold air pressure) which in turn will increase NO_x production [3]. Also, adjusting the equivalence ratio (ϕ) (ratio of the fuel to air normalized by the stoichiometric fuel to air ratio) affects both the oxygen concentration and combustion temperature thus having an effect on all emissions as seen in Fig. 1.3. It can be seen that CO and UHCs are lower in the fuel lean conditions while NO_x is highest slightly lean of stoichiometry. This is due to the higher combustion temperatures at stoichiometry and a higher oxygen concentration at more lean conditions.

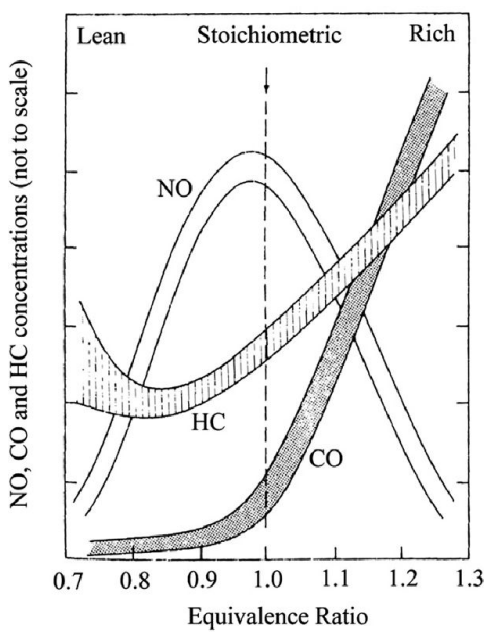

Figure 1.3: Emissions vs equivalence ratio trends for typical SI engines [34]

Lastly, the composition of the mixture can be adjusted to control emissions. A common method used for reducing in-cylinder temperatures in CI engines is through the use of exhaust gas recirculation (EGR). An example of how this works is shown in Fig. 1.4 where a diagram of a high pressure (both the intake and

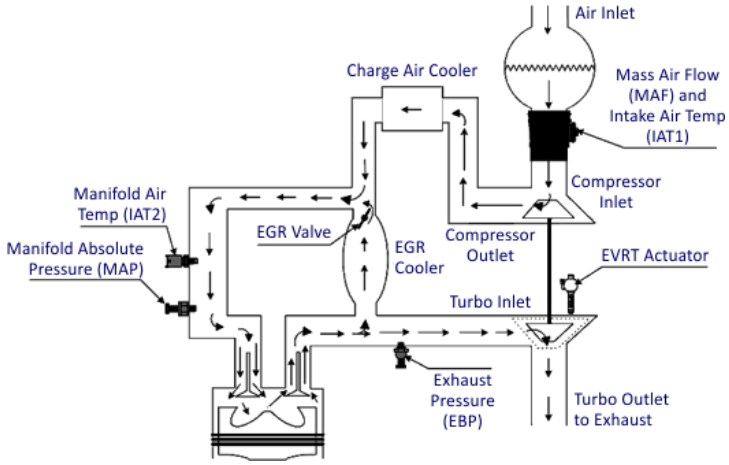

Figure 1.4: Diagram of a high pressure loopEGRsystem found in a 2003 Ford superduty. Used with permission. Copyright © ECOpoint Inc. Revision 2016.06 [12]

exhaust gases are mixed post turbocharger) EGR system is shown. As the exhaust pressures build behind the turbocharger, the EGR valve can be controlled to allow a portion of the exhaust gases to mix with the fresh intake charge. The primary purpose of EGR is to 1) reduce the oxygen concentration of the intake charge and 2) increase the specific heat of the intake charge and thus reduce the combustion temperatures [3]. Both of these effects have an impact on NO_x production.

Another method to reduce the mixture composition of the reactants is to change what fuel is used. This can be done either by using a mixture of fuels or changing the fuel altogether. Studies have shown that by using alternative fuels, engine metrics, such as peak cylinder pressure (PCP) and ignition timing, can be influenced [8, 36]. This is due to different combustion temperatures and flame speeds of various fuels [19]. This will in turn have an effect on emission production, especially NO_x.

1.5 HPDI Operation as a Driver for Natural Gas

As mentioned at the beginning of this chapter, NG is one such fuel that can reduce GHG emissions, specifically CO_2 emissions by approximately 20% [31], if used to replace traditional carbon based fossil fuels such as diesel. Other benefits of using

NG as a primary fuel for engines is that, because it is a gas, it possesses better mixing potential with air in the combustion chamber as compared to liquid fuels [57]. This, combined with the lack of carbon-carbon bonds leads to less PM formation, less UHCs, and less CO [71]. NG also has a lower adiabatic flame temperature relative to diesel which leads to overall lower NO_x emissions [54]. NG is also appealing as an alternative fuel choice due to the already existing infrastructure and reserves available [66, 67]. However, as mentioned in section 1.2.4, if methane emissions aren't mitigated, the use of NG in engines runs the risk of increasing total GHG emissions.

Westport Fuel Systems (WFS) has developed high-pressure direct-injection (HPDI) technology capable of injecting high-pressure NG directly into the combustion chamber of a CI engine [31]. This is different from dual-fuel port injected NG engines in that this uses high-pressure NG injected directly into the cylinder near top dead center. The injector consists of two concentrically mounted needles, each with its own actuating solenoid. One controls a pilot diesel injection followed by the other controlling the main NG injection.

The diesel pilot injection only serves as the ignition source for the NG and only provides approximately 5% of the total energy [22, 31, 49]. Studies have shown that the use of HPDI technology reduces methane emissions significantly as compared to dual-fuel port injected NG engine alternatives especially at low-load, lean operating conditions [26].

Another benefit of HPDI technology is that diesel-like efficiencies can be maintained [4]. This is because HPDI engines operate as CI engines, therefore, they are able to maintain higher compression ratios than premixed combustion engines. Conclusively, HPDI engines are capable of maintaining diesel-like efficiencies while reducing both GHG and pollutant emissions.

1.6 Previous Literature on NOx Behaviour in HPDI Engines

NO_x production, as well as in-cylinder NO_x reduction strategies, such as EGR, has been well studied and documented for diesel CI engines [11, 46, 55]. However, research has also shown that the nature of combustion for HPDI engines is signif-

icantly different from that of diesel engines, promoting more premixed combustion through the better fuel entrainment with air brought about by using a gaseous fuel [57]. These differences in combustion behavior between diesel and HPDI engines create the need for more research on understanding and characterizing NO_x formation in HPDI engines and how the effects of EGR affect NO_x production.

Previous literature shows that HPDI engines can produce less NO_x than diesel fuelled engines especially at higher loads due to the lower flame temperature of NG [31]. However, switching to HPDI technology with NG is not enough alone to meet today's NO_x standards. Other in-cylinder NO_x reduction strategies such as EGR must be employed to achieve the standards. Previous studies have investigated the effects of EGR on NO_x in HPDI engines [35, 51], but further experimental data is still needed to further identify the sensitivity of NO_x to the specific effects of EGR. This is especially important at higher EGR rates because previous research has shown that the reductions in NOx emissions are not nearly as dramatic at rates above 25% indicating that sensitivities are not equal across all EGR rates [51]. Because EGR can affect many aspects of combustion and engine performance, it is paramount that the manner in which EGR is used is well defined and as many engine parameters as possible are held constant to isolate the effects of EGR.

In terms of EGR, there are two methods of operation previously tested on HPDI enignes: replacement and supplemental as illustrated in Fig. 1.5 [51]. Replacement EGR adds exhaust gases to the intake fresh air charge while maintaining a constant intake manifold pressure. Supplemental EGR adds exhaust gases to the fresh air intake charge while maintaining a constant volume of fresh air. Replacement EGR requires less control and does not increase intake air temperatures as much as supplemental EGR. However, the equivalence ratio is affected by both of these methods of EGR.

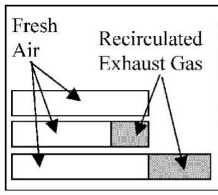

EGR Condition	Ingested mass (g/cycle)	EGR in charge (g/cycle)	O_2 Equi-valence Ratio	Ingested N_2 (mol%)	Ingested O_2 (mol%)	Ingested CO_2 (mol%)	Ingested H_2O (mol%)
0% EGR	3.6	0.00	0.53	79.0	21.0	0.00	0.00
20% Replacement	3.6	0.76	0.60	78.0	17.4	1.55	3.30
20% Supplemental	4.5	0.90	0.47	78.2	18.9	0.97	2.08

Figure 1.5: Replacement vs supplemental EGR where replacement EGR maintains manifold pressure and supplemental EGR maintains fresh air volume. Used with permission. Copyright © 2004, © SAGE Publications. [51]

The author has not found any studies that maintain a constant equivalence ratio while adjusting EGR rates. This would require a procedure similar to supplemental EGR where the intake pressure would have to be adjusted as EGR rates increase, but instead of maintaining a constant volume of air, a constant equivalence ratio would be maintained. This will be called constant ϕ EGR for this study. Previous literature demonstrates engine research that has used a design of experiments method to strategically perturb the overall engine system in such a way so that the influence of each individual input can be independently characterized [41]. The intent of maintaining a constant ϕ while only adjusting EGR is to provide a detailed mechanistic study of the effects of EGR while isolating other factors such as equivalence ratio.

EGR can also have an effect on engine performance metrics such as efficiency and combustion phasing. One previous study with EGR in HPDI engines has maintained engine speed, engine load, and injection timing constant, but the combustion phasing was not maintained [51]. Other studies have maintained combustion phasing by adjusting fuel injection timing, but only replacement EGR was utilized [35] thus affecting the equivalence ratio significantly. The author has not found research that experimentally explores the effects of EGR in HPDI engines for a constant equivalence ratio, engine load, and combustion phasing for all possible EGR rates up to the highest possible rates.

1.7 Objectives and Scope

While there are some studies that explore the effects of EGR on NO_x in HPDI engines, there are no studies showing experimental results of a complete EGR sweep holding equivalence ratio constant for the entire sweep. One study experiments with supplemental EGR, but the condition of the test facility only allowed for EGR rates up to 20% and this method did not maintain a constant combustion phasing throughout the sweep [51]. The more parameters that are held constant throughout an EGR sweep, the more isolated EGR becomes as the only factor of change. This allows for better understanding of how exactly EGR affects NO_x.

The overall objective of this research is to characterize NO_x formation in HPDI engines and identify the sensitivity of NO_x to different effects of EGR. This study can serve as a reference for NO_x mitigation strategies in alternative gaseous fueled direct injection engines. The three specific objectives to achieve this are as follows:

Objective 1: Develop a better understanding of the sensitivity of NO_x to the specific effects of EGR such as in-cylinder temperature, oxygen concentration and combustion duration.

Objective 2: Identify the limits of EGR as a NO_x reduction strategy based on trade-offs with combustion stability, CH_4 and PM emissions, and efficiency.

Objective 3: Develop a robust experimental HPDI EGR system capable of running and measuring high EGR rates up to $\sim$50% EGR while maintaining a constant equivalence ratio.

Chapter 2

Experimental Setup

All experiments for characterizing NO_x emissions in HPDI engines were performed using a single cylinder research engine (SCRE) in The Clean Energy Research Center (CERC) at The University of British Columbia (UBC). The details of the experimental lab including the research engine, data acquisition methods and instrumentation, emissions measurement methods, and engine operation strategies are discussed below.

2.1 Single Cylinder Research Engine (SCRE)

The SCRE is based on a 15 litre Cummins ISX400 inline six cylinder engine representative of engines used in heavy-duty trucks. The engine was heavily modified to allow for HPDI operation. This included the use of a WFS first generation HPDI injector and high pressure NG and diesel fuel lines connected to the fuel rails in the engine head.

The engine was further modified to allow for single cylinder operation by sealing the valves shut and using plugs in place of injectors on the other five cylinders to prevent any mass transfer. The pistons are still in place within the cylinders for engine balancing purposes. Previous studies using the SCRE have demonstrated similar performance to multi-cylinder equivalent engines [50]. Because only one cylinder is active, a major benefit is that smaller fuel systems are required and cylinder-to-cylinder variation is eliminated which could distort torque and/or emis-

sion measurements. An image of the SCRE and some of the main components of the engine can be seen in Fig. 2.1 and the specifications of the modified single cylinder engine can be seen in Table 2.1.

Table 2.1: SCRE specifications

Engine Parameter	Value
Compression ratio	17
Peak Cylinder Pressure (bar)	175
Clearance volume (m^3)	$1.55x10^{-4}$
Displacement volume (m^3)	24.9x10^{-}4
Bore (m)	0.137
Connecting rod length (m)	0.2615
Crank radius (m)	0.0845

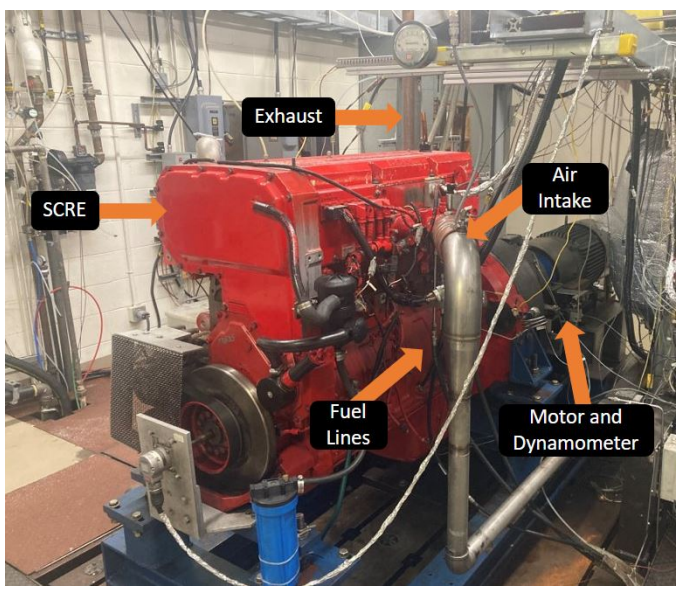

Figure 2.1: Detailed image of SCRE, dynamometer and motor all mounted in series with air intake manifold and exhaust only for one cylinder and fuel lines modified to carry high-pressure diesel and NG.

2.1.1 Dynamometer and Vector Drive Motor

To overcome the frictional losses of the other 5 non-firing pistons, a 30 kW electric motor is controlled by a vector drive to provide the necessary constant torque. A water-cooled eddy-current dynamometer is used in series with the electric motor to absorb the brake torque and to control the engine speed within 1% of the setpoint. A load cell mounted to the arm of the dynamometer was used to measure brake torque of the engine in addition to indicated work (discussed in section 2.3).

2.1.2 Air Exchange System

Figure 2.2 shows the air exchange system of the SCRE. The stock turbocharger was replaced with a stationary air compressor (Ingersoll-Rand, Model) to allow for more control over the intake air pressure independent of the engine operating condition. The compressor supplies a maximum pressure of 690 kPa to a computer controlled pneumatic regulator which reduces the maximum pressure to 300 kPa. A surge tank downstream of the regulator is used to damp the pulsations of the engine air exchange. The air flow rate is measured using a venturi and validated with a hot film sensor and is used to determine the equivalence ratio and exhaust flow rate. There is a burst disk rated to 300 kPa at 540 $^{\circ}C$ installed downstream of the vent from the intake surge tank. This is to protect the system from being over pressurized and further limits the intake pressures to 300 kPa.

The exhaust system is designed to allow for EGR operation and includes a surge tank on the exhaust flow to allow for the pulsations of the single cylinder gas exchange to be damped. When the back pressure valve seen in fig. 2.2 is fully open, the exhaust is fully vented to atmospheric pressure. The back pressure valve and the pneumatically controlled pressure relief valve can be used together to control the back pressure and to drive exhaust gases through the EGR cooler when the EGR valve is opened (further discussion on EGR control is discussed in 2.6). The EGR condensate trap (also discussed further in section 2.6) is a new addition relative to prior works using the same facility [50] and was added to prevent condensation of EGR water vapour in the engine intake and improve experimental repeatability. A burst disk with the same specifications as is in the intake system is used just downstream of the vent from the exhaust surge tank thus limiting the exhaust back

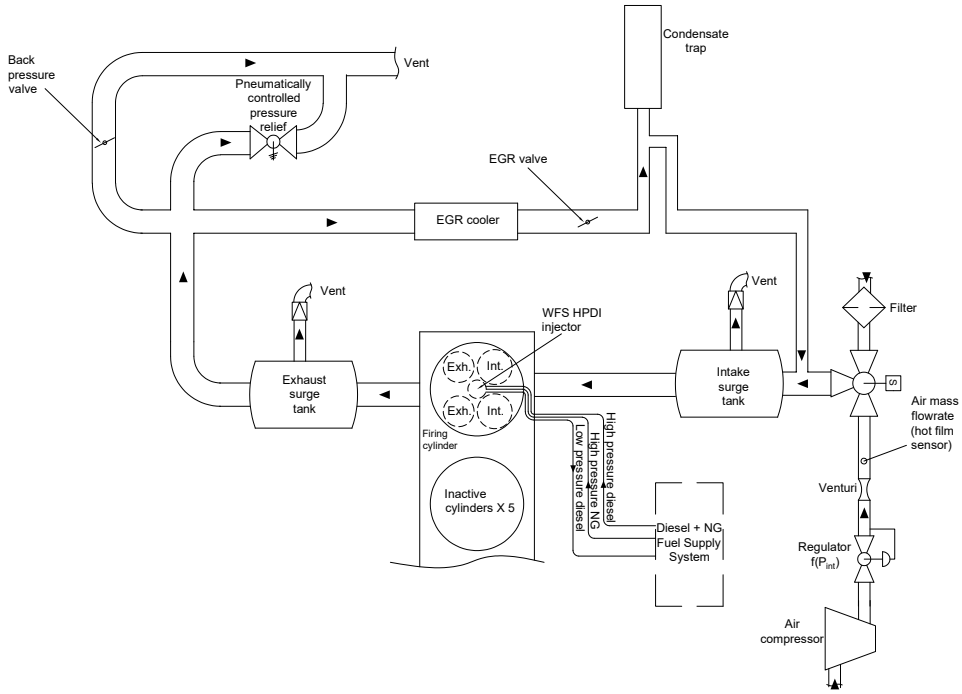

Figure 2.2: Piping and instrumentation diagram of the air exchange of the SCRE

pressures to 300 kPa as well.

2.1.3 Fuel System

Figure 2.3 shows a simplified diagram of the diesel and NG fuel system for the SCRE (more detailed P&ID in Appendix A). The NG was supplied by a stationary multi-stage screw compressor at pressures from 25-27 MPa. A pressure regulator was installed just downstream of the compressor (modified from previous versions of this fuel system [59]) to help damp the pulsations caused by the compressor. Another new addition to the fuel system is an excess flow valve just after the pres-

sure regulator for safety measures in case of a gas line rupture. The flow rate of the NG was then measured with a coriolis mass flow meter.

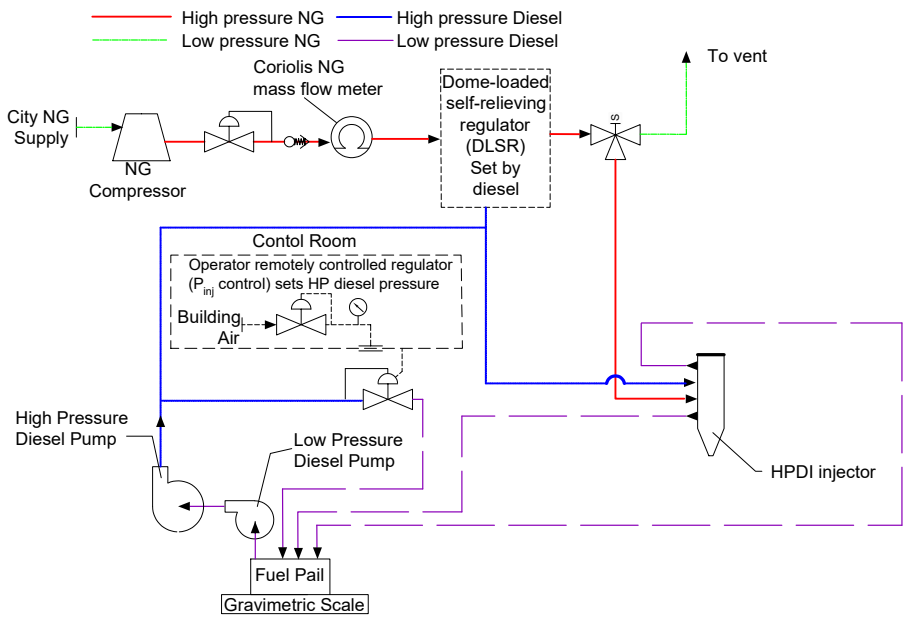

Figure 2.3: Piping and instrumentation diagram of the NG and diesel fuel system of the SCRE

The diesel was pumped from a gravimetric container by a low pressure pump to a high pressure bosch common rail pump. The change in mass of the gravimetric container is used to calculate diesel mass flow rate. The high pressure diesel is used to control the NG pressure up to the injector ($\sim$ 22 MPa for this research) with a dome loaded regulator. The diesel fuel is given a positive pressure bias (1.4 MPa and 0.8 MPa for when engine is running and not running respectively) to ensure NG will not leak into the diesel lines. The diesel pressure is regulated using compressed air.

During the time of research for this publication an injector failure was experi-

enced. Details of the failure and how the problem was resolved are in Appendix B. The symptoms of the failure were first noticed after the injector had been removed and reinstalled for the replacement of a new pressure transducer. The damaged injector was sent for diagnosis and repairs before eventually being reinstalled. All tests that were used for the data in this thesis used the repaired injector.

2.2 Data Acquisition and Instrumentation

The engine operation was controlled and the sensor and actuator signals were recorded using a National Instruments (NI) based data acquisition (DAQ) and control system. NI modules and chassis were used in conjunction with LabVIEW software. A more detailed description of the DAQ system can be found in previous works [49, 50] and fig. 2.4 shows the current DAQ hardware tower.

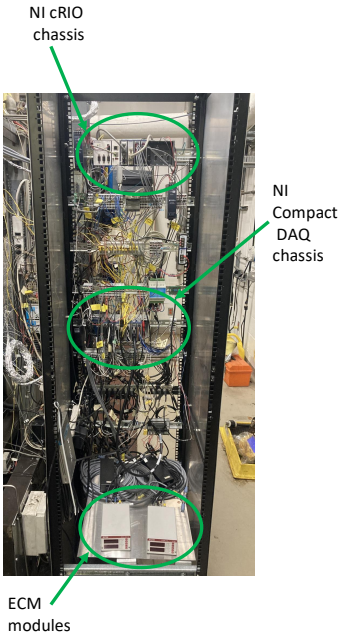

Figure 2.4: DAQ hardware tower containing National Instruments and ECM hardware

Cylinder pressure and intake manifold pressure were recorded at a frequency of 2 samples per crank angle degree (CAD). These were considered ”fast” data samples and all other data were recorded at a frequency of 10 Hz and was considered ”slow” data. From the control room, the engine operator was able to monitor both the ”slow” data virtually live while the ”fast” data was refreshed every second. Key parameters such as heat release rate (HRR), intake and exhaust pressures, and peak cylinder pressure (PCP) were constantly monitored to ensure safe and stable engine operation.

Oxygen and electrochemical NO_x sensors were installed (described in sections 2.6.2 and 2.4.2 respectively) as new hardware (as compared to the referenced DAQ in [49]). An additional ”slow” data module and corresponding plots were added to the DAQ chassis and LabVIEW virtual interface respectively for these additions. Other modifications to the DAQ system include the isolation and electromagnetic interference (EMI) shielding of the high speed cables to prohibit the EMI of the injector signal with the other high speed cables such as the crank and cam position sensors. Which otherwise would result in faulty engine speeds in the DAQ signals and cause an emergency shut down.

2.3 In-Cylinder Pressure Measurement

Measured emissions are typically normalized by measured work, but the majority of the experimental engine parameters defined in this work are as indicated values. This requires the use of a sensor with a fast response time because indicated work measurements are derived from the in-cylinder pressure measurements. The SCRE uses a flush mounted Kistler 6054C M5 pressure transducer which does not require water cooling. This replaced the Kistler water-cooled 6067C transducer used previously [59]. The function of the transducer is to produce a charge proportional to the pressure change. A Kistler 5018A charge amplifier is used to change the signal to a measurable voltage and account for signal decay. Because the in-cylinder sensor only measures change in pressure and is susceptible to drift, an initial starting pressure must be used to ”peg” the pressure measurement. A PCB piezotronics Model 1501C02EZ piezo-resistive transducer measures the intake manifold pressure at the same rate as the in-cylinder sensor and is used to peg the in-cylinder

pressure measurements. Every cycle, the in-cylinder pressure is pegged at the intake manifold pressure at the moment the intake valve closes (the moment when in-cylinder pressure is equal to intake manifold pressure).

The in-cylinder pressure measurements are used to calculate the indicated mean effective pressure (IMEP) which, due to the friction created by the 5 non-firing pistons, is more representative of the work produced by the fired cylinder than brake mean effective pressure (BMEP). The reported engine load is defined as gross indicated mean effective pressure (GIMEP) as seen in eqn. 2.1 below.

$$GIMEP = \frac{\int_{EVO}^{IVC} P(\theta)\, dV(\theta)}{V_d} \tag{2.1}$$

Exhasut valve open (EVO), Intake valve close (IVC) and displacement volume (V_d) are 150 crank angle degrees (CAD) after top dead center (TDC), 15 CAD after bottom dead center (BDC), and 2.49 litres respectively. $P(\theta)$ and $V(\theta)$ are the instantaneous cylinder pressure and volume measurements respectively at the corresponding CAD. GIMEP is used instead of net indicated mean effective pressure (NIMEP) (accounts for the pump work needed to be performed by the engine during the exhaust and intake strokes) because the pumping work will be affected by the other 5 inactive cylinders.

2.3.1 Heat Release Rate and Combustion Phasing

Apparent net heat release rate (HRR) is an important metric because it represents the sensible energy change and work transfer to the piston [34]. It can be calculated using the measured in-cylinder pressure based on the first law of thermodynamics and ideal gas law as seen in eqn. 2.2 below. The HRR represents the heat released due to combustion including the heat lost from heat transfer to the cylinder walls.

$$\frac{dQ_n}{d\theta} = \frac{\gamma}{\gamma - 1} p \frac{dV}{d\theta} + \frac{1}{\gamma - 1} V \frac{dp}{d\theta} \tag{2.2}$$

p is the in-cylinder pressure, V is the cylinder volume at crank angle degree θ, and γ is the specific heat ratio (1.3). It should be noted that γ is assumed to be constant in this calculation, but would actually vary with temperature variations in the cylinder.

The integral of the HRR was used to determine combustion timing and phasing. The point of 50% of the maximum integrated heat released (IHR50) was used as an indicator for combustion phasing. Because this engine uses two fuels, each with separate injections, both the diesel and NG injections needed to be adjusted to maintain constant combustion phasing. For the sake of consistency, the pulse separation (PSEP) between the diesel and NG injections was held constant. PSEP is defined as the time between the end of the pilot diesel injection and the start of the main NG injection. Therefore, both injections were adjusted to maintain combustion phasing, or IHR50.

2.4 Gaseous Emissions Measurement

The gaseous emissions were measured using a Bruker Matrix-MG5 Fourier Transform Infrared (FTIR) analyzer. The working principle of this FTIR is to draw exhaust gases at approximately 1 litre per minute (LPM) through the optical gas cell for infrared (IR) light to pass through. The optical cell has an effective IR light path length of 5 meters before reaching an interferometer which produces an optical signal. The exhaust gases absorb some of the IR light in the gas cell before it is detected by the interferometer thus creating a different optical signal depending on the absorption of the emissions gases. There is a fixed mirror and a moving mirror within the optical cell to provide interference so that spectral information can be extracted from a broadband light source. The following sections describe how the FTIR was fully commissioned for use as a gaseous emissions analyzer for this study.

2.4.1 FTIR Emissions Species and Concentration Selection

The Bruker MG-5 FTIR is optimized for fast gas exchange making it ideal for engine exhaust analysis, but the exact species to be analyzed had to be selected by the user. Therefore, it had to be fully commissioned for HPDI emission analysis prior to its use as the primary gaseous emissions analyzer for this research. The first step to commissioning the FTIR as a reliable gaseous emissions analyzer was to select the emissions species to be analyzed. This is necessary because the relevant spectral regions must be selected for the emission species and concentrations to

avoid interference from other species. An example of the optical image produced by the FTIR is shown in Fig. 2.5 where the exhaust sample image is in green, and an inert sample is in blue. Frequency ranges of high interference (highlighted in red) can be seen in the emission sample image. Each species of exhaust correlates to a frequency range of interference and it was the responsibility of the user to assign proper interference ranges for each species to be analyzed.

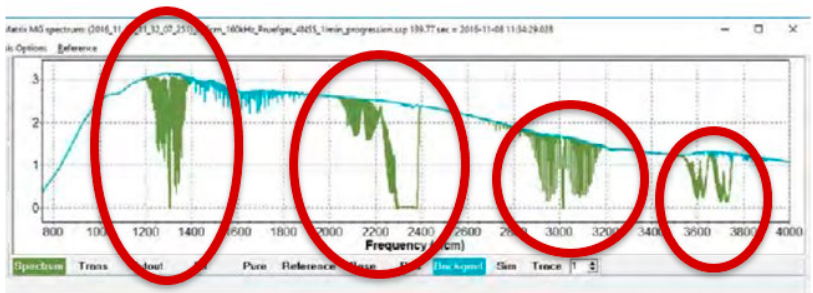

Figure 2.5: FTIR frequency interference of exhaust sample with high interference sections highlighted in red

Each species (ie. NO_x, CO, CH_4), and in some cases concentration of species, will absorb IR light differently, thus creating the need to assign interference frequency ranges for each desired emission species and concentration to be analyzed. Table 2.2 shows the species and their concentrations selected. Some species required more than one spectral range to be considered because the absorption created by the species would be in a different range for different concentrations. These species and range of concentrations were selected based on common emission species from previous research on the SCRE [59].

Table 2.2: Interference Frequency Range for FTIR Species and Concentrations

Species and Concentrations Analyzed	Interference Frequency Range (1/cm)
$CH_4 < 50$ ppm	3074-3115
$CH_4 > 50$ ppm	2690-2760
$NO < 500$ ppm	1899-1905
$NO > 500$ ppm	1944-1966
$NO_2 < 150$ ppm	1597-1600
$NO_2 > 150$ ppm	758-766
H_2O	1132-1190
CO_2	758-766
$CO < 400$ ppm	2110-2170
$CO > 400$ ppm	2020-2039
N_2O	1240-1265

2.4.2 FTIR Validation

The FTIR did not need to be calibrated because the output of the measurements were never adjusted. Only the configuration of the interference wavelengths were adjusted to give the correct output. Therefore, the FTIR was validated against known standard gases and against a trusted emissions analyzer, but not calibrated. First, gas standards of a known concentration were used to validate the frequency interference ranges selected by the user. Then, actual engine emissions were sampled in parallel with a trusted emissions analyzer and compared. This section will cover both processes.

Gas Standard Validation

Once the interference frequencies were selected for the emission species to be analyzed by the FTIR, gas standards of a known concentration for several different emission species were used to validate the FTIR and the assigned species. Table 2.3 shows the gases and concentrations selected for the validation process. Each gas is balanced with nitrogen.

Table 2.3: Calibration gases selected for validation of the FTIR and the assigned emission species

Calibration Gas	Concentration (ppm)
CO_2	830.0
CO_4	$1.310*10^5$
CO	300
NO	253.3
CH_4	120.1
CH_4	391.6
CH_4	100.4

The gases were each separately sampled through the FTIR at a flow rate of 1 LPM, and because the bottles were at a positive pressure, careful attention was given to ensure the FTIR gas cell pressure did not exceed 50 HPa over the calibrated 1013 HPa. This was accomplished, as seen in the pipe and instrumentation diagram (P & ID) in fig. 2.6, by setting the pressure regulators at the gas bottles to 10 psi maximum and using a needle valve upstream of a rotameter to lower the pressure.

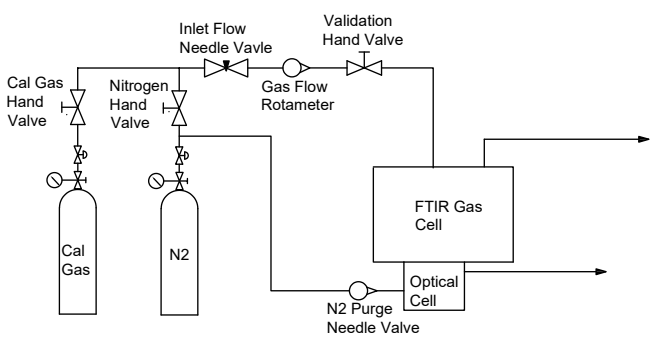

Figure 2.6: P & ID using calibration gases under pressure to validate the FTIR

Each gas was sampled through the FTIR for 4 minutes and the average recorded concentration from the FTIR was reported. This process was repeated 3 times on three different days in the months of October and November 2020. The results of the validation can be seen in fig. 2.7 with all gases reading within 7 per cent of the actual gas concentration in the bottle. This proved the frequency ranges selected for each species tested were resulting in valid concentrations.

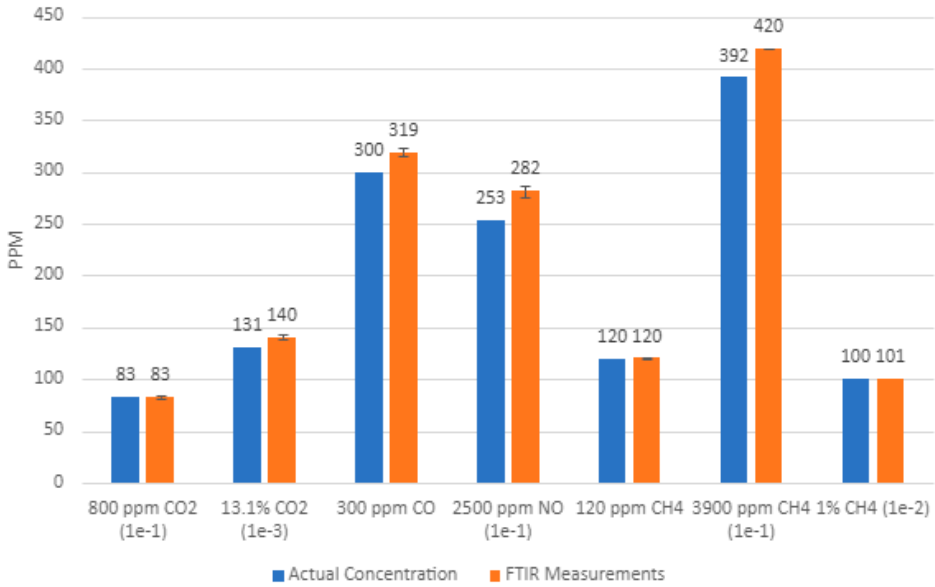

Figure 2.7: Validation of FTIR using calibration gases of known species and concentration

Emission Comparison Validation

The measurements of the FTIR were further validated using an emissions bench (AVL CEB II Emissions Bench). The AVL bench differs from the FTIR in that it uses several different instruments and techniques to measure different emission species. For example, it measures NO_x through the use of a chemiluminescence detector (CLD), CH_4 and UHCs with a flame ionization detector (FID), and CO and CO_2 with a nondispersive infrared sensor. Another difference is that the FTIR measures all emissions with water vapour still in the exhaust, while the AVL re-

moves the water vapour from the sample for CO and CO_2 measurements. This requires correction factors be applied when comparing these species of the two instruments. More detail on how each AVL instrument and technique measures each species can be found in [22].

The FTIR and AVL emissions bench were plumbed in parallel during emissions measurements as seen in fig 2.8. This parallel setup allowed the comparison of two identical gaseous emission samples through the AVL and FTIR. Results of the comparison between all emission species measured and recorded with the FTIR and the AVL can be found in Appendix C, but further explanation of how NO_x was validated is given here because it is the emission species of foremost concern for this work.

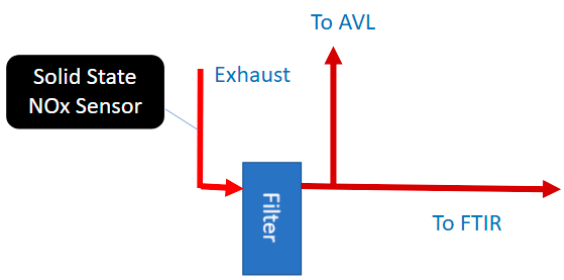

Figure 2.8: Parallel exhaust sampling to AVL and FTIR for further validation

Because the primary focus of this work is NO_x measurement and characterization, a third instrument was used to validate the NO_x emissions: a solid state electrochemical NO_x sensor (Engine Control and Monitoring (ECM), manufacturer) was installed in the exhaust within 24 inches of the exhaust valve to serve as a redundant comparison of NO_x emissions. First, the CLD requires that all the NO_x be converted to NO before being exposed to ozone [63]. Therefore, only NO and total NO_x is measured by the CLD whereas NO and NO_2 are explicitly measured by the FTIR. Second, the electrochemical sensor, as seen in fig. 2.9 works on the principle of first removing excess O_2 in a primary cell before the NO_x is diffused into a second cell. Here exists a reducing catalyst where the NO_x is reduced to N_2 and O_2. Because the excess O_2 in the exhaust was already removed, the pumping current of the second cell is proportional to the amount of oxygen produced from

the NO_x reduction [7].

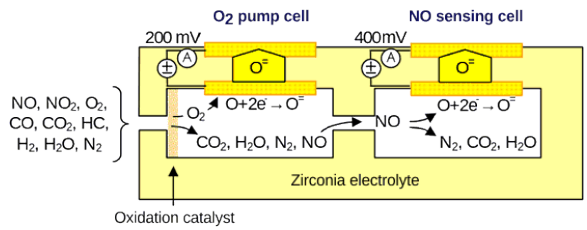

Figure 2.9: Schematic representation of NO_x sensor showing the two cells for oxygen removal then NO_x reduction. Used with permission. Copyright © ECOpoint Inc. Revision 2019.12 [7].

Another reason this sensor is attractive for this work, besides providing a third source of validation, is that it can record data at a faster rate than the FTIR so variations in tests can be tracked more easily. Also, electrochemical sensors are much easier to use in outside of laboratory based research so the results found here could be carried into the real world more easily. The results of this validation are found in chapter 4 and serve to help define measurement uncertainties.

2.4.3 Exhaust Sampling System

The FTIR measures the exhaust species with water vapor still in the exhaust sample, and unlike the AVL, all emission species are measured by one analyzer at a flow rate of 1 LPM. This means the water in the exhaust is never removed and creates the need to ensure no water can condense in the sampling system because water condensation was found to disrupt the emission species concentrations measured by the FTIR during preliminary testing.

To ensure no water condensation was trapped in the sampling system, first all sample lines and filters were heated to 191 $^{\circ}C$ to prevent the condensation within the tubing. The number of valves that were unable to be heated were kept to a minimum. Secondly, the flow of the sampling system was designed to prevent areas where water could become ”trapped” in the tubing. Lastly, water traps were installed at junctions where water had been found to condense previously. These consisted of a vertical volume of tubing with a hand valve at the bottom to be used to empty the trapped water in between tests. Figure 2.10 shows the piping and

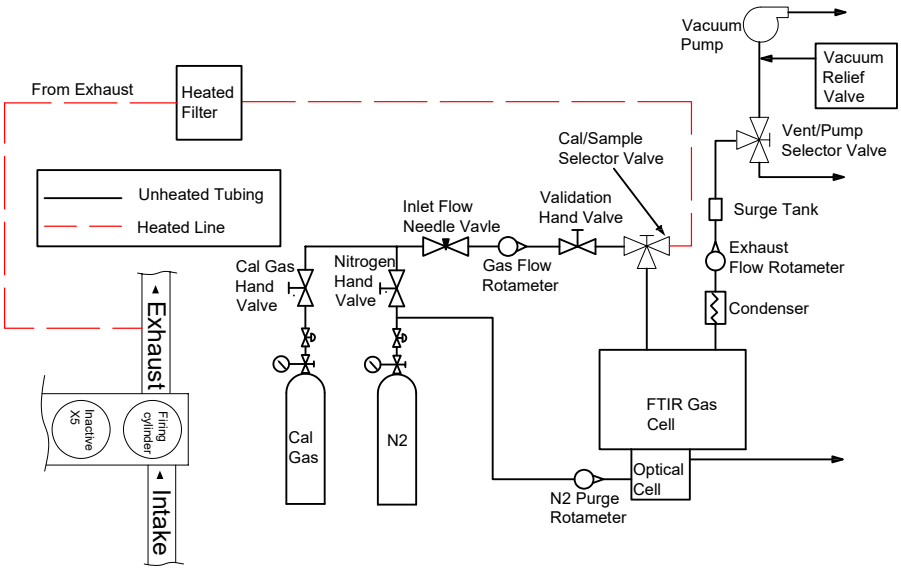

Figure 2.10: Schematic of the exhaust sampling system using the FTIR

instrumentation of the FTIR sampling system. The AVL has an internal pump, but the FTIR does not so an external pump was installed at the outlet side after a condenser to protect the pump from water.

2.5 Engine Operating Modes

A baseline operating condition was identified that provided representative PM and NO_x emissions at a medium-high load with liberty to employ significant EGR and/or equivalence ratio changes to reduce NO_x. The baseline condition for two different equivalence ratios is defined by the constant parameters specified in Table 2.4. These parameters were chosen based on former experiments performed on this engine with the intent to analyze PM emissions at high loads without exceed-

ing the peak cylinder limit of 175 bar [22]. Because intake pressure must increase with increased EGR rates to maintain a given equivalence ratio (see section 1.6), a slightly lower load (12 bar GIMEP instead of 16 bar) was selected for this experiment to prevent reaching the maximum intake pressure limit of 300 kPa. This also allows for higher EGR percentages at the relevant equivalence ratios while not exceeding the peak cylinder pressure limit of 175 bar.

Table 2.4: SCRE baseline constant parameters

Engine Parameter	Value
GIMEP (bar)	12
Engine Speed (rpm)	1300
IHR50 (ATDC)	10
PSEP (ms)	0.3
Gas Rail Pressure (MPa)	22
Equivalence Ratio	0.7 & 0.6

The EGR sweep was performed for each equivalence ratio by starting with 0% EGR and increasing by increments of 5% up until the constant parameters were not able to be maintained. This was done to find the limits of NO_x reduction in HPDI engines through the use of EGR. The desire was to reach 50% EGR because that is the maximum possible EGR in a wastegated turbocharger setup without having to add some sort of device capable of displacing the fresh air (intake throttke) [33]. The EGR rate was measured via O_2 sensors located at the intake and exhaust ports and is further discussed in section 2.6.

Because all the parameters in Table 2.4 were held constant during the EGR sweep, other parameters, such as the intake air and exhaust pressures, were adjusted. Similar to supplemental EGR methods (refer to section 1.6), the intake pressure was increased with increased EGR rates to maintain the equivalence ratio. The injection timings were advanced to maintain ignition timing of IHR50 = 10 CAD and the injection duration was decreased to maintain engine load as EGR rate was increased. The parameters that had to be adjusted by the user in order to maintain the constant parameters in Table 2.4 can be seen in fig. 2.11.

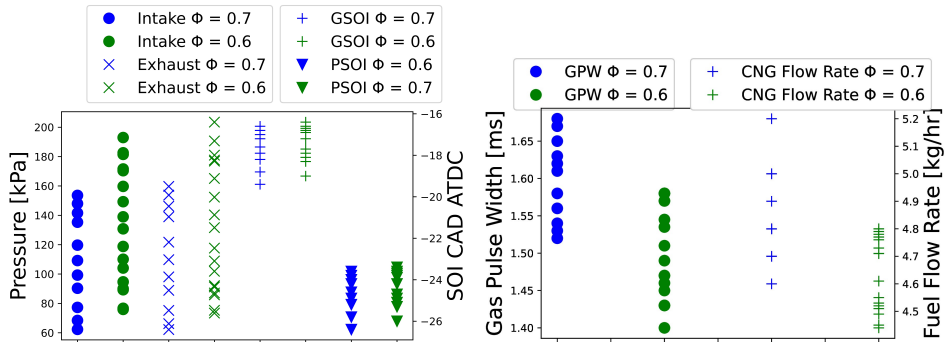

Figure 2.11: Plots showing variable parameters such as intake and exhaust pressures and injection duration and timing used to maintain the constant parameters in Table 2.4.

2.6 Exhaust Gas Recirculation (EGR)

The following sections outline the methods of measuring and validating EGR rate as well as evaluating the effects of varying EGR rates while maintaining engine load and equivalence ratio among other constants. As discussed in section 1.6, EGR, as defined by eqn. 2.3, has been shown to lower NO_x emissions in both diesel and HPDI engines. V_e and V_a are the volume exhaust and volume of fresh air in the intake respectively. EGR can be measured by mass concentrations or volume, and for this study the volumetric concentrations are used to allow for more direct comparison of different measurement instruments.

$$EGR = \frac{V_e}{V_a + V_e} \tag{2.3}$$

.

2.6.1 EGR Control

The EGR system on the SCRE differs slightly from the example shown in fig. 1.4 largely because there is no turbocharger. Previous research with the SCRE outlines the development of the original EGR system and control mechanisms incorporated [50]. The configuration of the EGR system is shown in fig. 2.2. The exhaust back pressure butterfly valve is used to set the exhaust back pressure to drive EGR

into the intake, similar to how a turbocharger would generate exhaust back pressure. The EGR flow control valve is then opened to allow for exhaust gases to mix with fresh intake air as long as the pressure ratio of exhaust to intake is equal to or greater than one. Due to the unstable, or nonlinear, flow control characteristic of the EGR valve, a pneumatically controlled wastegate valve is used to finely control the exhaust back pressure and thus finely control the EGR rate.

When running EGR with the SCRE, the user must first set the pneumatic back pressure wastegate to a value equal to or less than the intake pressure. Then the back pressure valve can be partially closed to match the exhaust pressure with the intake pressure (typically closed $\sim$90%). The control panel interface gives live feedback on the position of the wastegate valve so the user can know if it has reached its maximum limit of relief or if it is not having to relieve any pressure at all. Ideally, the wastegate valve is close to half way open before the EGR valve is opened by the user to ensure fine control of EGR is possible by adjustments made to the wastegate settings. The EGR valve is typically only opened 2.5% of the way and not adjusted during the EGR sweep because it is not very precise. The user can then finely control the EGR rate by fine adjustments to the wastegate valve.

A significant change on the most current EGR system is the addition of an EGR condensate trap. Due to the length of the intake pipe and size of the intake surge tank, it was observed that condensation would build up in the intake surge tank and intake pipe with high rates of EGR. This would cause an inconsistent EGR composition and induction of water into the engine and exhaust analyzers. There were also cases of the water freezing in the intake system overnight causing pipes to rupture. A condensate trap, as seen in Fig. 2.12 was installed immediately downstream of the EGR cooler to collect the condensation. It was designed to allow 50% EGR for up to one hour at a load 25% higher than what was tested in this work. It will better protect the engine and instrumentation from issues such as rust and flow restrictions caused by water buildup in the intake and exhaust lines. It will also provide more accurate and repeatable measurements with a more consistent EGR and fresh air composition.

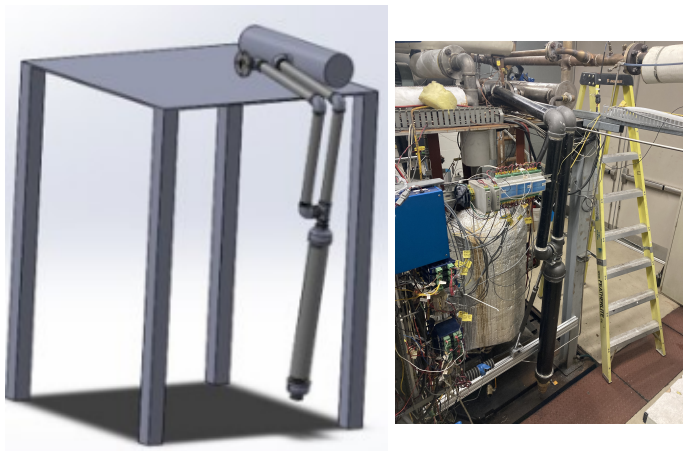

Figure 2.12: EGR condensate trap designed to prevent water condensation buildup in the intake surge tank and intake pipe due to high EGR rates

2.6.2 EGR Measurement

A common method of measuring EGR is by measuring the concentrations of CO_2 in both the exhaust and the intake. Equation 2.4 can then be used to determine the EGR rate [51] where $Y_{CO_{2i}}$, $Y_{CO_{2a}}$, and $Y_{CO_{2e}}$ are the volumetric concentrations of CO_2 in the intake, air, and exhaust respectively.

$$EGR_{CO_2} = \frac{Y_{CO_{2i}} - Y_{CO_{2a}}}{Y_{CO_{2e}}} \tag{2.4}$$

The procedure to measure the CO_2 based EGR rates using the FTIR is to first measure the total CO_2 emissions in the exhaust at a given operating point using the FTIR, then switch to measure the intake CO_2 at the same operating point. Figure 2.13 shows the P & ID of the FTIR sampling system for both exhaust and intake. Because the intake air is under pressure in the intake manifold, the design had to include a vent for the intake air in order to protect the FTIR from high pressures in the gas cell. Flow rates from the intake manifold were controlled at 1 LPM whether analyzing exhaust or intake.

As can be seen in fig. 2.13, both the exhaust and intake can be sampled, but must be done so separately because the FTIR only has one inlet. This requires the

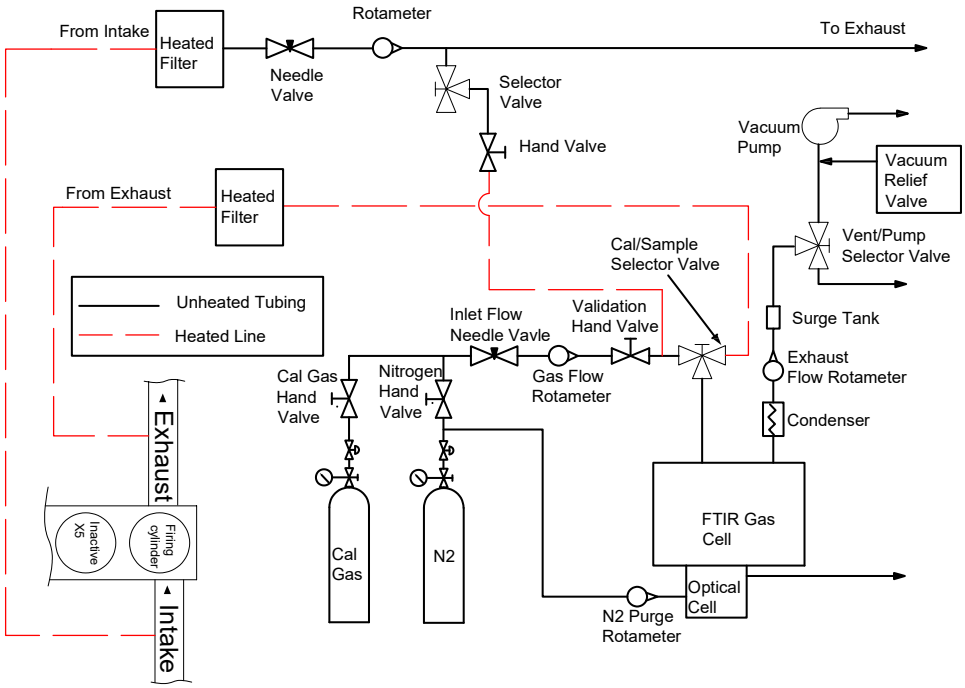

Figure 2.13: P & ID of the EGR validation using the FTIR

user to manually switch the three way valve between the exhaust sample and intake sample every time the sample source needs to be changed. If this was the only way to measure EGR, the valve would have to be manually switched for every operating point. This requires at least twice as much time for each operating point to ensure sufficient data is recorded for the intake sample and the exhaust sample. For this reason, an O_2 based EGR measurement system (ECM 5230) was implemented to provide faster and more accurate EGR rate measurements.

Electrochemical sensors not only provide a faster response time on EGR measurements, but can also be used in mobile applications making them an attractive alternative to gaseous EGR measurements for real-world applications. The O_2

based EGR measurement system on the SCRE consisted of two O_2 sensors, one mounted in the intake (downstream of the EGR introduction) and one in the exhaust system as seen in fig. 2.2. Pressure sensors are also installed next to the O_2 sensors for more accurate calculation of oxygen concentrations. The ECM module is then able to calculate an oxygen based EGR rate using eqn. 2.5 where $Y_{O_{2a}}$, $Y_{O_{2i}}$, and $Y_{O_{2e}}$ are the volumetric percentages of oxygen in the air, intake plus EGR, and exhaust respectively.

$$EGR_{O_2} = \frac{(Y_{O_{2a}} - Y_{O_{2i}})}{(Y_{O_{2a}} - Y_{O_{2e}})} \tag{2.5}$$

The EGR measurements O_2 sensors still needed to be validated using the more common and understood method of CO_2 based EGR measured via the FTIR. However, with the newly added condensate trap, the exhaust measurements for both O_2 and CO_2 contained water vapour (wet sample), but the intake sample did not (dry sample). This affected the measured results and corrections had to be made. Further discussion on the validation of the EGR measurements can be found in chapter 4 of this work.

2.7 Particulate Matter Measurement

To measure PM, the exhaust sample is first diluted before being analyzed by a TSI DustTrak DRX Model 8533 as demonstrated in fig. 2.14. It is required to dilute the sample in order to keep the PM concentration within the limits of the analyzer and prevent condensation and nucleation [56]. The sample is diluted with the same air that is used for the SCRE forced air intake. A California Analytical NDIR analyzer Model 100 is used to measure the diluted CO_2 concentrations. The dilution ratio is calculated using the CO_2 ratio between the diluted sample and the raw exhaust sample measured by the FTIR as described in section 2.4.

PM mass concentration is measured in diluted sample using a TSI DusTrak DRX Model 8533 which measures PM concentration through the use of light scattering. The calibration is based on Arizona Test Dust (ISO 12103-1 A1, TSI Incorporated, 2021a) which includes a large range of particle sizes (0.001 to 400 mg/m3). However, if the emission sample includes particle sizes outside of this range, the TSI DustTrak cannot read the mass concentrations correctly. (Previ-

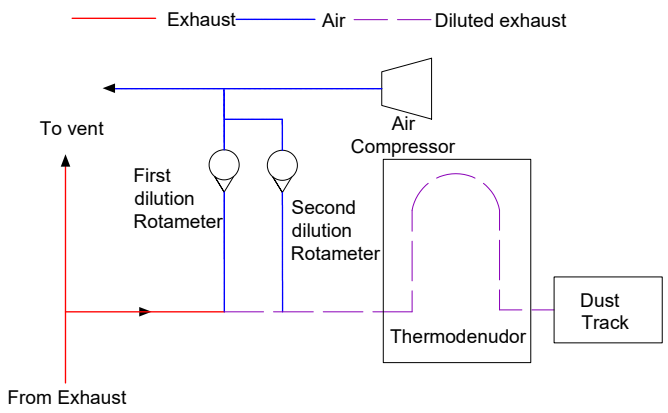

Figure 2.14: P & ID of particulate matter measurement using the DustTrak DRX 8533

ous research has shown the PM emissions from the SCRE fit well within this range [56]). The major benefit of the DustTrak is that it has a fast response time (1 second) and low cost.

2.8 Summary

In summary, a single cylinder research engineSCRE has been updated from previous research to include a more robust EGR system to allow for dry EGR with oxygen sensors in both the intake and exhaust to calculate EGR. An FTIR was commissioned to measure all gaseous emissions and also served as a tool to validate the oxygen based EGR measurements. The engine operation modes for an EGR sweep of two different equivalence ratios (0.6 &0.7) were established with constant parameters defined in Table 2.4. With the experimental state of the art defined, the next step is to numerically investigate EGR effects on simplified HPDI kinetics based models to support measured data from the SCRE.

Chapter 3

Kinetics Analysis of EGR Effects on NOx

The following chapter discusses how the effects of EGR, such as in-cylinder temperature, O_2 concentration, and combustion duration, affect NO_x through the use of a simplified kinetics analysis developed using the Cantera software package (more specifically the GRI- Mech 3.0, the 53-species, 325-reaction natural gas combustion mechanism was used within Cantera). These effects are analyzed using kinetics instead of equilibrium because the time required for NO_x to reach equilibrium is greater than the time allowed on engine timescales. However, the kinetic analysis is validated with equilibrium results. A kinetic analysis of a simplified representation of HPDI combustion, with the assistance of experimental data, can isolate some or all of the effects of EGR, which experimentally would all be dependent on EGR changes. This provides the knowledge of what effect has a more significant role in NO_x reduction and can be used to most efficiently reduce NO_x emissions in HPDI engines.

3.1 Purpose of Kinetic Analysis

The primary purpose of developing numerical models for this research is to isolate the effects of EGR (in-cylinder temperature, O_2 concentration, combustion duration) to determine the sensitivity of NO_x to those effects which could otherwise

not be independently adjusted experimentally. This was performed using a zero-dimensional kinetic analysis (developed using Cantera).

The models developed for this research are not an exact representation of HPDI combustion as measured from the SCRE. They are designed to function as a constant pressure reactor, but they do not have an ignition source or injection of fuel. There is also no transfer of mass, and the mixture is assumed to be homogeneous. However, similar trends were observed between the modelled results and some of the measured results, so the models can still provide insights to NO_x sensitivities to changes brought about by EGR.

A kinetic analysis was ultimately used over an equilibrium analysis in determining NO_x sensitivities because typical combustion duration times in an ICE tend to be much shorter than the time required for NO_x to reach equilibrium. The system is generally unsteady in the kinetic analysis, meaning all states are functions of time [27], so after the initial parameters, such as temperature, pressure, and reactants have been established, then the reaction can be analyzed over a defined period of time. If allowed enough time, the reaction will eventually reach equilibrium. For this purpose, an equilibrium analysis was used to validate the results of the kinetic analysis before further developments were made in isolating EGR effects.

EGR was implemented into the model to understand the effect it has on the kinetic process. Then, using measured data from the SCRE, parameters such as combustion duration time and temperature were isolated in isothermal and adiabatic versions of the kinetic analysis by defining them to match the measured data. By isolating such factors brought on by EGR, it was possible to determine the sensitivity of NO_x to specific effects of EGR.

3.2 Kinetic Analysis Development

Development of the kinetic analysis first began by selecting the proper reactor in Cantera and defining initial parameters. Cantera requires the use of predefined reactors to represent these time dependent chemically reacting systems. The reactor ”IdealGasConstPressureReactor” was chosen because it most closely matches HPDI combustion by simulating a constant pressure system for ideal gas mixtures. The state variables involved in this reactor are mass, m, (mass of the reactor’s con-

tents), temperature, T, and the mass fraction of each species, Y_k.

The volume of the reactor is not a state variable and it changes as a function of time in order to keep the pressure constant [27] which most closely represents the diesel cycle. The change of volume with respect to time is defined using eqn. 3.1 where $f_w = \pm 1$, indicating whether the wall is increasing or decreasing volume to maintain pressure. A_w and $v_w(t)$ represent the surface area of the wall and the velocity of the wall as a function of time respectively.

$$\frac{dV}{dt} = \sum_w f_w A_w v_x(t) \tag{3.1}$$

The reaction rate, or rate at which a given species, k, is generated is given in eqn. 3.2 where V represents the volume, $\dot{\omega}_k$ represents the net production rate of the given species, W_k represents the molecular weight of the given species, and finally, $\dot{m}_{k,wall}$ is the mass production rate for the given species at the wall.

$$\dot{m}_{k,gen} = V\dot{\omega}_k W_k + \dot{m}_{k,wall} \tag{3.2}$$

The energy equation, shown in eqn. 3.3, uses temperature as a state variable. Here $\dot{Q}$ is the net rate of heat addition to the system, and c_p and h are the specific heat capacity at a constant pressure and specific enthalpy for a given substance.

$$mc_p\frac{dT}{dt} = \dot{Q} - \sum_k h_k \dot{m}_{k,gen} + \sum_{in} \dot{m}_{in}(h_{in} - \sum_k h_k Y_{k,in}) \tag{3.3}$$

The reactants were defined as seen in eqn. 3.4. It should be noted that natural gas is used in the experiments, but because methane makes up over 90% of natural gas, it is being used as the fuel for the model for further simplification. This will have minor effects on factors such as flame temperature and ignition rate.

$$aCH_4 + b(O_2 + 3.76N_2) \tag{3.4}$$

Fuel was set to remain constant (a=1) while the molar quantity of air was modified to consider different equivalence ratios as defined in eqn. 3.5.

$$\phi = \frac{(\frac{fuel}{air})}{(\frac{fuel}{air})_{stoich}} \tag{3.5}$$

The molar coefficient b was defined to account for this change in air as seen in eqn. 3.6 where 2 is divided by the equivalence ratio (ϕ) because the stoichiometric molar ratio of air to fuel for methane is 2 to 1.

$$b = \frac{2}{\Phi} \tag{3.6}$$

The initial parameters of the kinetic analysis (temperature, pressure, reactants) were defined to most closely represent the conditions of the SCRE prior to fuel injection. In addition to these initial parameters, a time interval also needed to be defined for the reactor. An isobaric, adiabatic, kinetic simulation of stoichiometric methane-air mixture is shown exemplarily in Fig. 3.1 over a time span of 0.07 seconds. Following from left to right, the flame temperature (thick pink dashed line) initially rises slowly before reaching a maximum around 2500K. CH_4 and O_2, the green and brown lines, decrease sharply near the same time the temperature rises sharply and CO_2, the purple line, increases from zero. This indicates oxidation is taking place.

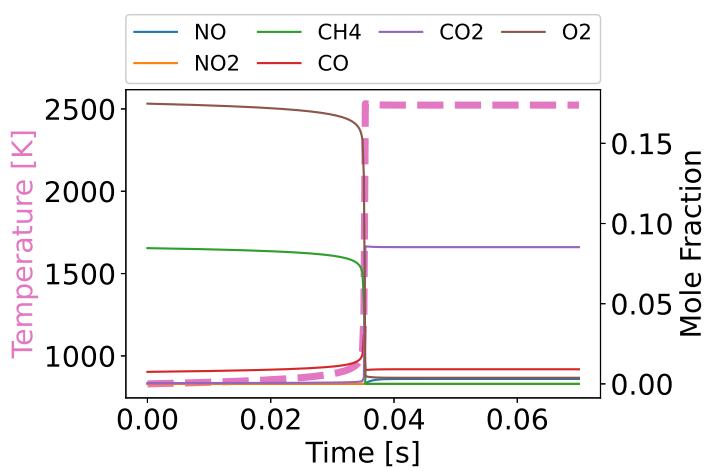

Figure 3.1: Isobaric, adiabatic, kinetic simulation of stoichiometric methane-air mixture showing dependency on time.

Because the kinetic analysis is a function of time, the final products of the simulation are a function of time and need to be defined as such. This example shown in Fig. 3.1 of a kinetic simulation of a stoichimetric CH_4-air mixture gives sufficient

time for the reaction to reach a state of equilibrium. This is verified by comparing the final products of the kinetic analysis to the products of an equilibrium analysis (discussed further in section 3.3). Becasue NO_x does not reach equilibrium in HPDI engines due to insufficient time (see section 1.2.1), the time constraints for the simulation have to be adjusted to more closely represent HPDI combustion duration characteristics (ie. the model will not reach equilibrium).

To define combustion duration time, the start of ignition must first be defined. This is the moment ignition occurs spontaneously, or without any external energy source. In a diesel CI engine, ignition would occur with the introduction of high pressure fuel being injected into the cylinder at a high temperature and pressure. Because the simulation does not account for the injection of fuel, the time of autoignition is defined as the moment the modelled temperature reaches its maximum temperature [9]. From the temperature vs time plot in Fig. 3.1 it can be seen that this time of autoignition is about t = 0.035 seconds for the stoichiometric CH_4-air kinetic simulation. It is from this point of autoignition that combustion duration time will begin. The total duration time will be representative of the time where in-cylinder temperatures of the SCRE are within the Zeldovich threshold temperature (discussed further in section 3.4).

3.3 Equilibrium Analysis for Validation of Kinetic Analysis

The purpose of an equilibrium analysis in this study is to validate the kinetic analysis at the point of equilibrium. To do this, a simulation was created to bring the defined reactants to a state of equilibrium. The initial parameters and reactants were defined to be identical to those defined in the kinetic analysis in section 3.2 which were representative of the SCRE prior to injection of fuel.

To define the thermodynamic state of the mixture requires two independent and intensive properties, as well as the mixture composition. Specific enthalpy and pressure were chosen to be fixed parameters for this model because that most closely represents the thermodynamic diesel cycle with constant pressure heat addition. While this is not an exact representation of HPDI combustion, the alternative would be to select a constant volume and internal energy system. This would

assume infinitely fast combustion and produce much higher NO_x emissions because of it. The first law of thermodynamics can be used, as in eqn. 3.7, to further explain the constant enthalpy heat addition process in the diesel CI cycle where there is a change of internal energy (ΔU) brought about with heat addition (q) and work (w) done on the piston.

$$\Delta U = q - w \tag{3.7}$$

For the initial states defined above, the equilibrium NOx concentration for an isobaric and isenthalpic process was evaluated for a range of equivalence ratios, as shown in Fig. 3.2a. This was used to compare to the kinetic NO_x concentration of a time sufficient enough to reach a state of equilibrium for a range of equivalence ratios, as shown in Fig.3.2b. The simulation time here for the kinetic simulation is significantly longer than a typical combustion event in an engine. However, this is done for demonstration purposes to compare the kinetic and equilibrium analyses, as shown in Fig. 3.2. While Nox concentrations generally agree for equilibrium and kinetic solutions, the agreement is less pronounced at an equivalence ratio $\leq$ 0.5 indicating that the kinetic mechanism is less accurate for predicting equilibrium compositions for these lean conditions.

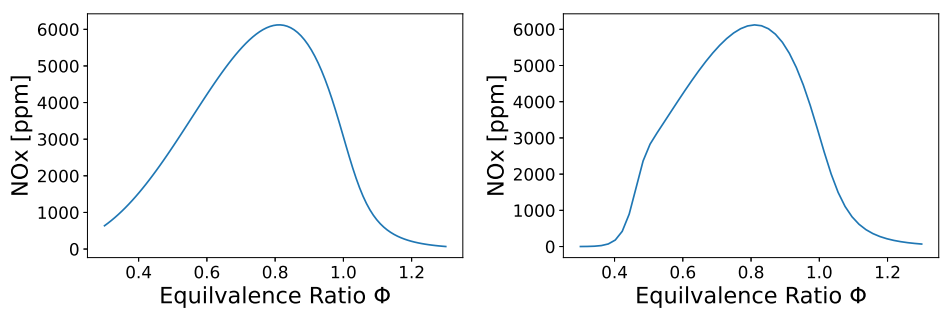

(a) Equilibrium NOx

(b) Kinetic NOx

Figure 3.2: NO_x vs ϕ for an equilibrium analysis and for kinetics analysis with a time sufficient enough to reach a state of equilibrium (b). NO_x concentrations generally agree for equilibrium and kinetic solutions, with the exception at an equivalence ratio $\leq$ 0.5.

3.3.1 Implementation of EGR into Models

Incorporating EGR into the kinetic analysis was the next crucial step in determining how it affects NO_x. The composition of EGR was defined in terms of products of combustion. For simplicity, complete combustion was assumed resulting in only carbon dioxide, water, nitrogen, and excess oxygen for lean conditions. This definition of exhaust products can be seen in eqn. 3.8 with the molar coefficient, χ, multiplied across the products to represent the molar quantity of EGR in the reactants.

$$\chi[CO_2 + 2H_2O + 7.52N_2 + (\frac{2}{\phi} - 2) * (O_2 + 3.76N_2)] \tag{3.8}$$

If the molar coefficient, χ, were equal to 1, meaning all of the exhaust is being recirculated into the intake, then the total EGR fraction (according to eqn. 2.3) would be approximately 52%. This is because the exhaust volume is equal to the intake volume plus the added fuel. Therefore, the molar coefficient was defined as a function of nominal EGR rate to be easily implemented into the kinetic analysis, as shown in eqn. 3.9.

$$\chi = \frac{\%EGR(\frac{2}{\phi} + \frac{7.52}{\phi})}{(1 - \%EGR) * (3 + (\frac{2}{\phi} - 2) + \frac{7.52}{\phi})} \tag{3.9}$$

Because there is excess air in the EGR for lean conditions, a corrected equivalence ratio (Φ_c) also had to be calculated and incorporated into the model. This corrected equivalence value was calculated as seen in eqn. 3.10. This differs from the normal equivalence ratio in that this accounts for the oxygen in the recirculated exhaust.

$$\Phi_c = \frac{1 + \chi}{\frac{1}{\Phi} + \chi} \tag{3.10}$$

By implementing EGR into the kinetic analysis, the effects of EGR can be analyzed as a function of time, as shown in Fig. 3.3. The initial conditions, temperature and equivalence ratio, were modified to show four different scenarios of a kinetic analysis of an EGR sweep. By setting the initial time as the point of autoignition as defined in section 3.2, each case begins combustion at the time equal to 0 seconds. As expected, lower EGR rates and higher initial temperatures produce higher NO_x

concentrations, but to better understand the sensitivities of NO_x to the effects of EGR, effects such as temperature and combustion duration must be isolated. This can be done using measured data from the SCRE.

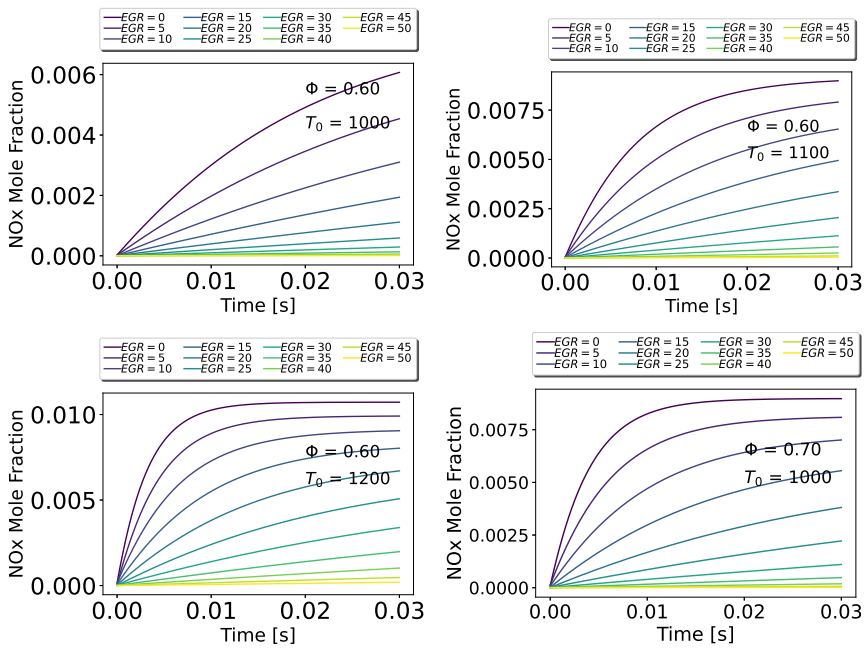

Figure 3.3: NOx vs time for a set time of 0.03 seconds after auto-ignition with different initial temperatures and equivalence ratios.

3.4 Isothermal vs Adiabatic Kinetics Based Models

While the kinetic analysis with EGR can help better understand how EGR affects the NO_x formation in HPDI engines with relation to time, all the effects of EGR, such as reduced oxygen concentrations, and decreased in-cylinder temperatures and combustion duration, are playing a role. To analyze the outcome each specific effect of EGR has on NO_x reduction, the other effects need to be isolated, or held constant. O_2 concentration is already held constant for each equivalence ratio and EGR rate. Time can be isolated by selecting one time frame (0.03 seconds for example) within the adiabatic model. Temperature can be held constant by isolating the temperature in an isothermal environment.

To analyze the effect of decreased in-cylinder temperatures brought about by increased EGR rates has on thermal NO_x reduction, specific combustion duration times must be assigned to each EGR rate being analyzed. These times are representative of the time above the Zeldovich threshold temperature of 1700K and can be estimated using the ideal gas law and measured in-cylinder pressures from the SCRE.

Figure 3.4 shows what estimated temperature profiles based on in-cylinder measurements would look like and the red line indicates the thermal NO_x threshold. The combustion duration would be defined as any time where the temperature is above that threshold for each EGR rate (indicated as the black bracket). An adiabatic analysis can then be performed for several different initial temperatures and the NO_x results can then be plotted against the adiabatic final temperatures to observe the effect temperature reduction through the use of EGR has on NO_x.

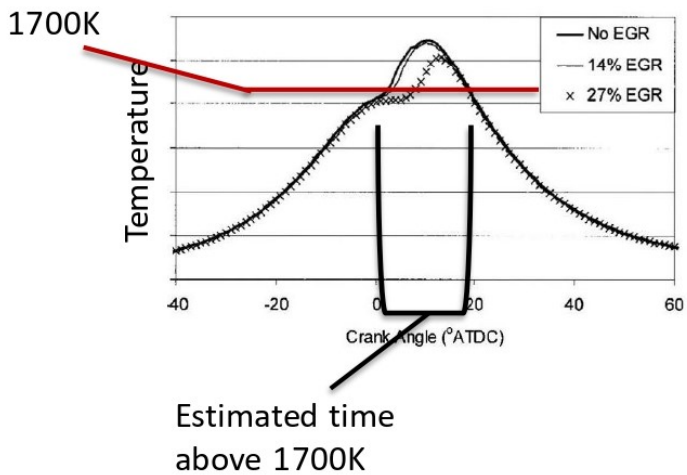

Figure 3.4: Estimation of in-cylinder temperatures with the combustion duration time labeled. The red line is added to represent Zeldovich threshold temperature of 1700K.

To analyze the effect of reduced O_2 concentration brought about by increased EGR rates has on thermal NO_x reduction, both the time and temperature need to be isolated. Time can be isolated, again, by assigning each EGR rate a representative time of estimated in-cylinder temperatures above 1700K. Temperature can be held

constant by assigning an isothermal environment to the analysis. This, however, does not represent the estimated temperature profile where temperatures rise and fall within the combustion duration time. To resolve this issue, each temperature profile estimated from in-cylinder pressure measurements are used as inputs to a sequential series of isothermal kinetic analyses. This is illustrated in Fig. 3.5 where the temperature profile is broken into segments to represent a constant temperature and set time. The summation of NO_x from each segment would represent the total NO_x for that EGR rate.

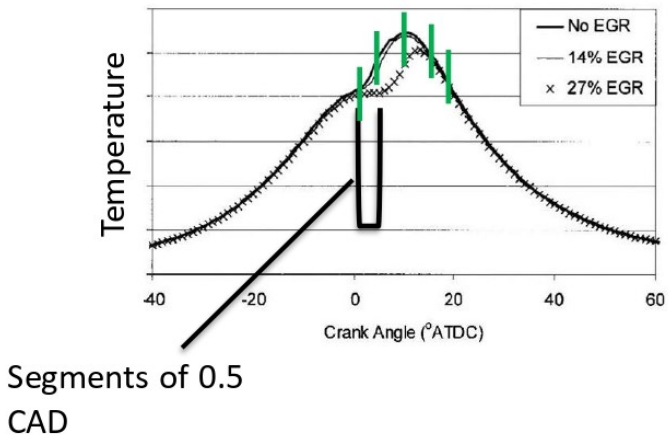

Figure 3.5: Estimation of in-cylinder temperatures. The green segments represent sections of the temperature profile held constant for 0.5 CAD in the isothermal reactor.

Further investigation into these two methods of isolating certain effects of EGR to identify NO_x sensitivities will be presented in chapter 4.

Chapter 4

Interpretation of Kinetic and Experimental Analyses

A kinetic analysis on the effects of EGR on NO_x was performed using measured data from an experimental EGR sweep to represent initial conditions. The measured data was incorporated into the models presented in Chapter 3 to more fully understand the sensitivity of NO_x to EGR. Other factors, such as adiabatic flame temperature and oxygen concentration, were examined to determine what role they play in NO_x formation in HPDI engines. The effectiveness of the newly developed emissions measurement and EGR systems was reviewed by examining the precision and uncertainty of the systems. The precision was defined using the comparison of one measurement source measured with different measurement tools and techniques, while the uncertainty was defined using the largest standard error found from either systematic or statistical errors. An EGR sweep performed at varying equivalence ratios was carried out to identify it's limits for engine-out NO_x emissions.

4.1 Effectiveness of Emissions Measurement System

As mentioned in chapter 2, many changes were made to the SCRE EGR system and data collection hardware especially in regards to emissions measurements. The following sections discuss the benefits of a new EGR condensate trap that was

installed to prohibit water getting trapped in both the exhaust sampling system and in the intake of the engine. A detailed analysis used to validate the new dry EGR system follows. Also discussed are the improved performance of the FTIR as an emissions analyzer and the measures taken to ensure the measurements were accurate and repeatable by using redundant sensors throughout the system. Lastly, the uncertainty of all of these measurements including those of the new in-cylinder pressure transducer is analyzed.

4.1.1 EGR Validation

To validate the ECM 5230 EGR Module, the recorded EGR rates are compared to the the FTIR CO_2 based EGR measurements as described in section 2.6.2. However, with the condensate trap implemented into the EGR system, the EGR measurements for both measurement methods now report values based on dry intake samples and wet exhaust samples. This creates discrepancies between the two measurements because the EGR 5230 system is designed to report ”wet EGR” [18]. These discrepancies can be seen in fig. 4.1 showing the parity between the FTIR CO_2 based EGR measurements vs the ECM O_2 based measurements. Equations 2.4 and 2.5 are used to calculate the CO_2 and O_2 based EGR rates respectively.

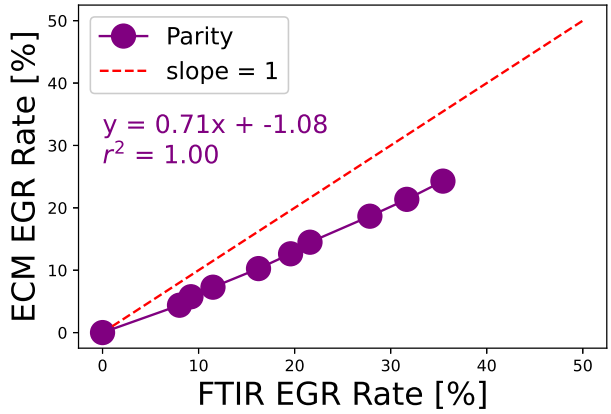

Figure 4.1: Results between FTIR CO_2 based EGR measurements vs ECM O_2 based EGR measurements show poor parity without any corrections to the recorded data.

Although the R^2 value is equal to 1 in Fig. 4.1, there is a 29% constant difference in the data (due to the slope of the line being 0.71) so it is obvious some correction factor or factors need to be applied to the measured data to improve the parity. This section describes the methods used to validate the dry EGR readings of the ECM EGR 5230 system using the FTIR sampling system described in section 2.6.2.

Volumetric EGR **Calculations**

Because most emission measurements were measured on a volume basis for this research, the following definitions and derivations of how EGR was calculated and validated are all on a volume/molar basis. All nominal values for volumetric EGR measurements were within 4% of the mass based EGR measurements, so not much variance should be seen in comparison to other works using a mass based system. These same calculations could be performed on a mass basis by applying the molecular weights or known masses to each species.

The definition for EGR on a volume basis is given in eqn. 4.1 below where V_e is the volume of exhaust in the intake and V_a is the volume of air in the intake.

$$EGR_v = \frac{V_e}{V_a + V_e} \tag{4.1}$$

This equation assumes all the water in the exhaust has been retained and thus would be considered "wet" EGR and can be rewritten as eqn. 4.2 to represent wet exhaust measurements in the intake, while eqn. 4.3 represents dry exhaust measurements in the intake.

$$EGR_{v_w} = \frac{V_{e_w}}{V_a + V_{e_w}} \tag{4.2}$$

$$EGR_{v_d} = \frac{V_{e_d}}{V_a + V_{e_d}} \tag{4.3}$$

A simplified chemical reaction shown in eqn. 4.4 can represent the reactants and products involved in the intake and exhaust of the HPDI engine with no EGR. All the species to the right of the arrow represent the products of combustion and a

portion of these can be recycled back into the exhaust to introduce EGR.

$$\mathrm{CH_4} + (\frac{2}{\phi}) \cdot (\mathrm{O_2} + 3.76\,\mathrm{N_2}) \longrightarrow \mathrm{CO_2} + 2\,\mathrm{H_2O} + 7.52\,\mathrm{N_2} + (\frac{2}{\phi} - 2) \cdot (\mathrm{O_2} + 3.76\,\mathrm{N_2}) \tag{4.4}$$

Equation 4.5 is a simplified representation of only the reactants of HPDI combustion with EGR.

$$\mathrm{CH_4} + (\frac{2}{\phi}) \cdot (\mathrm{O_2} + 3.76\,\mathrm{N_2}) + \chi[\mathrm{CO_2} + 2\,\mathrm{H_2O} + 7.52\,\mathrm{N_2} + (\frac{2}{\phi} - 2) \cdot (\mathrm{O_2} + 3.76\,\mathrm{N_2})] \tag{4.5}$$

χ is the molar number of reciculated exhaust gas, EGR, in the intake and is calculated using eqn. 3.9 shown in section 3.3.1.

Now using eqns. 4.2 and 4.4 one can solve for the molar "wet" EGR rate for a given equivalence ratio and χ value as seen in eqn. 4.6. The molar values for each species can be used to then calculate the volumetric EGR rate.

$$EGR_w = \frac{\chi[CO_2 + 2H_2O + 7.52N_2 + (\frac{2}{\phi} - 2) * (O_2 + 3.76N_2)]}{(\frac{2}{\phi}) * (O_2 + 3.76N_2) + \chi[CO_2 + 2H_2O + 7.52N_2 + (\frac{2}{\phi} - 2) * (O_2 + 3.76N_2)]} \tag{4.6}$$

For the dry measurements, only the water needs to be removed from eqn. 4.6 giving eqn. 4.7. These two values can then be compared to give a ratio between wet vs dry EGR rates. The value will vary depending on the equivalence ratio and measured EGR rate.

$$EGR_d = \frac{\chi[CO_2 + 7.52N_2 + (\frac{2}{\phi} - 2) * (O_2 + 3.76N_2)]}{(\frac{2}{\phi}) * (O_2 + 3.76N_2) + \chi[CO_2 + 7.52N_2 + (\frac{2}{\phi} - 2) * (O_2 + 3.76N_2)]} \tag{4.7}$$

Within the experimental bounds of equivalence ratios and EGR rates, a value of 1.11 $\pm$0.04 was calculated as a ratio between wet vs dry EGR using this method of calculating volumetric EGR rates. The largest ratio value correlates to the lowest EGR rate at ϕ = 0.7 and the lowest correlates to the highest EGR rate at ϕ = 0.6. When this factor was applied accordingly to the ECM measurements, the parity improved by approximately 7% between the FTIR and ECM EGR measurements. However, the parity can be improved further still. As stated in section 2.6.2, EGR is measured either via a CO_2 based method or oxygen concentration method rather

than on volumes of exhaust and intake. Because this wet vs dry EGR correction method only uses the assumed volumes of exhaust and intake, further calculations are necessary to fully validate the wet vs dry EGR measurements.

CO_2 Based EGR Calculations

Equation 4.8 (also eqn. 2.4) is used to calculate EGR using CO_2 concentrations of both the intake and the exhaust.

$$EGR_{CO_2} = \frac{Y_{CO_{2i}} - Y_{CO_{2a}}}{Y_{CO_{2e}}} \tag{4.8}$$

In order to further investigate wet vs dry EGR both the intake and exhaust CO_2 measurements need to be defined as seen in eqns. 4.9 and 4.10 respectively where $V_{CO_{2_i}}$ and $V_{CO_{2_e}}$ are the volume concentrations of CO_2 in the intake and exhaust and V_i and V_e are the total volumes of intake and exhaust respectively.

$$Y_{CO_{2_i}} = \frac{V_{CO_{2_i}}}{V_i} \tag{4.9}$$

$$Y_{CO_{2_e}} = \frac{V_{CO_{2_e}}}{V_e} \tag{4.10}$$

Using eqns. 4.4, 4.5, 4.9, 4.10 one can form eqns. 4.11 and 4.12. Again, these assume the sample to include water thus making them "wet" CO_2 mole fractions. To calculate the dry EGR rates one must simply remove the H_2O from the equation giving $CO_{2_{i_d}}$ and $CO_{2_{e_d}}$. When comparing wet vs dry EGR rates in this manner, a ratio of 1.11 $\pm$0.02 is found just as with calculating based on volumes only. This is to be expected as this method assumes both the intake and exhaust to be dry.

$$Y_{CO_{2_i}} = \frac{\chi * CO_2 + CO_{2_a}}{(\frac{2}{\phi}) * (O_2 + 3.76N_2) + \chi[CO_2 + 2H_2O + 7.52N_2 + (\frac{2}{\phi} - 2) * (O_2 + 3.76N_2)]} \tag{4.11}$$

$$Y_{CO_{2_e}} = \frac{CO_{2_e}}{CO_2 + 2H_2O + 7.52N_2 + (\frac{2}{\phi} - 2) * (O_2 + 3.76N_2)} \tag{4.12}$$

One major difference between comparing dry vs wet EGR using the CO_2 based calculations over using only volumes of intake and exhaust is that now the intake species only represent dry EGR while the exhaust remains wet (contains water

vapour). This is possible because it is a comparison of the exhaust measurement to the intake measurement unlike eqn. 4.1 where it is only a theoretical measurement of the intake volume percentages. Using only dry intake is also more representative of the actual measurements because the exhaust sample is wet and the intake sample is dry. This calculation of the FTIR representative EGR measurement is shown in eqn. 4.13

$$EGR_{FTIR} = \frac{Y_{CO_{2_{i_d}}} - Y_{CO_{2_a}}}{Y_{CO_{2_{e_w}}}} \tag{4.13}$$

Calculating EGR with dry intake and wet exhaust gives a higher EGR rate than wet EGR by a factor of 0.87 $\pm$0.04. When this factor is applied to the FTIR measurements even better parity exists between the ECM and FTIR EGR measurements. Still further agreement can exist between the two measurements though, and because the ECM module uses an oxygen based measurement, further calculations are needed to find better parity.

O_2 Based EGR Calculations

Equation 4.14 (also eqn. 2.5) is used to calculate EGR using oxygen concentrations of the exhaust and intake.

$$EGR_{O_2} = \frac{(Y_{O_{2a}} - Y_{O_{2i}})}{(Y_{O_{2a}} - Y_{O_{2e}})} \tag{4.14}$$

Similarly as with CO_2 based EGR, both the intake and exhaust oxygen concentrations need to be defined as seen in eqns. 4.15 and 4.16. Again, it is assumed that water is retained for both the exhaust and intake in these equations so they would represent "wet" EGR.

$$Y_{O_{2_i}} = \frac{\chi * [(\frac{2}{\phi} - 2) * O_2] + \frac{2}{\phi} * O_2}{(\frac{2}{\phi}) * (O_2 + 3.76N_2) + \chi[CO_2 + 2H_2O + 7.52N_2 + (\frac{2}{\phi} - 2) * (O_2 + 3.76N_2)]} \tag{4.15}$$

$$Y_{O_{2_e}} = \frac{(\frac{2}{\phi} - 2) * O_2}{CO_2 + 2H_2O + 7.52N_2 + (\frac{2}{\phi} - 2) * (O_2 + 3.76N_2)} \tag{4.16}$$

Removing the water would give $O_{2_{i_d}}$ and $O_{2_{e_d}}$ for the intake and exhaust respectively, but just as with the CO_2 based EGR calculations, only the intake mea-

surements are dry. The more accurate representation of EGR as measured by the ECM module would be as seen in eqn. 4.17. This gives a higher value than what is measured by the ECM module.

$$EGR_{ECM} = \frac{O_{2_a} - O_{2_{i_d}}}{O_{2_a} - O_{2e_w}} \tag{4.17}$$

The ratio between actual measured ECM EGR and calculated EGR using eqn. 4.13 is 1.19 $\pm$0.04. When this factor is applied to the ECM measurements and the factor of 0.87 $\pm$0.02 is applied to the FTIR EGR measurements almost perfect parity exists as seen in fig. 4.2. These correction factors are then applied to the ECM EGR measurements in post processing and analysis of the data.

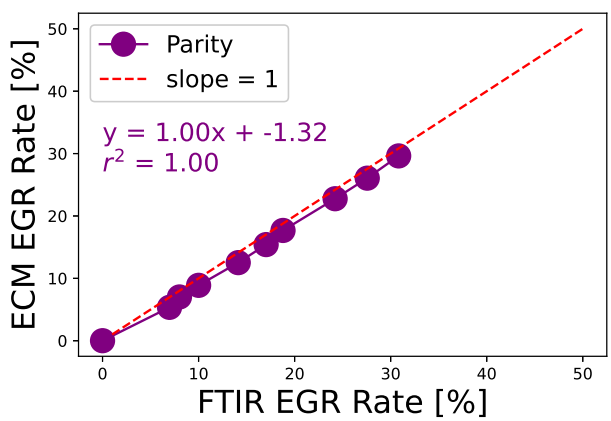

Figure 4.2: Parity between corrected FTIR CO_2 based EGR measurements vs correcrted ECM O_2 based EGR measurements showing almost perfect parity

The parity established between the CO_2 based EGR measurements of the FTIR and O_2 based EGR measurements of the elctrochemical O_2 sensors validates the use of electrochemical sensors for EGR measurements. This is beneficial for this work because this provides a much more efficient manner to measure and record EGR as compared to switching between intake and exhaust samples on the FTIR. Also, beyond this work, the use of electrochemical sensors can be used in field measurements much more easily than using an FTIR due to their smaller physical footprint. They are also capable of dynamic measurements with a much faster

response time than the FTIR.

4.1.2 Emissions Validation

Section 2.4.2 describes the method of using an AVL CEB II emissions bench and electrochemical NO_x sensor to validate the FTIR emissoins measurements and this section reviews the validation. Figure 4.3 shows the comparison of NO_x measured by the FTIR vs the AVL CLD sensor and vs the electrochemical sensor. With a slope of nearly 1 for each case, near perfect agreement is found between two different NO_x measuring techniques thus validating the measurements of the FTIR. It should be noted that the two plots do not represent the same data set because the ECM electrochemical NO_x sensor was not implemented into the system until after the AVL stopped working. However, the FTIR was used for both data sets and they each cover a wide range of NO_x emissions to validate the entire range of NO_x measurements of the FTIR.

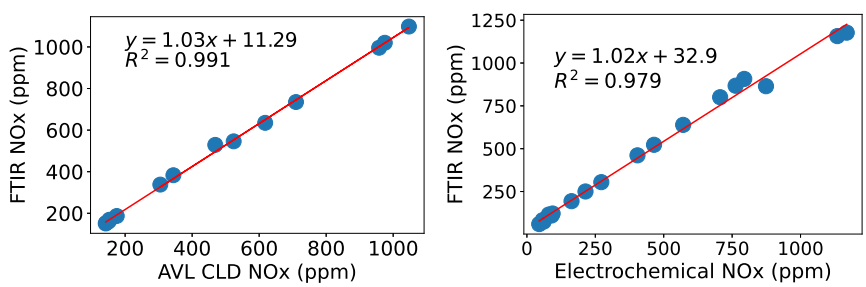

Figure 4.3: FTIR vs AVL CLD and ECM electrochemical NO_x measurements with a slope and R^2 value of nearly 1 validating the FTIR as a reliable emissions species analyzer

Other emissions such as CO_2 and CO were also compared to the AVL before moving solely to the FTIR for emissions measurements. CH_4 was also compared to the AVL as well as the measurements of a wavelength modulation spectroscopy device developed by other researchers at UBC for measuring high concentrations of methane [61]. The details of these comparisons can be found in appendix C.

4.2 Measurement Uncertainty

After the devices used to measure EGR and emissions have been validated against other instruments, it is necessary to review the uncertainty of all measurements for this research. This section discusses the uncertainty of the measurements for two main categories: 1) systematic uncertainty, being a source of the limitations of the instruments used; and 2) statistical uncertainty related to the variations between and during tests. The largest form of uncertainty is reported in the results.

4.2.1 Systematic Uncertainty

Systematic uncertainties originate from the instruments used to measure the SCRE outputs when their measurements differ from the actual values. This includes emissions, engine load, and exhaust and intake pressure measurements among others.

As discussed in sections 2.4.2 and 4.1.2, NO_x emissions were compared to the ECM solid state sensor as well as the chemiluminescence detector (CLD) in the AVL CEB II bench in which all three sensors showed close agreement. CH_4 emissions measured from the FTIR were compared to the results of the flame ionization detector (FID) of the AVL CEB II bench and also showed good agreement. CO and CO_2 FTIR measurements were also compared and showed good agreement to the AVL CEB II bench where it uses nondispersive infrared (NIR) sensors.

All sytematic uncertainties from the ECM hardware were found from their respective manufacturers' manuals [18] and [17]. All measurements normalized by brake work originate from the measured torque at the dynamometer as discussed in section 2.1.1. The systematic uncertainties for brake measurements thus come from the Omega load cell specifications [53]. As discussed in section 2.3 all indicated loads are derived from in-cylinder pressure measurements, therefore, the systematic uncertainties of all indicated measurements are a factor of the Kistler 6054C pressure transducer specifications [44].

All systematic uncertainties and their source of uncertainty can be found in Table 4.1. The emissions' systemic uncertainties arise from comparisons to gas standards, whereas the systemic uncertainties for the other measurements listed are reported by the manufacturer.

Table 4.1: Instrumental Uncertainties

Parameter	Source	Uncertainty
GIMEP	Kistler 6054C Pressure Transducer	$\pm 1.5\%$
Maximum P_{cyl}	Kistler 6054C Pressure Transducer	$\pm 1.0\%$
BMEP/Brake Torque	Omega Load Cell	$\pm 0.02\%$
EGR Rate	ECM 5230 Module	$\pm 0.5\%$
ϕ	ECM O_2 Sensor	$\pm 0.9\%$
O_2 Concentration	ECM O_2 Sensor	$\pm 0.1\%$
NO_x	FTIR/ECM Electrochemical/AVL CLD	$\pm 0.072\%$
CH_4	FTIR/AVL FID/WMS	$\pm 0.034\%$
CO_2	FTIR/AVL NDIR	$\pm 0.019\%$
CO	FTIR/AVL NDIR	$\pm 0.045\%$

4.2.2 Statistical Uncertainty

Statistical uncertainty emerges from a sample size of measurements of the same process over a period of time. Two types of samples were considered for this analysis: 1) the sample over the period of time data was recorded for a single steady-state test and 2) the sample of multiple tests recorded on different days for the same operating point.

Firstly, the data measured and recorded over the span of one steady state engine test (defined as exhaust temperatures measured upstream of the exhaust surge tank to have less than 10 $°C$ variation) was analyzed and defined as temporal uncertainty. The measurement frequency and time of data recorded for the DAQ and FTIR is shown in Table 4.2. During the 90 seconds of recording time, the FTIR recorded the average of 150 data points 3 times thus creating a sample size of 3, over the span of 90 seconds. The DAQ has ”fast” and ”slow” data as defined in section 2.2.

Table 4.2: Instrumental Measurement Information

Instrument	Measurement Frequency	Time Span
FTIR	5 Hz	90 seconds
DAQ (slow)	10 Hz	30 seconds
DAQ (fast)	2 $\frac{samples}{CAD}$	30 seconds

Secondly, several test points were repeated on different days to provide a sec-

ond sample size for an uncertainty analysis defined as repeatability uncertainty. Three operating points were selected from each equivalence ratio EGR sweep to represent no EGR, medium EGR and high EGR rates. These points were repeated two to four times thus creating the sample ranging from two to four.

Lastly, the standard deviation was calculated with eqn. 4.18 where x_i is each value from the sample population and μ is the population mean. N represents the two different sample sizes from the different time periods.

$$\sigma = \sqrt{\frac{\sum(x_i - \mu)^2}{N}} \tag{4.18}$$

The standard error was then calculated using eqn. 4.19. Because the standard error was so small for most metrics measured, the standard deviation is what is plotted in the figures in this chapter.

$$SE = \frac{\sigma}{\sqrt{N}} \tag{4.19}$$

The uncertainty was found to vary for each equivalence ratio more than it did for varying EGR rates. Because of this, each metric for a given equivalence ratio was assigned the largest source of uncertainty to represent the final uncertainty in the results of this research. Table 4.3 shows the final standard deviations and errors for the metrics used in the analysis of this work and from what source the uncertainty was the largest.

Table 4.3: Statistical Uncertainties

Parameter	Largest Source of Uncertainty	σ		SE	
		$\phi = 0.6$	$\phi = 0.7$	$\phi = 0.6$	$\phi = 0.7$
GIMEP	Temporal	0.17 bar	0.51 bar	0.12 bar	0.23 bar
Max P_{cyl}	Temporal	1.4 bar	1.6 bar	7.6 kPa	8.4 kPa
BMEP	Temporal	0.24 bar	0.28 bar	0.17 bar	0.15 bar
Torque	Temporal	112 Nm	106 Nm	6 Nm	6 Nm
EGR Rate	Repeatability	0.34%	1.6%	0.24%	0.88%
ϕ	Repeatability	0.063	0.0048	0.002	0.003
O_2%	Repeatability	1.5%	0.42%	0.04%	0.23%
NO_x	Temporal	0.35 ppm	1.82 ppm	0.2 ppm	1.1 ppm
CH_4	Temporal	2.15 ppm	10 ppm	1.24 ppm	5.77 ppm
CO_2	Temporal	14 ppm	58 ppm	8 ppm	34 ppm
CO	Temporal	288 ppm	323 ppm	166 ppm	180 ppm

4.3 Incremental Constant ϕ EGR Experimental Results

The engine performance and emissions were measured for HPDI combustion at a representative operating condition, with EGR rates from 0% to nearly 50% EGR. This was performed at two different equivalence ratios while maintaining engine load and combustion phasing among other constants as outlined in table 2.4. These measurements will be evaluated here to identify the influence of EGR on NO_x emissions and to identify the EGR limits as a NO_x reduction strategy at the specified operating condition (Section 2.5). Further, these measurements are interpreted using the kinetic analysis techniques presented in chapter 3 to isolate factors of EGR effects such as in-cylinder temperatures, combustion duration, and oxygen concentrations. The following sections discuss the limitations of EGR in HPDI engines, the effects of EGR rates on engine performance/efficiency, and NO_x and other emissions.

4.3.1 EGR Limitations

With the improvements made to the SCRE cell as outlined in chapter 2 and section 4.1.2, EGR rates were able to be reached up to nearly 50% while maintaining a constant equivalence ratio. Previous research in the same facility has not shown the impact of supplemental EGR on NO_x reduction beyond the rate of approximately 20% [51]. There is not a lot of explanation for why that was the limit other than due to experimental limitations. Key factors that assist in reaching high EGR rates as compared to experiments performed previously in this lab are listed in Table 4.4. Dry EGR eliminates water impeding the intake flow which otherwise would have caused engine failures. These tests were not carried out to maintain a constant volume of fresh air as is defined for supplemental EGR, instead they maintained a constant equivalence ratio. The O_2 in the EGR is accounted for in equivalence ratio measurements which allows for lower intake manifold pressures and thus allows for higher EGR rates before reaching the maximum pressure limit of 300 kPa. Lastly, using electrochemical O_2 sensors instead of gaseous CO_2 analyzers to measure EGR allows for more efficient measurements. This is especially advantageous when operating at less stable conditions (high EGR rates) becasue less time is required to collect the needed data.

Table 4.4: Benefits Achieved from Upgraded EGR System

Factor in EGR Improvement (Cause)	Effect
Dry EGR	Eliminates water buildup in the intake system and provides consistent EGR composition.
Constant ϕ	In comparison to supplemental EGR, slightly lower intake manifold pressures are required.
Electrochemical sensor	More efficient measurements of EGR allow (especially helpful at more unstable condtions).

As EGR rates increase, the oxygen concentrations of the intake decrease and results in decreased combustion stability. This instability can be seen by using the coefficient of variation (COV) as defined in eqn. 4.20. In this case, σ, as defined in eqn. 4.18, and $\bar{x}$ are the standard deviation and mean respectively of all the peak cylinder pressures or IMEP values for every engine cycle in the 30 seconds of data

for each steady state operating condition.

$$COV = \frac{\sigma}{\bar{x}} \tag{4.20}$$

Figure 4.4 shows the COV for both equivalence ratios. In general, an increase in EGR and EQR both result in increases in the COV, with EGR rates $> 35\%$ resulting in the most significant increases. Decreased O_2 concentration and temperature play a role in the increase of instability at higher EGR rates.

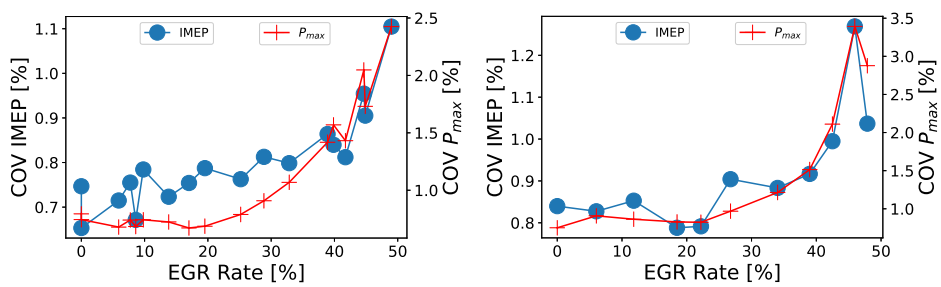

(a) ϕ = 0.6 **(b)** ϕ =0.7

Figure 4.4: Coefficient of variability for maximum cylinder pressure and indicated mean effective pressure. Higher EGR rates induce more combustion instability witnessed in a higher COV for both in-cylinder pressure and IMEP with higher variability seen for the more fuel rich condition (b) as compared to ϕ = 0.6 (a).

As EGR rates increased, the intake and exhaust pressures were increased to maintain a constant equivalence ratio. The increase in intake pressure required a decrease in fuel consumption to maintain a constant load. Finally, with decreased oxygen concentrations and increased diluent, the timing of fuel injections had to be advanced to maintain the combustion phasing. (The details of these variable user inputs used to maintain the controlled fixed parameters are seen in fig. 2.11 with the fixed parameters seen in Table 2.4). Eventually, the EGR rate became too high to maintain constant combustion phasing because it was no longer responsive to changes in injection timing. The limit of EGR as a NO_x reduction strategy was defined as the maximum EGR rate possible while still maintaining combustion phasing among the other constants. However, nearly 50% EGR was achieved which was the target for this study because this is the maximum possible EGR in a

wastegated turbocharged engine setup [33].

4.3.2 Constant ϕ EGR Impact on Engine Performance

While one of the main objectives of this work is to determine how EGR effects NO_x in HPDI engines, other factors such as engine performance and efficiency cannot be overlooked. As was discussed in section 2.5, injection timing and intake and exhaust pressures were adjusted to maintain the constant parameters in Table 2.4. This has an effect on engine performance and efficiency. The following sections discuss how varying EGR rates using the constant ϕ EGR (constant equivalence ratio, engine load and combustion phasing) affects factors such as in-cylinder pressures, heat release rates and indicated efficiency.

Impact of Constant ϕ EGR on Igniton Timing

Peak cylinder pressures are affected by constant ϕ EGR rates primarily due to the impact it has on ignition timing. Peak cylinder pressure in CI engines is highly dependent on the premixed combustion phase (for HPDI engines this would be the combustion of the NG), which is significantly affected by ignition delay [1]. Longer ignition delays lead to a higher accumulation of mixed fuel with air, and combustion occurs closer to TDC which both lead to higher peak cylinder pressures. Decreased O_2 concentrations, caused by increased EGR rates, lead to increased ignition delay [55] which ultimately leads to higher peak cylinder pressures. This effect can be seen in Fig. 4.5 where the peak cylinder pressures for each ϕ increase with increasing EGR rates.

Intake manifold pressures also have an effect on peak cylinder pressures as can be seen by the higher peak cylinder pressures for $\phi = 0.6$ which had a higher overall intake manifold pressure than for $\phi = 0.7$ (this effect is also seen in the pressure vs volume plots shown in appendix D). Using a constant ϕ EGR technique as a NO_x reduction strategy could lead to exceeding engine peak cylinder pressure limits if not monitored carefully. That is why the medium load of 12 bar GIMEP was selected for these tests.

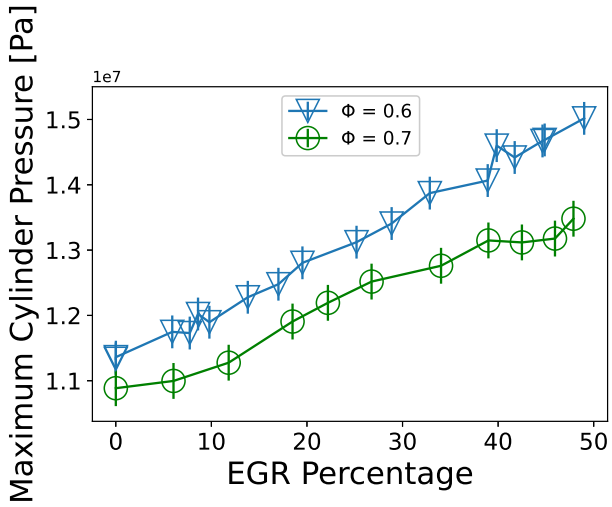

Figure 4.5: Peak cylinder pressure vs EGR rate. Increased peak cylinder pressures were caused by ignition delay and increasing intake manifold pressures.

Increasing constant ϕ EGR also has an effect on heat release rates (HRR) as shown in Fig.4.6 where the HRR is delayed with increasing EGR rates. This effect is brought on by ignition delays similar to how peak cylinder pressures are increased. Even though injection timing is advanced with increased EGR rates to maintain combustion phasing, ignition timing is delayed resulting in higher peak pressures, but constant phasing (appendix E).

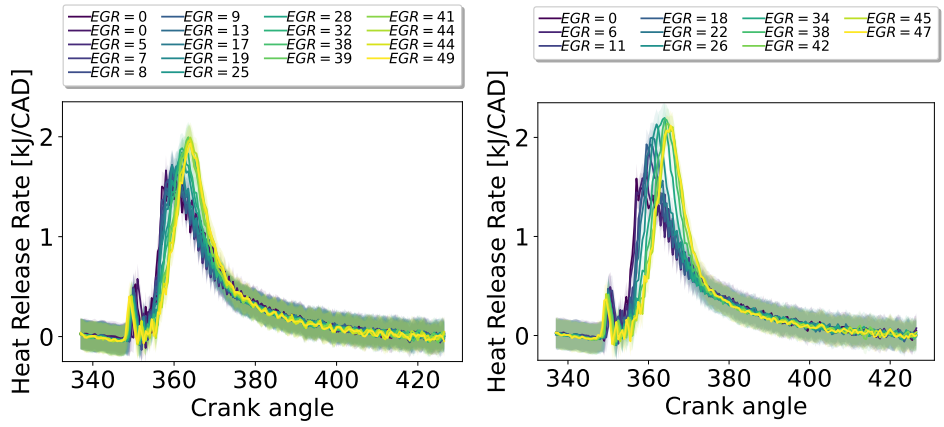

(a) ϕ = 0.6 **(b)** $\phi = 0.7$

Figure 4.6: Heat release rates for both equivalence ratios and each EGR rate. Delayed HRR is caused by ignition delay which also promotes a higher peak HRR.

Effects of Constant ϕ EGR on Gross Indicated Engine Efficiency

Increased constant ϕ EGR rates increased engine gross indicated efficiency by $\sim$ 3% for each ϕ as shown in Fig. 4.7. Gross indicated efficiency was calculated using eqn. 4.21 where m_f is the mass of fuel per engine cycle and lhv_f is the lower heating value of the fuel.

$$\eta_i = \frac{GIMEP * V_d}{m_f * lhv_f} \tag{4.21}$$

Because delayed ignition caused by increased EGR rates caused increased peak cylinder pressures, less fuel was required to maintain a constant engine load leading to higher gross indicated efficiency. Another factor is that higher EGR rates produce lower in-cylinder temperatures (discussed further in section 4.4.1) thus reducing heat transfer losses and increasing efficiency.

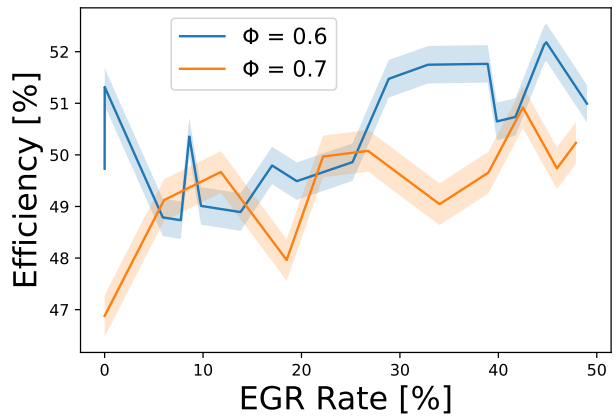

Figure 4.7: Indicated efficiency versus EGR rate. An increase of ∼3% is observed for each ϕ partly due to reduced heat transfer losses.

4.3.3 Indicated Specific Emissions

The emissions reported in this section are specific to the indicated power output rate of one hour. Equation 4.22 was used to convert the volumetric emissions measured by the FTIR to represent indicated specific emissions in the units of $\frac{g}{kW*hr}$. Y_{em} represents the emissions measured from the FTIR on a molar basis and M is the molar mass of the emission species. The exhaust flow rate is represented by $\dot{m}_{ex}$ and is calculated assuming the conservation of mass of the measured air intake and fuel flow rates. m_{ex} is the sum of all exhaust masses including air, and P is the indicated engine power output.

$$em_{spec} = \frac{Y_{em} * M * \dot{m}_{ex}}{m_{ex} * P} \tag{4.22}$$

Because of the single cylinder nature of the SCRE and reliance on the vector motor drive, specific emissions are calculated using indicated power calculated from the in-cylinder pressure as shown in eqn. 4.23. GIMEP is defined in section 2.3 with eqn. 2.1 and V_d, N and n_c are the volume displaced, engine speed and number of revolutions per power stroke respectively.

$$P_i = \frac{GIMEP * V_d * N}{n_c} \tag{4.23}$$

The influence of EGR on the indicated specific emissions for NO_x (ISNOx), CH_4 (ISCH$_4$), CO (ISCO), and PM ($\frac{mg}{mm^3}$) is shown in Fig. 4.8. For both equivalence ratios, ISNOx decreases linearly with increased EGR rates until an approximate 80% reduction (∼25% EGR) of the non-EGR ISNOx levels. More than another 15% further reduction occurs at higher EGR rates up to 50%, but the rate of reduction is significantly reduced.

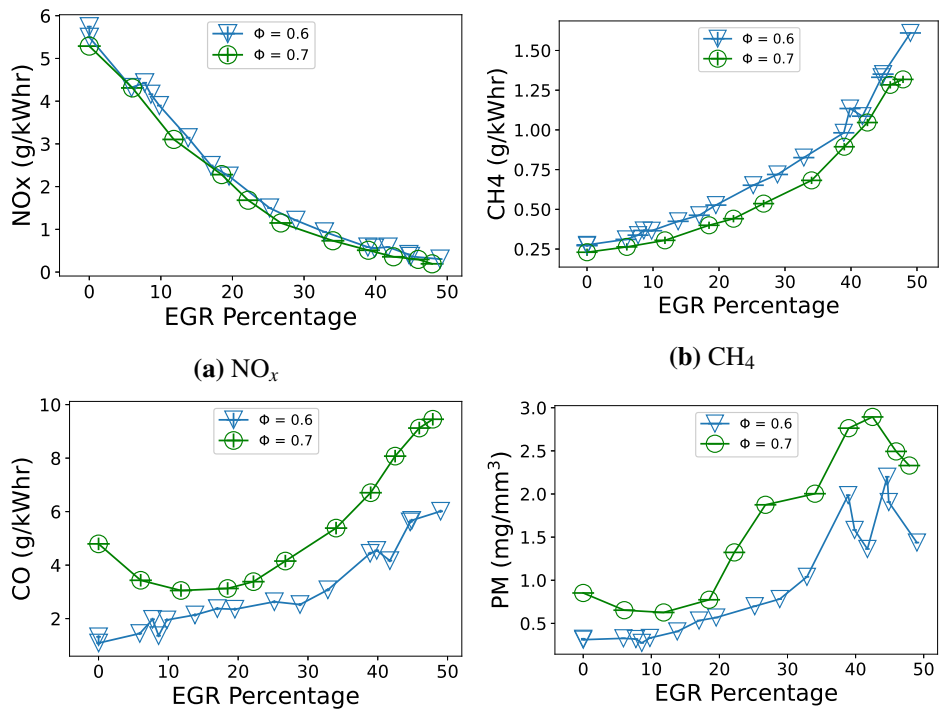

(a) NO_x **(b)** CH_4 **(c)** CO **(d)** PM

Figure 4.8: Indicated specific emissions vs EGR rates. Most significant ISNOx reduction occurs before EGR rates of 30%, but significant increases for the other pollutants occur after 30%.

In contrast, ISCO, ISCH$_4$, and PM increase with increased EGR rates and more variability is observed for each equivalence ratio. ISCH$_4$ has a more dramatic increase at EGR rates above 30%, but the levels are still much less than what is reported by port injected dual fuel NG engines at low load operation (values over 200 $\frac{g}{kW*hr}$ have been reported) [29, 60]. ISCO and PM, for ϕ = 0.7, both initially

decrease slightly with increasing EGR rates before more considerably increasing beyond EGR rates of ∼20% while for ϕ = 0.6, a more consistent increase is observed as EGR rates increase.

The lower O_2 concentrations caused by higher EGR rates results in less oxidation of air bound nitrogen and thus less NO_x. This is also why less ISNOx is observed for the less fuel lean condition ϕ = 0.7. However, lower O_2 concentrations also lead to less complete oxidation of fuel resulting in higher $ISCH_4$, ISCO, and PM emissions.

Another key factor at play in the ISNOx reduction spawned by increasing EGR rates is the reduction of in-cylinder temperatures resulting in less residence time above the Zeldovich threshold temperature of 1700K. Lower temperatures will also reduce full oxidation thus leading to higher $ISCH_4$ and ISCO. However, PM inception requires temperatures around 1400K [64], so while a reduction in O_2 concentration may increase PM formation, significantly reduced temperatures may reduce the time for PM inception. This may explain why a slight reduction in PM is observed at the highest EGR rates for both equivalence ratios.

An important characteristic of ISNOx emissions is the ratio of NO to NO_2 because the selective catalytic reduction system SCR can be more efficient at a ratio of 1:1 (refer to section 1.4.1 for more details). The ratio of NO to NO_2 is quite high until the NO_x from the thermal NO route is significantly decreased. Initially, NO_2 is reduced at a faster rate than NO with the introduction of EGR which leads to an initial increase in the ratio as EGR rates increase. However, this ratio becomes much closer to 1:1 at rates above approximately 35% as shown in Fig. 4.9.

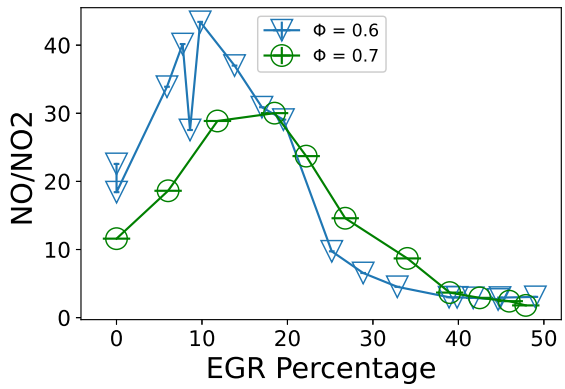

Figure 4.9: NO:NO_2 ratio vs EGR rate. The ratio closer to 1:1 at higher EGR rates is desirable for more a efficient SCR.

Both equivalence ratios demonstrate a relatively slight decrease in indicated specific CO_2 ($ISCO_2$) emissions with an increase in EGR rates. This can be related back to the slight increase in efficiency observed caused by less heat transfer loss and higher peak cylinder pressures with higher EGR rates. Higher efficiencies indicate less fuel is needed which directly relate to $ISCO_2$ emissions when using hydrocarbon fuels.

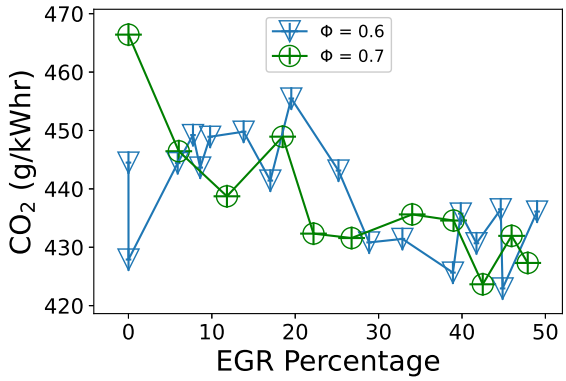

Figure 4.10: CO_2 emissions vs EGR rate for both equivalence ratios. A slight reduction is observed with increasing EGR rates due to higher efficiencies.

4.4 Interpretation of Experimental Results with Kinetic Analysis

As stated in chapter 3, more experimental data was needed to make better use of the zero dimensional chemical kinetic model developed in Cantera. In particular, data from in-cylinder temperatures was needed to more accurately assign initial parameters to the models and identify the parametric sensitivities of NOx to engine relevant parameters. This data could then be used to simulate NO_x production at more realistic engine times at selected temperatures, whether those be assigned isothermal or adiabatic reactors. The following sections describe how in-cylinder pressure data was used to estimate the in-cylinder temperatures for use in adiabatic and isothermal reactors. This was done to isolate parameters such as combustion duration time, temperatures, and oxygen concentrations for further analysis on what factors of EGR affects NO_x emissions most significantly. These models do not serve as an exact replication of HPDI engines (no fuel injection, assumed homogeneous mixture, no mass transfer etc.); however, they can provide insight to processes and sensitivities of NO_x to the specific effects of EGR by isolating them individually.

4.4.1 In-Cylinder Temperature Estimation

The in cylinder temperature was estimated for each EGR rate at each equivalence ratio using the ideal gas law as seen in eqn. 4.24 where P and v are the measured pressure and volume of the cylinder during operation. The mass (m) is the sum total of the air, fuel, and EGR in the intake, and R is the specific gas constant of an unburned mixture composition for each equivalence ratio referenced from [34].

$$PV = m * R * T \tag{4.24}$$

The results of the estimated temperatures for each equivalence ratio can be seen in fig. 4.11. The Zeldovich threshold temperature as defined in section 1.2.1 of 1700K is overlaid on each plot to better visualize the amount of time (as seen in crank angle degrees) each EGR rate experiences above this temperature. These times provide an estimate to the residence time that is used for the kinetic simula-

tions. For instance, for an equivalence ratio of 0.7 and EGR rate of 0%, the time exposed above 1700K is from approximately 365 to 432 CAD, which at 1300 RPM equates to approximately 8.6 ms.

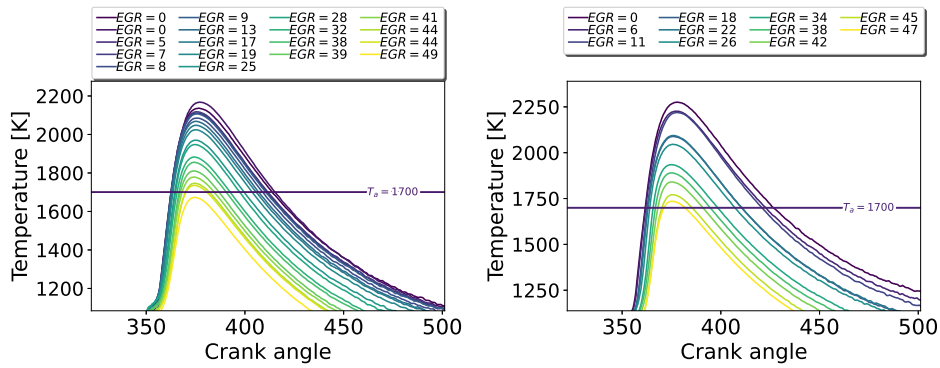

(a) $\phi = 0.6$ **(b)** $\phi = 0.7$

Figure 4.11: Estimated in-cylinder temperature. Peak temperatures and duration time above 1700K decrease with increased EGR.

4.4.2 Variable Time Adiabatic NOx vs Temperature

Following the procedure for an adiabatic kinetic analysis outlined in section 3.4 and using the prescribed temperatures as described above, measured NO_x emissions were overlaid on the modelled results to better observe the sensitivity of NO_x to temperature. To do this, the modelled NO_x of one EGR rate from the adiabatic analysis was first plotted against adiabatic final temperature. The point of interception of measured NO_x for the same EGR rate was then plotted to represent the temperature at which that operating point produced that level of NO_x. This was then repeated for each EGR rate and equivalence ratio as shown in Fig. 4.12. The lower rates of EGR in the model have lower resolution of adiabatic temperature than the higher rates due to the higher overall temperatures generated.

It can be seen that as expected for both equivalence ratios, a trend of lower temperatures correspond to lower NO_x emissions. This is the case for all except modelled NO_x at 50% EGR because the modelled NO_x for both equivalence ratios nearly create no NO_x for the entire temperature range over such a short time span.

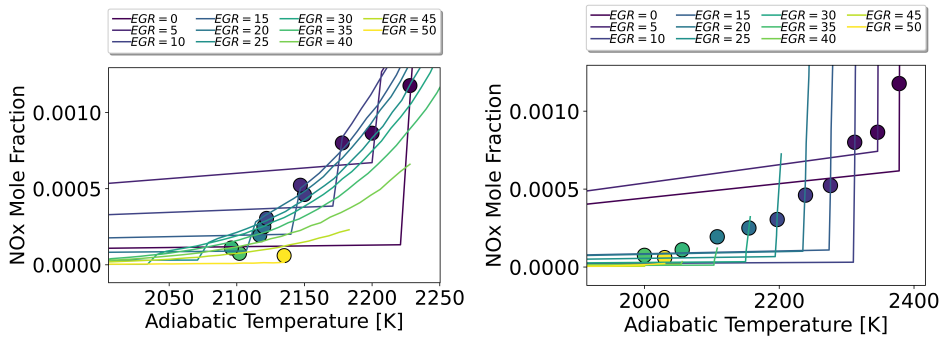

(a) $\phi = 0.6$ **(b)** $\phi = 0.7$

Figure 4.12: Measured NO_x emissions overlaid on top of modelled NO_x emissions using an adiabatic reactor with appropriate combustion duration times assigned for each EGR rate.

This is why the yellow dot corresponding to measured NO_x at approximately 50% EGR appears to form at a higher temperature than for some of the preceding EGR rates. This indicates a limitation to this approach that experimental temperatures are likely higher than the modelled temperatures; however, sensitivities of NO_x to temperature can still be observed.

The temperatures at which the measured NO_x matches the modelled NO_x are higher than the peak temperatures estimated from the in-cylinder pressure measurements. This can be attributed to the estimated temperatures being an average in-cylinder temperature, whereas local in-cylinder temperatures will vary. As mentioned in chapter 1, thermal NO_x is generated on the flame front where the temperatures will be hotter [11].

More significant changes in NO_x are observed at lower EGR rates as temperature is reduced signifying that NO_x is more sensitive at higher temperatures. Sensitivities of NO_x can be quatnified by the rate of change of NO_x vs the change in temperature as defined in eqn. 4.25 where the partials are normalized by the mean temperature difference for the purpose of comparison to other effects.

$$\frac{\partial NOx}{\partial T} * \frac{1}{\overline{T}}\bigg|_{EGR=\not{c}} \tag{4.25}$$

Figure 4.13 shows the sensitivity of NO_x to temperature changes with the peak sensitivity occurring around 2500K for each equivalence ratio. This signifies that any temperature changes at these regions will have a significant impact on NO_x production/reduction. However, this also indicates that when operating at lower temperatures, such as less than 2000K (high EGR rates indicated these temperatures from the measured data overlaid on the adiabatic analysis results) lower temperatures further will not have as strong of an impact on NO_x reduction.

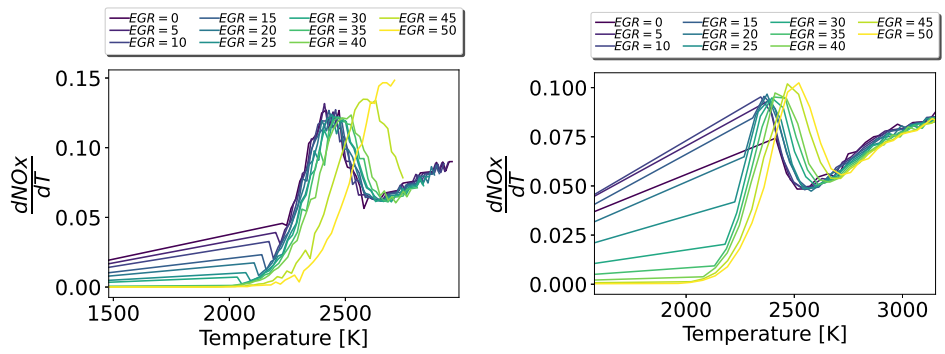

(a) $\phi = 0.6$ **(b)** $\phi = 0.7$

Figure 4.13: The derivative of NO_x over the derivative of normalized temperature for both equivalence ratios. Highest NO_x sensitivity occurs at the temperature range of 2200 to 2600K with slightly more sensitivity for equivalence ratio of 0.6.

4.4.3 T(θ) Isothermal NOx vs O_2 Concentration

To observe the effects that O_2 concentration has on NO_x, the procedure outlined in section 3.4 was executed to produce NO_x in an isothermal reactor where segments of the estimated temperature profile represented one constant temperature. The NO_x produced from each segment was then summed and repeated for several equivalence ratios and EGR rates to create Fig. 4.14. In this case, the O_2 concentration for the measured data could be calculated based on equivalence ratio and EGR rate, so the measured NO_x data was overlaid on top of the isothermal modelled data according to the calculated O_2 concentration.

The measured NO_x data shows similitude with the trend of the equivalence

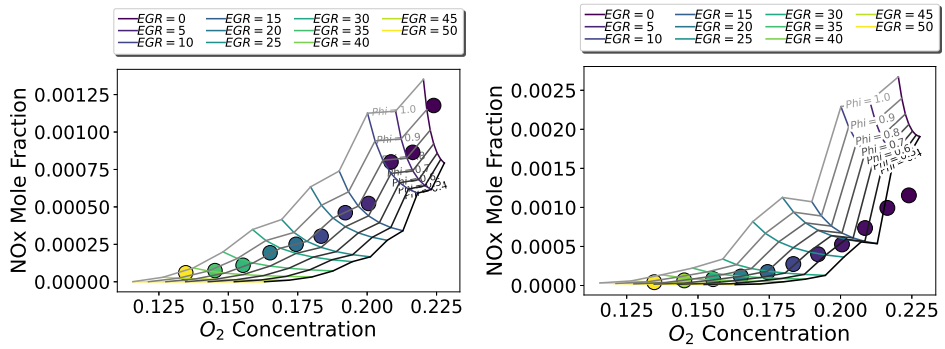

(a) $\phi = 0.6$ **(b)** $\phi = 0.7$

Figure 4.14: Measured NO_x emissions for both equivalence ratios overlaid on top of modelled NO_x emissions using an isothermal reactor used to isolate temperature and duration time above 1700K.

ratio iso lines. This is to be expected because the measured data is all from one equivalence ratio. Because only temperatures above 1700K were used, the model doesn't account for any NO_x formation that could occur before the Zeldovich threshold temperature is reached. However, as discussed in chapter 1, the Fenimore method, or prompt method, of NO_x formation can be more relevant at lower temperatures [43]. This would create the expectation that the measured NO_x emissions would be higher than the modelled NO_x emissions because the full temperature range is included in the measured emissions. Figure 4.14a shows the measured NO_x emissions following the trend of an equivalence ratio of 0.8 (higher NO_x levels than expected) rather than the equivalence ratio of 0.6 of which they were measured. This holds generally true for all EGR rates signifying that there is more involved with NO_x formation than just thermal NO_x above 1700K. This holds true for the equivalence ratio of 0.6 but not for the equivalence ratio of 0.7 signifying a limitation to this approach, but NO_x sensitivities to O_2 concentration can still be analyzed.

Similar to the sensitivities of NO_x to temperature, NO_x is most sensitive to changes in O_2 concentrations at lower EGR rates. This can be quantified using eqn. 4.26 with the partials being normalized with the mean O_2 concentration dif-

ference for better comparison to sensitivities to temperature.

$$\frac{\partial NOx}{\partial O_2} * \frac{1}{\overline{O_2}}\bigg|_{EGR=\not{c}} \tag{4.26}$$

Figure 4.15 shows the sensitivies of NO_x for each individual EGR rate as O_2 concentrations are adjusted with a change in equivalence ratio. Again, lower EGR rates produce much higher sensitivities to NO_x production/reduction; however, the peak sensitivity is less than half that of temperature sensitivities.

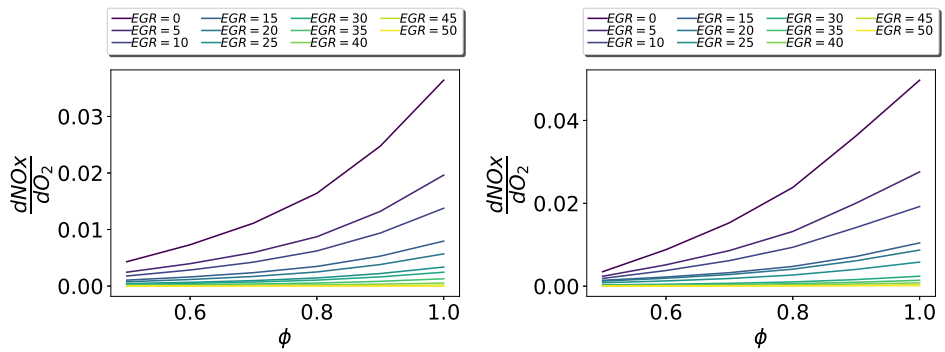

(a) $\phi = 0.6$ **(b)** $\phi = 0.7$

Figure 4.15: Sensitivity of NO_x to normalized O_2 concentrations for each EGR rate. NO_x is much more sensitive to changes in O_2 concentrations at lower EGR rates, but the maximum sensitivity is still less than half as sensitive as maximum sensitivity to temperature changes.

4.5 Summary

Measured emission and engine performance data was recorded up to EGR rates of nearly 50% on account of improvements made to the EGR system including dry EGR which was validated using correction factors. This measured data was implemented into isothermal and adiabatic kinetic analyses to isolate factors such as time and temperature to better observe the sensitivity of NO_x to such factors of EGR. It was determined that NO_x is most sensitive to temperature changes in the range of 2200-2600K. Lower EGR rates do not provide as much NO_x sensitivity to temperature or O_2 concentration changes. These trends could suggest that the cost

of high EGR rates (higher PM, less stable combustion) are not worth the minor reductions in NO_x for an engine calibration.

Chapter 5

Conclusions and Future Work

The need to reduce carbon emissions due to their impact on climate change has motivated the emergence of engine technologies such as HPDI natural gas engines. While these engines can help reduce carbon emissions as compared to their diesel counterparts, they are still a source of toxic NOx emissions which is known to form photochemical smog and can cause eye and respiratory irritation. Exhaust gas recirculation (EGR) has been shown to significantly reduce NOx emissions in compression ignition engines, but the limits and mechanisms of EGR as a NOx reduction strategy are not fully understood for HPDI engines.

The objectives of this research were to primarily develop a better understanding of what specific effects of EGR, such as in-cylinder temperature and O2 concentrations affect NOx emissions most significantly. This was accomplished by using experimental data and numerical models. Secondary objectives were to identify the limits of EGR as a NOx reduction strategy made possible by developing a robust experimental HPDI EGR system capable of attaining and measuring high EGR rates ($\sim 50\%$). Lastly, this information can then be used by researchers and industry innovators as a guideline to NOx formation and limitations in HPDI engines for natural gas, but also toward alternative fuels such as renewable natural gas and hydrogen.

5.1 Conclusions

Measured ISNOx emissions from an incremental EGR experiment on an HPDI engine were found to decrease linearly with increased EGR rates up to an approximate 80% reduction of the non-EGR ISNOx levels. More than another 15% further reduction occurred at higher EGR rates up to 50%, but the rate of reduction was significantly reduced. Other pollutants, such as PM, $ISCH_4$, and ISCO, increased most significantly at EGR rates above 30%. Combustion instability was also found to increase most substantially at rates above 35%. These results suggest that the cost of EGR outweigh the benefits beyond EGR rates of ∼35-40% where the costs are combustion instability, PM and CH_4 emissions.

The experimental data measured from the SCRE helped create more representative numerical models of simplified HPDI combustion by providing realistic in-cylinder temperature profiles for various EGR rates. The models were used to isolate effects of in-cylinder temperatures and O_2 concentrations caused by changes in EGR for better understating of how EGR affects NOx and which effect of EGR has the most impact (in-cylinder temperature, O_2 concentration and combustion duration). From the kinetic analysis, it was found that NOx emissions are nearly twice as sensitive to temperature changes as to changes in O_2 concentrations at maximum sensitivity for each case. NOx was found to be most sensitive at a temperature range from approximately 2200-2500K, which is slightly higher than the experimental peak temperatures estimated from measured in-cylinder pressures. However, diminishing returns of NOx sensitivity begin at in-cylinder temperatures below 2200K. This is also the temperature estimated by the interception of measured data and the adiabatic model for EGR rates above 35%. This further emphasizes the diminishing returns (and high cost) of NOx reduction beyond EGR rates of 35% that reduce in-cylinder temperatures below approximately 2200K.

While NOx is nearly twice as sensitive to changes in temperature as in changes to O_2 concentrations, it is more sensitive to changes in O_2 concentrations at lower EGR rates. Diminishing returns of NOx reduction based on O_2 concentration adjustments begin to develop around 25% EGR. Because PM is formed in an oxygen deprived environment, reducing O_2 concentrations as a strategy to reduce NO_x runs the risk of increasing PM which makes the cost of NO_x reduction even more con-

sequential than by adjusting the temperature especially at higher EGR rates.

The limit of EGR as a NOx reduction strategy in HPDI engines was experimentally determined to be 50% for both equivalence ratios 0.6 and 0.7 under a medium load of 12 bar GIMEP. That was the target for this study because this is the maximum possible EGR in a wastegated turbocharged engine setup. Eventually, the EGR rate became too high to maintain constant combustion phasing because it was no longer responsive to changes in injection timing. The limit of EGR as a NO_x reduction strategy was defined as the maximum EGR rate possible while still maintaining combustion phasing among the other constants.

The COV for maximum cylinder pressure and GIMEP were more unstable for the equivalence 0.7 than 0.6, but a significant increase of the COV occurred for EGR rates above approximately 35%. All experimental tests implemented constant ϕ EGR meaning the equivalence ratio and remained constant throughout the entire EGR range. This influenced slightly more efficient engine performance (along with the ignition delay caused by O_2 concentration reduction) by about 3% with higher EGR rates due to the higher intake pressures and advanced injection timings.

The high rates of EGR were experimentally possible through the modifications made to the SCRE cell including an EGR water condensate trap installed after the EGR cooler, the use of O_2 sensors in the intake and exhaust to measure EGR, and the use of an FTIR to measure emissions and validate the EGR measured by the O_2 sensors. Previously, water in the recirculated exhaust would condense in the intake system and have a significant impact on the repeatability of tests. The FTIR was validated using an AVL CEB II emissions bench and was then used to validate the dry EGR measurements made by the O_2 sensors in the intake and exhaust. The electrochemical sensors allowed for more efficient testing and measurements of EGR allowing for less engine run time which is especially important at more unstable operating conditions such as with high EGR rates. This could also be advantageous in field measurements where a small physical footprint and efficient, reliable data is desirable.

5.2 Future Work

While the main objectives of this research were obtained, some further questions remain pertaining to the limitations of EGR as a NOx reduction strategy in HPDI engines now and in the near future:

- The kinetic analysis could be further developed to more closely represent HPDI combustion. This could include a heterogeneous mixture instead of assuming a homogeneous mixture. A constant volume reactor could also be explored and compared to the constant pressure reactor results used in this research.

- In order to better understand how the EGR effect of the residence time of NOx formation affects NOx, different engine speeds need to be considered. Different engine speeds alone will affect the residence time of NOx formation, but they will also affect the rates of EGR possible at specific engine loads because it will have an effect on combustion stability.

- This work focused strictly on the use of natural gas in HPDI engines, but as the need for less carbon intensive fuels becomes more imperative, the findings in this research can be used toward alternative fuels such as hydrogen. Even though hydrogen in HPDI engines will not produce any carbon emissions, NOx will still be a problem. Based on the results of this work, it can be estimated that higher NOx emissions will be seen for hydrogen fuelled HPDI engines due to a higher adiabatic flame temperature than natural gas. However, higher EGR rates may be advantageous due to the higher flame temperatures creating a more NO_x sensitive environment. This hypothesis can be tested with further experimental research.

Bibliography

[1] F. Aklouche, K. Loubar, A. Bentebbiche, S. Awad, and M. Tazerout. Experimental investigation of the equivalence ratio influence on combustion, performance and exhaust emissions of a dual fuel diesel engine operating on synthetic biogas fuel. *Energy Conversion and Management*, 152:291–299, 2017. ISSN 0196-8904. doi:https://doi.org/10.1016/j.enconman.2017.09.050. URL https://www.sciencedirect.com/science/article/pii/S0196890417308750. → page 63

[2] C. A. Amann and D. C. Siegla. Diesel particulates—what they are and why. *Aerosol Science and Technology*, 1(1):73–101, 1982. doi:10.1080/02786828208958580. URL https://doi.org/10.1080/02786828208958580. → pages xii, 6

[3] Anonymous. *Bosch Automotive Handbook 3rd Edition*. Robert Bosch GmbH, Worldwide Distribution by SAE, 1993. ISBN 1-56091-372-X. → pages 9, 10, 11

[4] N. J. Beck and S. K. Chen. Gas engine combustion principles and applications. In *Future Transportation Technology Conference & Exposition*. SAE International, aug 2001. doi:https://doi.org/10.4271/2001-01-2489. URL https://doi.org/10.4271/2001-01-2489. → page 12

[5] M. C. Besch, J. Israel, A. Thiruvengadam, H. Kappanna, and D. Carder. Emissions characterization from different technology heavy-duty engines retrofitted for cng/diesel dual-fuel operation. *SAE International journal of engines*, 8(3):1342–1358, 2015. → page 2

[6] S. Y. Buhmann. *Introduction: Dispersion Forces*, pages 1–43. Springer Berlin Heidelberg, Berlin, Heidelberg, 2012. ISBN 978-3-642-32484-0. doi:10.1007/978-3-642-32484-0_1. URL https://doi.org/10.1007/978-3-642-32484-0_1. → page 6

[7] S. Carstens and W. Majewski. Nox sensors. *DieselNet*, 12 2019. URL https://dieselnet.com/tech/sensors_nox.php. → pages xiii, 30

[8] B. A. Ceper. Use of hydrogen-methane blends in internal combustion engines. In D. Minic, editor, *Hydrogen Energy*, chapter 7. IntechOpen, Rijeka, 2012. doi:10.5772/50597. URL https://doi.org/10.5772/50597. → page 11

[9] S. Chaudhari. Week 7 - auto ignition using cantera. https://skill-lync.com/student-projects/week-7-auto-ignition-using-cantera-49 Online; accessed 1 November, 2022. Skill Lync. → page 43

[10] Cummins. How an aftertreatment system works. https://www.cummins.com/components/aftertreatment/how-it-works Online; accessed 29 November, 2022. → page 9

[11] J. Dec. A Conceptual Model of DI Diesel Combustion Based on Laser-Sheet Imaging. *SAE International*, 1997. → pages 12, 72

[12] DieselNet. Egr control strategy. https://dieselnet.com/tech/engine_egr_control.php Online; accessed 30 November, 2022. → pages xii, 11

[13] DieselNet. United states: Heavy-duty vehicles: Ghg emissions & fuel economy. https://dieselnet.com/standards/us/fe_hd.php Online; accessed 30 November, 2022. → page 8

[14] DieselNet. United states: Heavy-duty onroad engines. https://dieselnet.com/standards/us/hd.php Online; accessed 29 November, 2022. → page 7

[15] DieselNet. Canada: Heavy-duty engines & vehicles. https://dieselnet.com/standards/ca/hd.php Online; accessed 29 November, 2022. → page 7

[16] DieselNet. Engine emission control. https://dieselnet.com/tech/engine_emission-control.php Online; accessed 29 November, 2022. → page 8

[17] ECM. *NOx CANt NOx CAN Module Instruction Manual*. Engine Control and Monitoring, 2012. → page 57

[18] ECM. *EGR 5230 EGR/Dual Lambda/O2 Analyzer Instruction Manual*. Engine Control and Monitoring, 2017. → pages 50, 57

[19] S. El-Ghafour, A. El-dein, and A. Aref. Combustion characteristics of natural gas–hydrogen hybrid fuel turbulent diffusion flame. *International Journal of Hydrogen Energy*, 35(6):2556–2565, 2010. ISSN 0360-3199. doi:https://doi.org/10.1016/j.ijhydene.2009.12.049. URL https://www.sciencedirect.com/science/article/pii/S0360319909019776. → page 11

[20] EPA. Diesel vehicles. https://www.fueleconomy.gov/feg/di_diesels.shtml Online; accessed 23 November, 2022. → page 1

[21] EPA. Overview of greenhouse gases. https://www.epa.gov/ghgemissions/overview-greenhouse-gases Online; accessed 24 November, 2022. → page 2

[22] E. Faghani. *Effect of injection strategies on particulate matter emissions from HPDI natural-gas engines*. PhD thesis, University of British Columbia, Vancouver, CA, 2005. → pages 12, 29, 32

[23] FortisBC. Natural gas facts. https://www.fortisbc.com/about-us/facilities-operations-and-energy-information/natural-gas-facts#:~:text=Mostly%20made%20up%20of%20methane,propane%20and%20other%20heavier%20hydrocarbons. Online; accessed 15 December, 2022. → page 2

[24] J. Gary Hawley, C. J. Brace, F. J. Wallace, and R. W. Horrocks. Chapter 10 - combustion-related emissions in ci engines. In E. Sher, editor, *Handbook of Air Pollution From Internal Combustion Engines*, pages 280–357. Academic Press, San Diego, 1998. ISBN 978-0-12-639855-7. doi:https://doi.org/10.1016/B978-012639855-7/50049-1. URL https://www.sciencedirect.com/science/article/pii/B9780126398557500491. → pages xi, 3, 4

[25] P. Glarborg. Chapter 11 - detailed kinetic mechanisms of pollutant formation in combustion processes. In T. Faravelli, F. Manenti, and E. Ranzi, editors, *Mathematical Modelling of Gas-Phase Complex Reaction Systems: Pyrolysis and Combustion*, volume 45 of *Computer Aided Chemical Engineering*, pages 603–645. Elsevier, 2019. doi:https://doi.org/10.1016/B978-0-444-64087-1.00011-5. URL https://www.sciencedirect.com/science/article/pii/B9780444640871000115. → pages 3, 4

[26] I. M. Gogolev and J. S. Wallace. Performance and emissions of a compression-ignition direct-injected natural gas engine with shielded glow

plug ignition assist. *Energy Conversion and Management*, 164:70–82, 2018. ISSN 0196-8904. doi:https://doi.org/10.1016/j.enconman.2018.02.071. URL https://www.sciencedirect.com/science/article/pii/S0196890418301882. → page 12

[27] D. G. Goodwin, H. K. Moffat, I. Schoegl, R. L. Speth, and B. W. Weber. Cantera: An object-oriented software toolkit for chemical kinetics, thermodynamics, and transport processes. https://www.cantera.org, 2022. Version 2.6.0. → pages 40, 41

[28] ”Government of Canada”. Guidance document - heavy-duty vehicle and engine greenhouse gas emission regulations. https://ec.gc.ca/lcpe-cepa/default.asp?lang=En&n=71EF09D7-1&offset=3#:~:text=This%20effectively%20includes%20all%20on,the%20Passenger%20Automobile%20and%20LightOnline accessed 29 November, 2022. → page 7

[29] M. Guan. *Measurement and characterization of in-use emissions from dual-fuel diesel engines operating on alternative fuels*. PhD thesis, University of British Columbia, 2021. URL https://open.library.ubc.ca/collections/ubctheses/24/items/1.0406235. → page 67

[30] J. Harrington and R. Shishu. A single-cylinder engine study of the effects of fuel type, fuel stoichiometry, and hydrogen-to-carbon ratio on co, no, and hc exhaust emissions. *SAE Technical Paper*, 730476, 1973. ISSN 2688-3627. doi:https://doi.org/10.4271/730476. → page 6

[31] J. Harrington, S. Munshi, C. Nedelcu, P. Ouellette, J. Thompson, and S. Whitfield. Direct injection of natural gas in a heavy-duty diesel engine. In *Spring Fuels & Lubricants Meeting & Exhibition*. SAE International, may 2002. doi:https://doi.org/10.4271/2002-01-1630. URL https://doi.org/10.4271/2002-01-1630. → pages 11, 12, 13

[32] S. J. Harris and M. Maricq. Signature size distributions for diesel and gasoline engine exhaust particulate matter. *Journal of Aerosol Science*, 32 (6):749–764, 2001. ISSN 0021-8502. doi:https://doi.org/10.1016/S0021-8502(00)00111-7. URL https://www.sciencedirect.com/science/article/pii/S0021850200001117. → pages 5, 6

[33] J. Hawley, F. Wallace, A. Cox, R. Horrocks, and G. Bird. Reduction of steady state nox levels from an automotive diesel engine using optimised vgt/egr schedules. In *International Congress & Exposition*. SAE International, mar 1999. doi:https://doi.org/10.4271/1999-01-0835. URL https://doi.org/10.4271/1999-01-0835. → pages 32, 63

[34] J. Heywood. *Internal combustion engine fundamentals*. McGraw Hill, 1988. ISBN 978-0070286375. → pages xii, 6, 10, 23, 70

[35] P. G. Hill and G. P. McTaggart-Cowan. Nitrogen oxide production in a diesel engine fueled by natural gas. In *SAE 2005 World Congress & Exhibition*. SAE International, apr 2005. doi:https://doi.org/10.4271/2005-01-1727. URL https://doi.org/10.4271/2005-01-1727. → pages 13, 14

[36] R. L. Hoekstra, P. V. Blarigan, and N. Mulligan. Nox emissions and efficiency of hydrogen, natural gas, and hydrogen/natural gas blended fuels. *SAE International*, 961103, 1996. ISSN 2688-3627. → page 11

[37] J. Huang and R. J. Crookes. Assessment of simulated biogas as a fuel for the spark ignition engine. *Fuel (Guildford)*, 77(15):1793–1801, 1998. → pages xi, 2, 3

[38] IEA. The future of trucks. https://www.iea.org/reports/the-future-of-trucks Online; accessed 23 November, 2022. License: CC BY 4.0. → page 1

[39] IPCC. Direct global warming potentials. *IPCC Fourth Assessment Report, Climate Change 2007*, Working Group I: The Physical Science Basis: Chapter 2.10, 2007. → page 2

[40] E. R. Jayaratne, Z. D. Ristovski, N. Meyer, and L. Morawska. Particle and gaseous emissions from compressed natural gas and ultralow sulphur diesel-fuelled buses at four steady engine loads. *The Science of the total environment*, 407(8):2845–2852, 2009. → page 2

[41] M. Karpinski-Leydier. *Machine learning modeling of a direct-injected dual-fuel engine based on low density experimental data*. PhD thesis, University of British Columbia, 2021. URL https://open.library.ubc.ca/collections/ubctheses/24/items/1.0401819. → page 14

[42] J. J. Kasab and A. Strzelec. *Automotive Emissions Regulations and Exhaust Aftertreatment Systems*. SAE International, 2020. ISBN 978-0-7680-9955-3. URL https://app.knovel.com/hotlink/toc/id:

kpAEREAS01/automotive-emissions/automotive-emissions. → pages 5, 7, 8, 9

[43] R. Kee, M. Coltrin, P. Glarborg, and H. Zhu. *Chemically Reacting Flow*. Wiley, 22018. ISBN 9781119186281. → page 74

[44] ”Kistler”. *Compact M5 cylinder pressure sensor*. Kistler, 2021. → page 57

[45] T. Korakianitis, A. Namasivayam, and R. Crookes. Natural-gas fueled spark-ignition (si) and compression-ignition (ci) engine performance and emissions. *Progress in Energy and Combustion Science*, 37(1):89–112, 2011. ISSN 0360-1285. doi:https://doi.org/10.1016/j.pecs.2010.04.002. URL https://www.sciencedirect.com/science/article/pii/S0360128510000377. → page 2

[46] N. Ladommatos, S. Abdelhalim, and H. Zhao. The effects of exhaust gas recirculation on diesel combustion and emissions. *International Journal of Engine Research*, 1:107–126, Dec. 2000. ISSN 20413149. doi:10.1243/1468087001545290. → page 12

[47] F. Leach, G. Kalghatgi, R. Stone, and P. Miles. The scope for improving the efficiency and environmental impact of internal combustion engines. *Transportation Engineering*, 1:100005, 2020. → page 1

[48] A. C. Lloyd and T. A. Cackette. Diesel engines: Environmental impact and control. *Journal of the Air and Waste Management Association (1995)*, 51 (6):809–847, 2001. → page 1

[49] G. McTaggart-Cowan. *Pollutant Formation in a Gaseous-Fuelled, Direct-Injection Engine*. PhD thesis, University of British Columbia, Vancouver, CA, 2006. → pages 12, 21, 22

[50] G. McTaggart-Cowan, W. Bushe, and P. Hill. A supercharged heavy-duty diesel single-cylinder research engine for high-pressure direct injection of natural gas. *International Journal of Engine Research*, 4:315–330, Feb. 2003. ISSN 20413149. doi:10.1243/146808703322743912. → pages 16, 18, 21, 33

[51] G. McTaggart-Cowan, W. Bushe, and P. Hill. NOx reduction from a heavy-duty diesel engine with direct injection of natural gas and cooled exhaust gas recirculation. *International Journal of Engine Research*, 5: 175–191, Sept. 2004. ISSN 214680874. doi:10.1243/146808704773564578. → pages xii, 13, 14, 15, 35, 61

[52] W. F. Northrop, D. Zarling, and X. Li. Considerations in using photometer instruments for measuring total particulate matter mass concentration in diesel engine exhaust. *Journal of engineering for gas turbines and power*, 140(11), 2018. → page 3

[53] Omega. Lcm103b-250 s-beam load cell specifications. https://www.omega.ca/en/force-strain-measurement/load-cells/lc103b/p/LCM103B-250Online; accessed 18 November, 2022. → page 57

[54] P. Ouellette, B. Douville, P. Hill, and B. Ursu. Nox reduction in a directly injected natural gas engine. In *Proceedings of the 1998 Fall Technical Conference of the ASME, IC Engines Division, ICE*, volume 31-3, 1998. → page 12

[55] S. B. Park, H. J. Paik, J. Li, J. O. Chae, J. K. Park, Y. S. Jeong, S. M. Lee, and Y. J. Choi. Effect of intake composition on combustion and emission characteristics of di diesel engine at high intake pressure. In *International Congress & Exposition*. SAE International, feb 1997. doi:https://doi.org/10.4271/970322. URL https://doi.org/10.4271/970322. → pages 12, 63

[56] B. D. Patychuk. *Particulate matter emission characterization from a natural-gas high-pressure direct-injection engine*. PhD thesis, University of British Columbia, 2013. URL https://open.library.ubc.ca/collections/ubctheses/24/items/1.0071963. → pages 37, 38

[57] J. Rochussen, G. McTaggart-Cowan, and P. Kirchen. Parametric study of pilot-ignited direct-injection natural gas combustion in an optically accessible heavy-duty engine. *International Journal of Engine Research*, 21, Dec. 2019. ISSN 20413149. doi:10.1177/1468087419836877. → pages 12, 13

[58] K. Senecal and F. Leach. *Racing Toward Zero The Untold Story of Driving Green*. SAE International, 2021. ISBN 978-0-7680-9422-0. → pages 1, 2

[59] A. Singh. Characterization and system level study of air addition in a pilot ignited direct injection natural gas engine. Master's thesis, University of British Columbia, Vancouver, CA, 2019. → pages 19, 22, 25

[60] D. E. Sommer, M. Yeremi, J. Son, J. C. Corbin, S. Gagné, P. Lobo, J. W. Miller, and P. Kirchen. Characterization and reduction of in-use ch4 emissions from a dual fuel marine engine using wavelength modulation

spectroscopy. *Environmental Science & Technology*, 53(5):2892–2899, 2019. doi:10.1021/acs.est.8b04244. URL https://doi.org/10.1021/acs.est.8b04244. PMID: 30712340. → page 67

[61] D. J. Son. *Development of a fast methane sensor based on wavelength modulation spectroscopy for exhaust methane emission measurement*. PhD thesis, University of British Columbia, 2019. URL https://open.library.ubc.ca/collections/ubctheses/24/items/1.0384580. → pages 7, 56

[62] D. J. Speeding. *Air Pollution*. Clarendon Press, 1974. ISBN 019855463x. → page 3

[63] R. Stone. *Introduction to Internal Combustion Engines*. SAE International, 2012. ISBN 978-0-7680-2084-7. → page 29

[64] D. R. Tree and K. I. Svensson. Soot processes in compression ignition engines. *Progress in Energy and Combustion Science*, 33(3):272–309, 2007. ISSN 0360-1285. doi:https://doi.org/10.1016/j.pecs.2006.03.002. URL https://www.sciencedirect.com/science/article/pii/S0360128506000608. → pages xii, 6, 68

[65] USDOT. Corporate average fuel economy (cafe) standards. https://www.transportation.gov/mission/sustainability/corporate-average-fuel-economy-cafe-standards Online; accessed 29 November, 2022. → page 7

[66] USEIA. Canada executive summary. https://www.eia.gov/international/analysis/country/CAN Online; accessed 30 November, 2022. → page 12

[67] USEIA. U.s. crude oil and natural gas proved reserves, year-end 2020. https://www.eia.gov/naturalgas/crudeoilreserves/ Online; accessed 30 November, 2022. → page 12

[68] USEPA. Air pollution control technology fact sheet. https://www3.epa.gov/ttncatc1/dir1/fscr.pdf Online; accessed 29 November, 2022. → page 9

[69] S. Ushakov, D. Stenersen, and P. M. Einang. Methane slip from gas fuelled ships: a comprehensive summary based on measurement data. *Journal of Marine Science and Technology*, page 1, 01 2019. URL https://www.proquest.com/scholarly-journals/

methane-slip-gas-fuelled-ships-comprehensive/docview/2165963506/se-2. → page 7

[70] C. Wang, Y. Tu, Z. Yu, and R. Lu. Pm2.5 and cardiovascular diseases in the elderly: An overview. *International journal of environmental research and public health*, 12(7):8187–8197, 2015. → pages xi, 3, 4

[71] J. Warnatz. *Combustion: physical and chemical fundamentals, modeling and simulation, experiments, pollutant formation*. Springer, 2006. ISBN 978-3-540-25992-9. → pages 4, 5, 12

[72] WorkSafeBC. Carbon dioxide in industry. file:///C:/Users/kloew/Downloads/ws_09_02-pdf-en.pdfs Online; accessed 24 November, 2022. → page 3

Appendix A

SCRE HPDI Fuel System P&ID

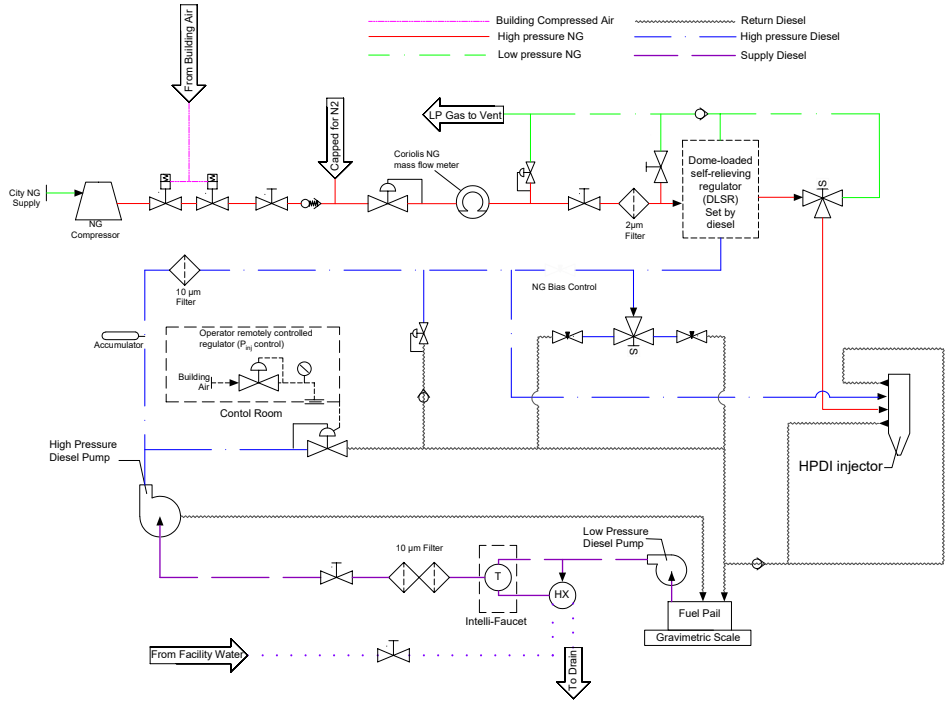

Figure A.1: Piping and instrumentation diagram of SCRE HPDI fuel system

Appendix B

Injector Failure Details

During the time of research for this publication an injector failure was experienced. The symptoms of the failure listed below were first noticed after it had been removed and reinstalled for the replacement of a new pressure transducer. These symptoms are what led to the diagnosis of the failed injector SN 122 as stamped on the injector barrel:

- Engine stopped firing and failed with decreasing combustion stability.
- Very significant gas was blowing out of return line into tank. Sufficient to cause misting of the diesel fuel.
- Diesel was found in the NG line, so the injector was removed to find a broken ring under the first O-ring

The injector was removed from the engine for inspection whereupon a broken O-ring clip was found just below the NG input and above the lower diesel return line as seen in fig. B.1. This failure resulted in high pressure NG leaking into the diesel return line producing the bubbling in the diesel tank. When the system would shut down, low pressure diesel would be pulled through the NG line leaving diesel in the NG lines upon the next start up.

To resolve the issue, firstly the fuel lines were purged to remove diesel from the NG lines. This purge included all of the lines up to the dome loaded regulator to the injector including the common rail. A new injector (SN 60 stamped on the

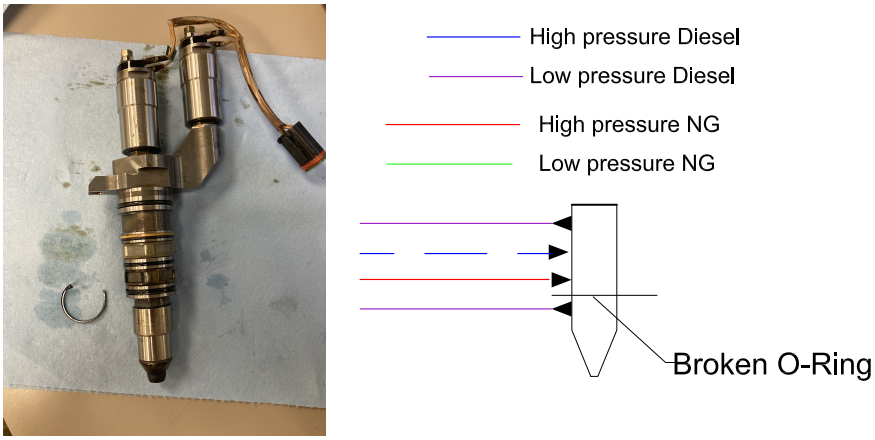

Figure B.1: Broken O-ring from HPDI injector and diagram of where the O-ring was located on the injector relative to the fuel lines

barrel) was installed and the gas leaks were resolved. The damaged injector (122) was sent for diagnosis and repairs before eventually being reinstalled. All tests that were used for the data in this thesis used the repaired injector (122).

Appendix C

FTIR and AVL Comparisons

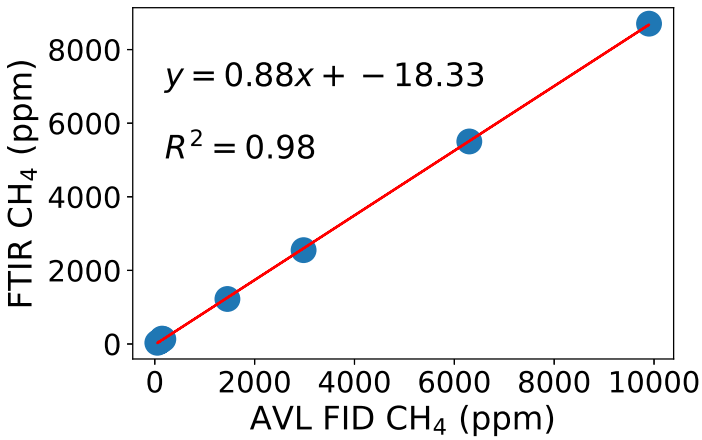

Figure C.1: AVL FID CH_4 comparison with FTIR with very close parity.

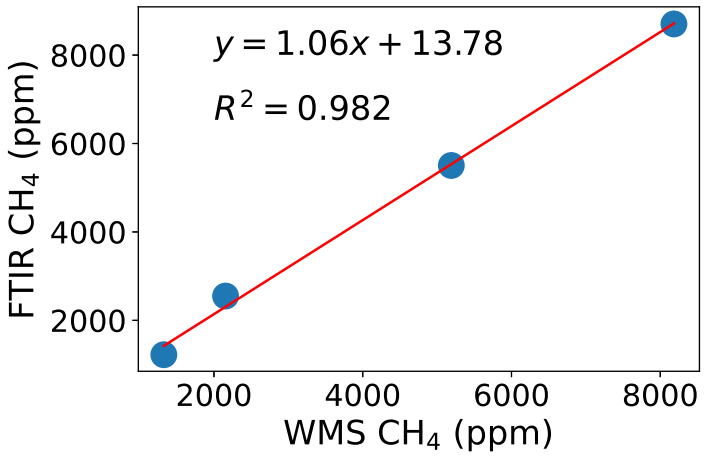

Figure C.2: WMS CH_4 comparison with FTIR. Only a few points were recorded due to the sensitivity of the WMS at low methane concentrations.

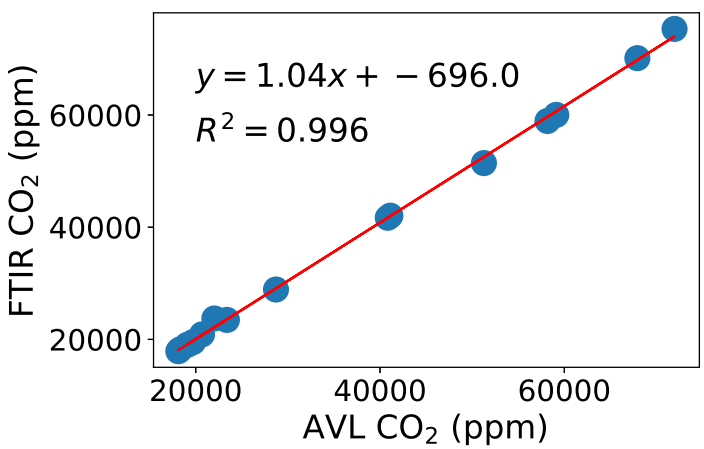

Figure C.3: Wet corrected AVL CO_2 emissions compared to FTIR showing very good parity.

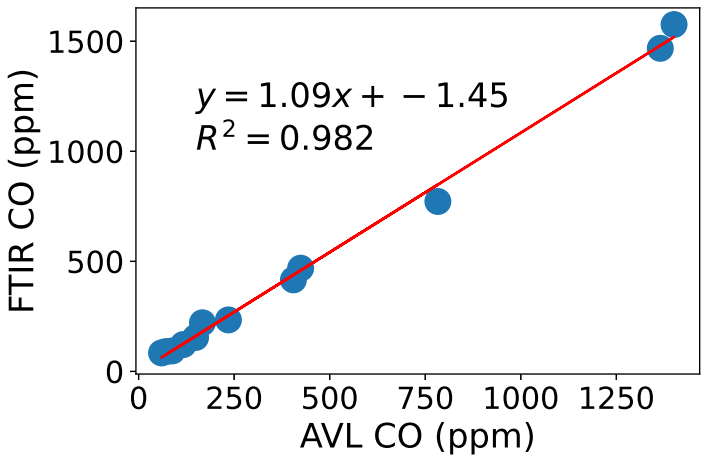

Figure C.4: Wet corrected AVL CO emissions compared to FTIR showing very good parity.

Appendix D

Pressure vs Volume

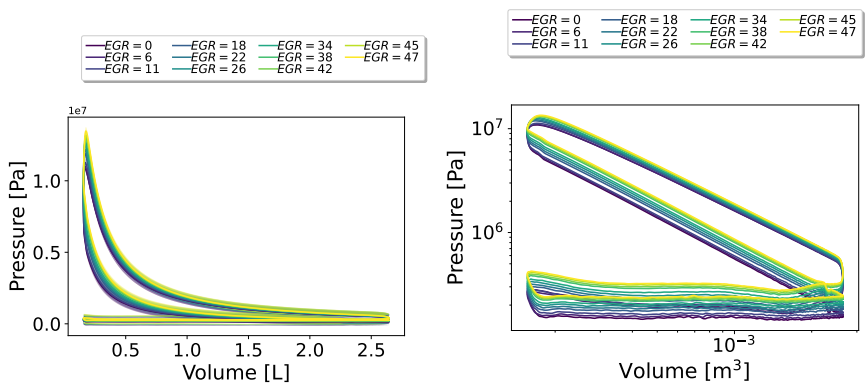

Figure D.1: Pressure vs volume for an equivalence ratio of 0.6. Higher EGR rates increased in-cylinder pressures.

The range of maximum cylinder pressures for the equivalence ratio of 0.6 was from 113.3 bar to 150.2 bar. Likewise, the range for equivalence ratio 0.7 is from 108.9 to 134.8 bar. The difference from minimum to maximum intake pressures as seen in fig. 2.11 is approximately 11 and 10 bar with the maximum being 19 bar and 15 bar for equivalence ratios 0.6 and 0.7 respectively. Higher intake pressures with increasing EGR rates are thus proportional to higher overall in-cylinder pressures.

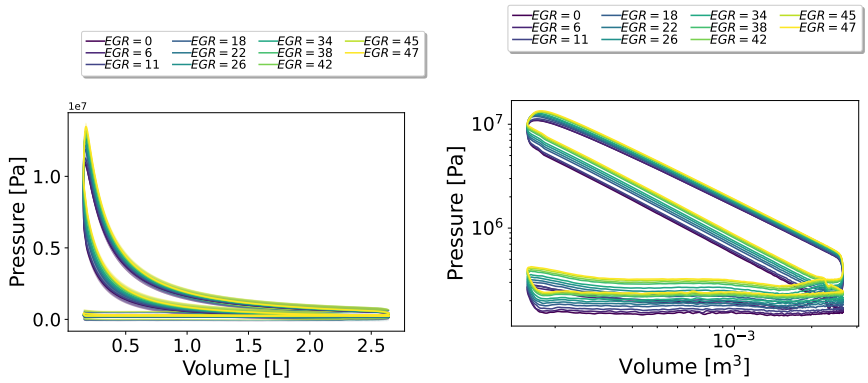

Figure D.2: Pressure vs volume for an equivalence ratio of 0.7. Similar trend is seen as with 0.6, but lower overall pressures due to lower intake manifold pressures.

Appendix E

50% Integrated Heat Release (Combustion Phasing)

The integrated heat release rate is important in maintaining combustion phasing. The point of 50% integrated heat release was used as a constant parameter as outlined in Table 2.4. Figures E.1a and E.1b show the effects of EGR on the integrated heat release. Very little variation is seen with the integrated heat release due to this being one of the constant control parameters. Refer to Table 4.1 for the uncertainty of combustion phasing.

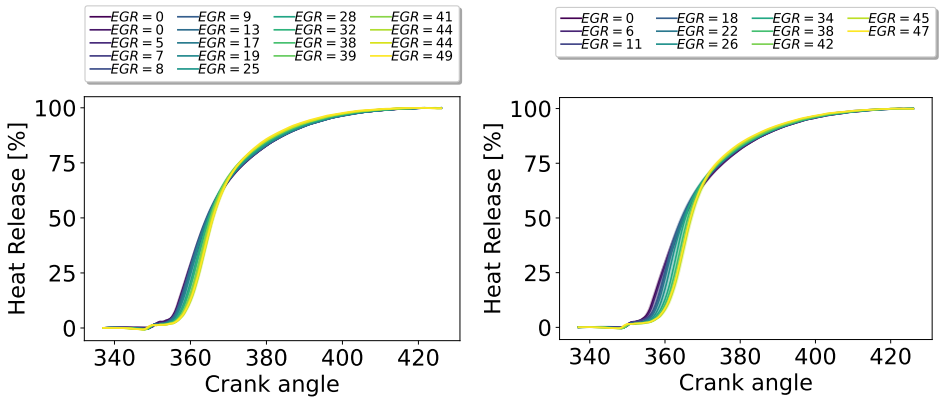

(a) $\phi = 0.6$ **(b)** $\phi = 0.7$

Figure E.1: Integrated heat release rate for both equivalence ratios and each EGR rate. Very little variation seen with increased EGR rates, but slightly more variation with $\phi = 0.7$ (b) than with equivalence ratio 0.6 (a).

Appendix F

Indicated and Brake Mean Effective Pressures

Gross indicated mean effective pressure was another parameter that was controlled to be constant similar to combustion phasing. For this reason, the mean effective pressures did not vary much as EGR rates changed as seen in figs F.1a and F.1b. The definition and calculation for GIMEP is found in section 2.3 with eqn. 2.1.

The brake mean effective pressure (BMEP) was measured from the brake torque (T) of the engine as seen in eqn. F.1. All brake specific measurements (ie. BMEP, torque) are subject to the uncertainty of the strain gauge (Table 4.1) attached to the arm of the dynamometer.

$$BMEP = \frac{2 * \pi * n_c * T}{V_d} \tag{F.1}$$

Net indicated mean effective pressure (NIMEP) is similar to GIMEP except it is the integral across the entire engine cycle and not just from IVC to EVO. This is why it is less than GIMEP because it includes pumping losses. The pumping mean effective pressure (PMEP) is simply the difference between the net and gross indicated mean effective pressures.

The friction mean effective pressure accounts for parasitic losses and in-cylinder friction and is the difference between the NIMEP and BMEP. The total friction mean effective pressure (TFMEP) includes pumping losses and is the difference

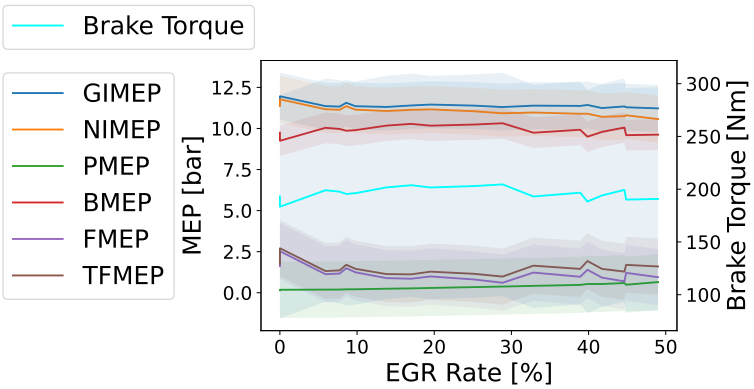

(a) $\phi = 0.6$

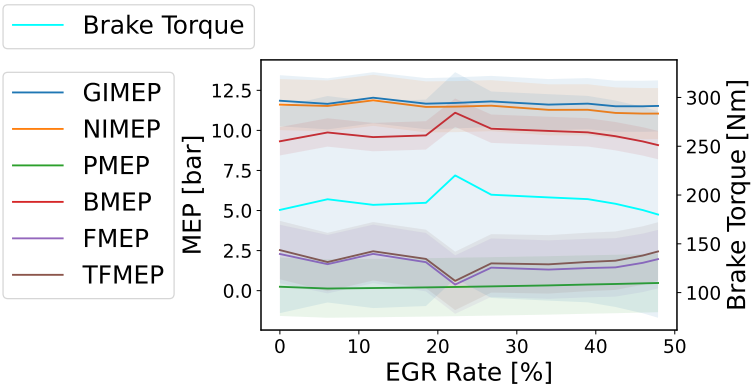

(b) $\phi = 0.7$

Figure F.1: MEPs for both equivalence ratios as EGR rates increse. Most remain relatively constant due to the control parameter GIMEP being held constant.

between the GIMEP and BMEP.

Appendix G

Detailed Measured Emissions

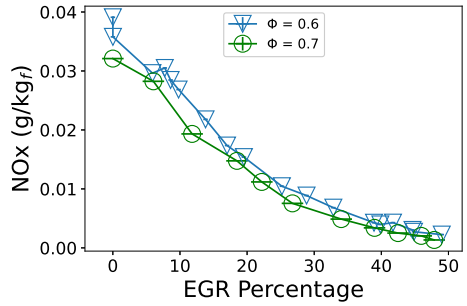

(a) (IFSNO$_x$) vs EGR rate

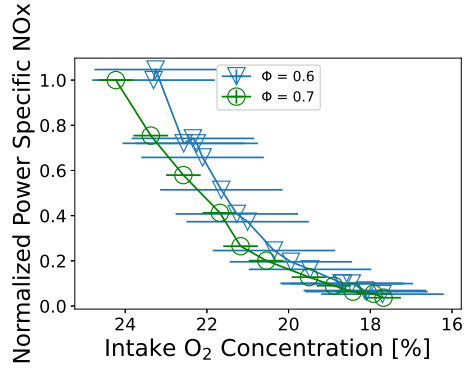

(b) Normalized ISNOx vs O$_2$ concentration

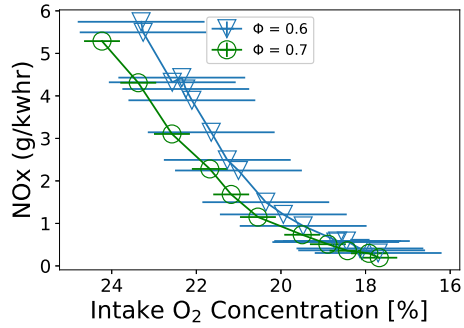

(c) IFSNO$_x$ vs O$_2$ concentration

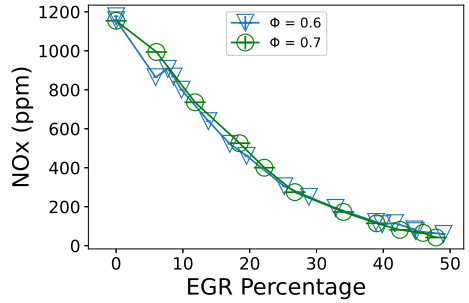

(d) Volumetric NOx vs EGR

Figure G.1: NOx emissions

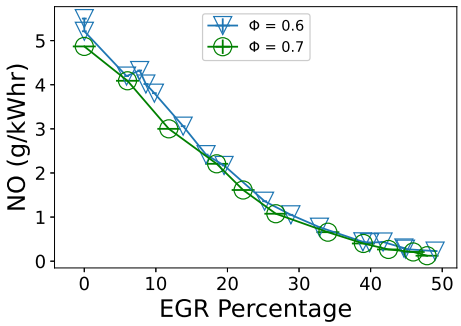

(a) (ISNO) vs EGR rate

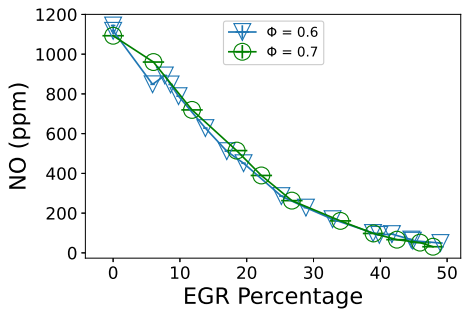

(b) Volumetric NO vs EGR rate

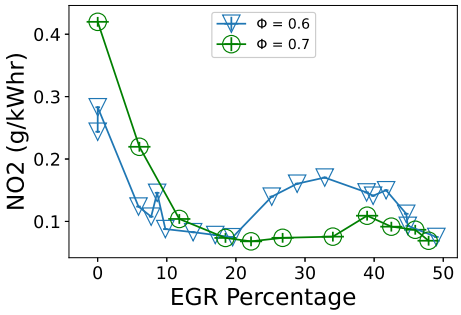

(c) ($ISNO_2$) vs EGR

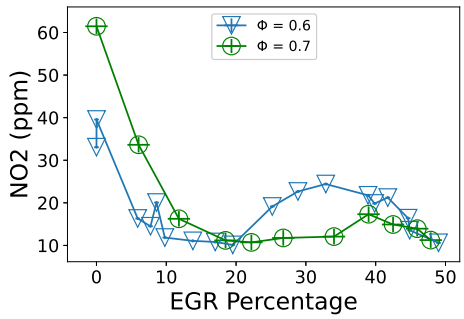

(d) Volumetric NO_2 vs EGR

Figure G.2: NO and NO_2 emissions

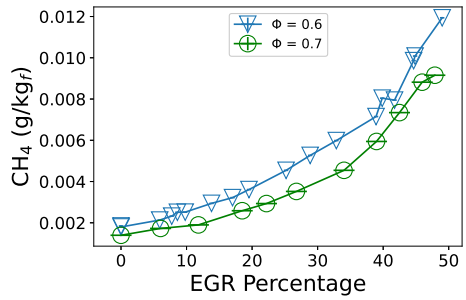

(a) (IFSCH$_4$) vs EGR rate

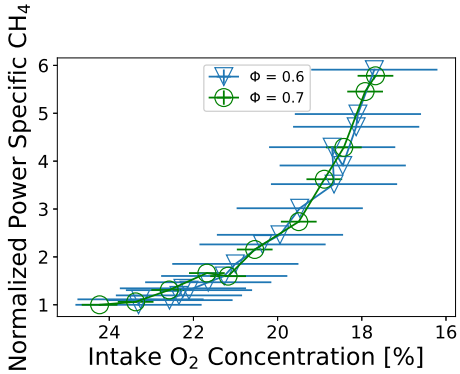

(b) Normalized ISCH$_4$ vs O$_2$ concentration

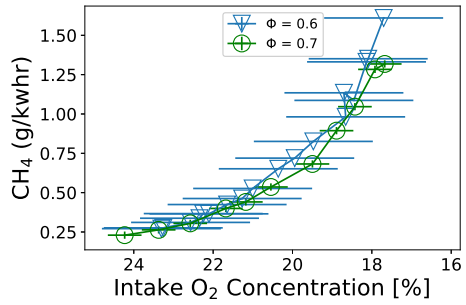

(c) IFSCH$_4$ vs O$_2$ concentration

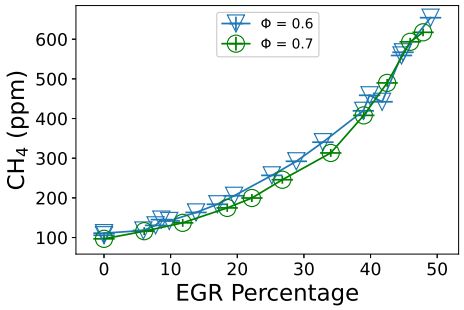

(d) Volumetric CH$_4$ vs EGR

Figure G.3: CH$_4$ emissions

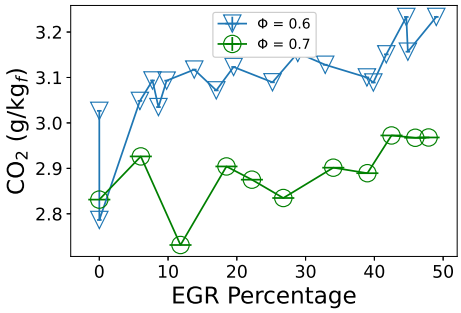

(a) ($IFSCO_2$) vs EGR rate

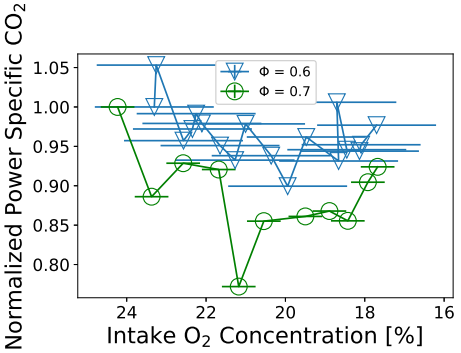

(b) Normalized $ISCO_2$ vs O_2 concentration

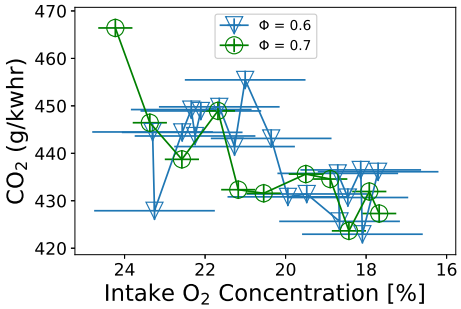

(c) $IFSCO_2$ vs O_2 concentration

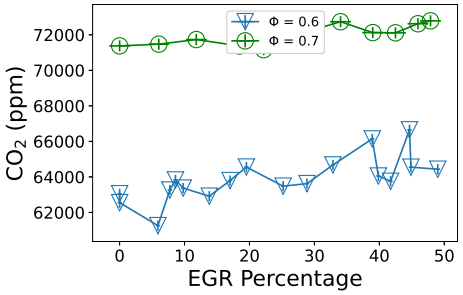

(d) Volumetric CO_2 vs EGR

Figure G.4: CO_2 emissions

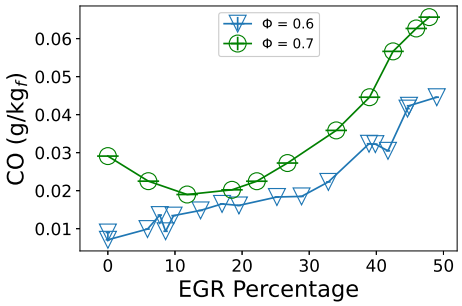

(a) (IFSCO) vs EGR rate

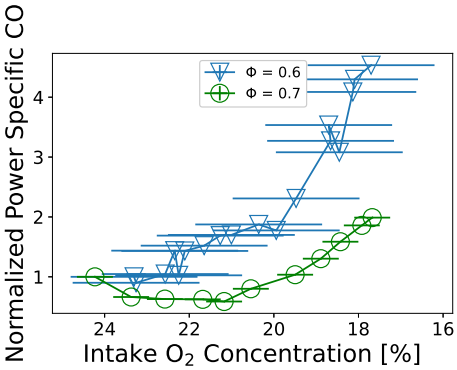

(b) Normalized ISCO vs O_2 concentration

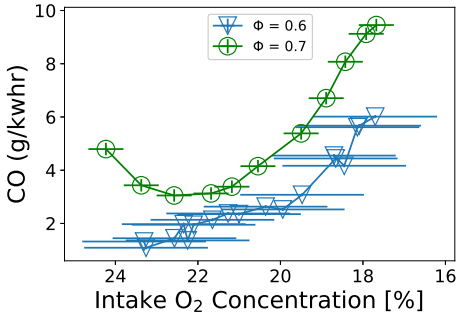

(c) IFSCO vs CO concentration

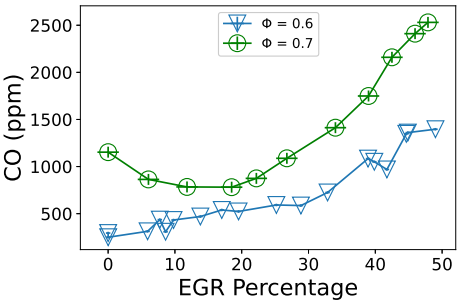

(d) Volumetric CO vs EGR

Figure G.5: CO emissions

Appendix H

NOx sensitivity to Oxygen concentration with a constant equivalence ratio

Unlike when analyzing NO_x sensitivity to temperature changes, NO_x sensitivity to O_2 concentrations can be analyzed based on a constant equivalence ratio or EGR rate as seen in H.1. In other words, the derivative of NO_x was taken following the iso line of each equivalence ratio and each EGR curve as seen in fig. 4.14.

$$\frac{\partial NOx}{\partial O_2} * \frac{1}{\overline{O_2}}\bigg|_{\phi=\not{c}} \tag{H.1}$$

The results of the sensitivity of NO_x to O_2 concentration variations for each equivalence ratio as compared to EGR rates is seen in fig. H.1. This is now referencing the rate of change of the iso lines for each equivalence ratio. In other words, this analyzes how sensitive NO_x is as EGR rates change the O_2 concentrations of a given equivalence ratio. It can be seen that the highest point of sensitivity is around 10% EGR. The effects of EGR as a NO_x reduction strategy begin to dwindle after approximately 30% when only analyzing from an O_2 concentration perspective. Yet, the maximum sensitivity of NO_x to O_2 concentrations for given equivalence ratios is less than half that of the sensitivity to temperature changes.

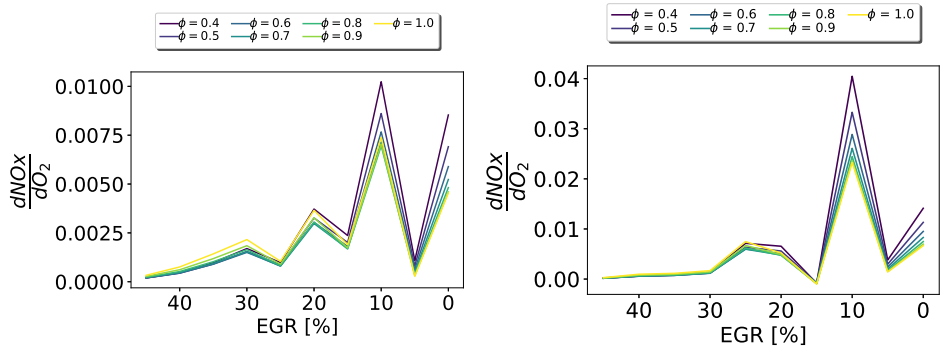

(a) $\phi = 0.6$

(b) $\phi = 0.7$

Figure H.1: Sensitivity of NO_x to normalized O_2 concentrations for seven different equivalence ratios vs EGR rates. NO_x sensitivity to changes in O_2 concentrations begins to dwindle after approximately 30% EGR, but the maximum sensitivity is still less than half that of temperature.